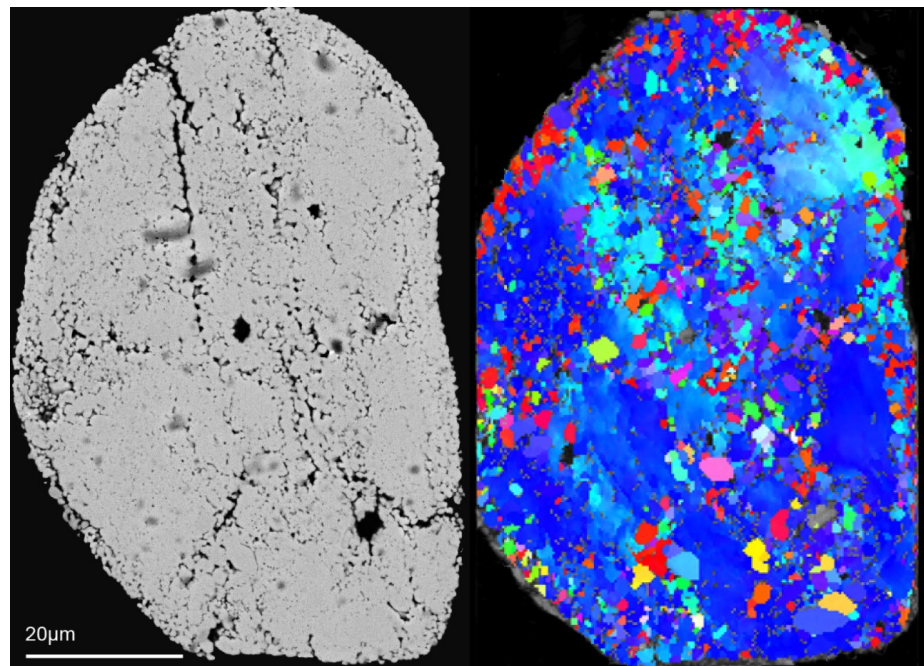# Shock metamorphic features in zircon grains from the Mien impact structure - clues to conditions during impact

__Josefin Martell__

Dissertations in Geology at Lund University,
Master's thesis, no 542
(45 hp/ECTS credits)

Shock metamorphic features in zircon grains from the Mien impact structure - clues to conditions during impact

Master's thesis
Josefin Martell

Department of Geology
Lund University
2018

Contents

Cover Picture: BSE-EBSD image of a granular zircon grain

Shock metamorphic features in zircon grains from the Mien impact structure - clues to conditions during impact

Josefin Martell

Abstract: Well-preserved impact craters are rare on Earth, especially compared to other celestial bodies in our solar system. However, we know that the Earth has been part of the same bombardment and that impact cratering has influenced the Earth's geological and biological history.

When the morphological evidence of a former impact event has been eradicated, the identification of shock metamorphic features in minerals could be the crucial step to confirming a suspected impact structure. These microtextural characteristics may also provide pressure- and temperature (P-T) constraints and reveal information of mineral behaviour at extreme conditions.

This thesis examines shock metamorphic features in zircon from the Mien impact structure and to what extent these can be used to constrain P-T conditions. This has been done by sampling of impactites of three different lithologies from Mien: two impact melt rocks with different degrees of clast-content and one "suevite" breccia; from these rocks, zircon grains were separated. Exterior and interior textures in these grains were documented using scanning electron microscopy (SEM)-imaging, and electron backscatter diffraction (EBSD)-analysis was conducted on a completely granular grain in order to study orientation relationships between granules. Further, Raman spectroscopy was conducted on grains with granular– and microporous texture to reveal potential phase variations.

The main results are 1) a textural study with grains classified on the basis of notable features, revealing granular- and microporous texture as two dominating features in impact melt rocks and 2) the construction of an orientation map with corresponding pole figures, showing a systematic relationship between granules that is indicative of the transformation of and reversion from reidite to zircon. This relationship has just recently been established in studies from other impact structures. I have suggested a P-T-path for the impactites based on observations in this study; the impact melt rocks could possibly have experienced pressures as high as >50 GPa and temperatures ~1500°C. The rarity of granular – and microporous texture in zircon from the "suevite" breccia suggests that these have been subjected to lower pressures and temperatures than the impact melt rocks, which is in accordance with the expected stratigraphy of impactites where the impact melt occur closest to "ground zero".

Josefin Martell, Department of Geology, Lund University, Sölvegatan 12, 223 62 Lund, Sweden. E-mail: josefin.martell@geol.lu.se; josefin@martell.se

Chockmetamorfa texturer i zircon från nedslagsstrukturen Mien, Sverige

Josefin Martell

Sammanfattning: Jämfört med andra himlakroppar i vårt solsystem så finns det få välbevarade nedslagsstrukturer på jorden. Vi vet att jorden har påverkats av nedslag från rymden i lika stor utsträckning som övriga planeter och att dessa nedslag har influerat jordens geologiska och biologiska utveckling. När en krater blivit nederoderad så kvarstår mikroskopiska bevis för att ett nedslag skett på platsen, unika för denna geologiska process. I vissa fall kan de användas för att avgöra vilka tryck- och temperaturförhållanden som rådde när de bildades samt ge information om mineraluppträdande vid extrema förhållanden.

I detta mastersarbete har jag undersökt chockmetamorfa texturer i zirkon från nedslagsstrukturen Mien i Sverige. Impaktiter är bergarter som bildas vid nedslag; tre olika litologier (två smältbergarter och en "suevit" breccia) har insamlats från platsen och från dessa har zirkon separerats ut. Zirkonkornen har sedan undersökts med svepelektronmikroskop (SEM) för att studera texturer på ytan och inuti kornen. Vidare så har en *electron backscatter diffraction (*EBSD)-analys utförts på ett korn med granulär textur, i syfte att undersöka eventuella systematiska förhållanden mellan granuler.

Resultaten visar bland annat att 1) de två dominerande texturerna i smältbergarterna är granulär- och porös textur och 2) ett systematiskt förhållande mellan granuler som är indikativt för tidigare förekomst av högtryckspolymorfen reidite (s. k FRIGN zircon). Med hjälp av dessa fynd var det möjligt att upprätta en tryck-och temperaturkarta som visar att smältbergarterna kan ha genomgått tryck uppemot 50 gigapascal och temperaturer runt 1500°C. Få av zirkonkornen i "suevit" breccian uppvisade granulär eller porös textur, och de bör därför ha upplevt lägre chockförhållanden än smältbergarterna; detta är i enlighet med den generella stratigrafin för impaktiter där smältbergarterna antas ha formats närmast "ground zero".

Josefin Martell, Geologiska institutionen, Lunds Universitet, Sölvegatan 12, 223 62 Lund, Sverige. E-post: josefin.martell@geol.lu.se; josefin@martell.se

1. Purpose of this study

The purpose of this study is to 1) document and study shock textures in zircon from the Mien impact structure in Sweden – one of three large impacts occurring in Scandinavia during the Cretaceous (the others being Dellen, 90 Ma and Lappajärvi, 80 Ma; Henkel 1992) - and 2) assign these textures to corresponding shock pressures and temperatures. Shock-metamorphic features such as planar deformation features (PDFs) in quartz have previously been documented from Mien (Svensson & Wickman 1965; Stanfors 1973), but no studies have yet focused on shock signatures in zircon. This thesis will complement earlier studies of Mien and add to the overall data collection of zircon behaviour at extreme conditions.

2 Introduction

2.1. Meteorite impacts - A planetary perspective

Late morning in 2013, a bright explosion in the sky surprised Russian locals in the southern Ural region. Undetected by warning-networks, a meteor had passed through the Earth's atmosphere and according to Russian authorities (2013a), the shock wave following the explosion damaged some thousand buildings and injured hundreds of people. The meteor explosion above Russia in 2013 is the largest object penetrating the atmosphere since the Tunguska-event in 1908 (Brumfiel 2013) and made the then deputy Prime Minister of Russia to request a "spaceguard" system to protect the planet from extra-terrestrial objects (2013b). Meteorites large enough to cause substantial damage are luckily enough rare (time scale millions of years for meteorites D>1 km). However, we know that at least one has caused a biological mass extinction; 66 million years ago a meteorite impact eradicated the dinosaurs from the Earth, and the catastrophic event now marks the Cretaceous – Palaeogene boundary (Alvarez et al. 1980; Renne et al. 2013).

To date, about 190 terrestrial impact structures have been confirmed (documented in Earth Impact Database), and with new discoveries of impact unique shock features, the list is steadily growing. In contrast to other terrestrial planets and moons in our solar system, the Earth is a geologically active planet. Since we know that meteorite impacts have had a large influence on the Earth's geological and biological history, impact indicators such as shock textures in minerals are vital to establish e.g. crater formation processes on Earth and the following mineralogical and biological effects. By looking at other planetary bodies, we also
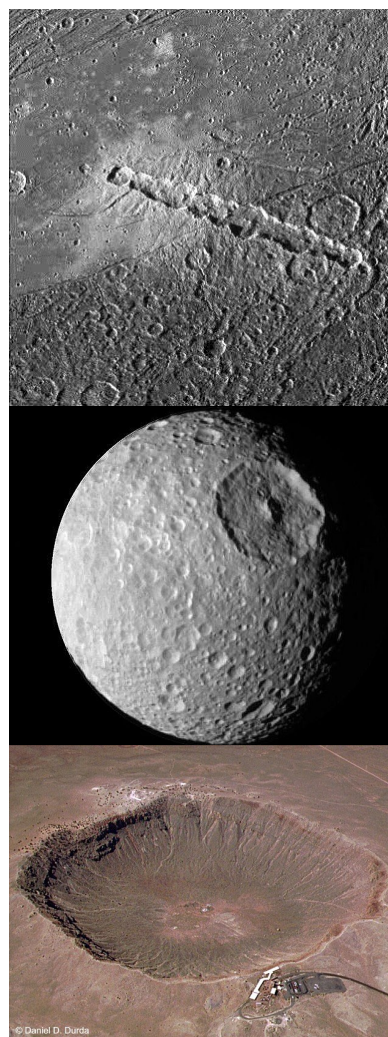

Figure 1. From top: a chain of 13 closely spaced craters on Ganymede, one of Jupiter's moons (Galileo spacecraft, NASA 1997). A complex crater on Mimas, one of Saturn's moons (Cassini spacecraft, NASA 2005). Photo of Meteor Crater in Arizona, a bowl-shaped simple crater (Photo courtesy Daniel D Durda).

know that this has been a frequent and on-going process since the formation of our solar system, and that impact craters must have existed to the same extent here. Refined age dating of known structures could reveal whether these impacts have occurred randomly or followed a periodic pattern. Old impact basins in the range of >1000 km on our moon and other planets (Fassett et al. 2009; Spudis P. D. et al. 2013; Norman & Nemchin 2014) show that a similar magnitude meteorite bombardment must have hit the Earth early in the history of the planet (>3.8 Ga). These impacts may have triggered volcanism and generated immense volumes of impact melt, contributing to creating the early continental crust (Frey 1980; Glikson 2001). The oldest identified impact structures on Earth are Vredefort

in Canada and Sudbury in South Africa (Krogh 1984; Kamo et al. 2011), but these are considerably smaller and younger than what can be expected from the Early earth bombardment. Because of endogenic and active processes such as sedimentation and erosion it has been estimated that ~20 % of impact structures on Earth are buried (from present terrestrial record) (Grieve 1991).

Some of the last remnants of impact structures are microscopic "fingerprints", expressed as shock textures- and features in minerals. Several studies of shocked zircon have demonstrated that microtextures can register extreme temperatures and pressures (P and T) allowing thermobarometrical calculations (Timms et al. 2017 and references therein); this is the only terrestrial mineral known to register both pressure and temperature during an impact event.

2.2. The process of impact cratering

Impact craters are classified based on three main morphological types (with increasing size): simple craters, complex craters and multi-ring basins (Fig. 1) (Dence 1972). Due to the extreme conditions taking place during an impact event, craters of similar size tend to have an analogous morphology regardless of local geology at the impact site. Impact structures with a diameter of ~4 km and above have central uplifts and are classified as complex craters whereas a smaller (simple) structure has a bowl-shaped appearance.

The formation process is generally divided into three main events. The first stage takes place instantly as the projectile hits the target rock (at a velocity ~15km/s), causing compression and an instantaneous transfer of kinetic energy into the target. Shock waves propagates into both projectile and target and results in a transient crater (Melosh 1989), and as the shock waves pass, decompression leads to brecciation and melting of rock. A part of the kinetic energy is converted to thermal energy and to internal energy of target rocks, a process that can generate shock-metamorphic features in minerals. The second stage is the excavation of the actual crater; a complex process where shock waves are reflected as they intersect with the original ground surface, with fracturing and shattering of rock as the result; some of this material will be ejected from the crater at high speed. The excavation flow proceeds from the outward movement of target rocks from the impact point, creating a bowl-shaped depression (Melosh 1989; French 1998 and references therein). Due to the volume of ejected material, the diameter of the final crater will be considerable (20-30 times) larger than that of the projectile (French 1998). As the maximum size has been achieved, gravity will begin to modify the crater. There is no definite end to this stage as normal geological processes such as sedimentation, erosion and tectonics are on-going processes.

Table 1. Difference between regional- and contact metamorphism and shock metamorphism (Modified from French 1998)

	Regional and Contact Metamorphism; Igneous Petrogenesis	Shock Metamorphism
Geological setting	Widespread horizontal and vertical regions of Earth's crust, typically to depths of 10-50 km	Surface or near-surface regions of Earth's crust
Pressures	Typically <1-3 GPa	100-400 GPa near impact point; 10-60 GPa in surrounding rock (within crater)
Temperatures	Generally ≤1000°C	Up to 10,000°C near impact point (vaporization); typically from 500°C to 3000°C in surrounding rock
Strain rates	10^{-3}/s to 10^{-6}/s	10^4/s to 10^6/s
Time for completion of process	From 10^5 - 10^7 yr	"Instantaneous". Shock-wave passage through 10-cm distance <10^{-5} s; formation of large (100 km-diameter)
Reaction times	Slow; minerals closely approach equilbrium	Rapid; abundant quenching and preservation of metastable minerals and glasses

2.3. Shock metamorphism in minerals

As shown by Table 1, several factors differentiate shock metamorphism from other geological settings. The most significant of these is the time perspective; as shock waves propagate rapidly through the target rock, the constituent minerals are subjected to temperatures and pressures that normally would occur only at lithostatic pressures at 75-1000 km, creating shock-textures unique to the impact process (French 1998). Transient stress conditions, high strain rates and rapid quenching of minerals further characterize the formation of shock effects.

In non-porous rocks, pressures of 2-6 GPa will result in breccia formation and shatter cones, the latter being a diagnostic evidence of impact. Above pressures of 10 GPa, microscopic shock features such as planar deformation features (PDFs) in quartz (Fig. 2),

SiO_2 transitions to stishovite and coesite (transition of quartz-coesite takes place at >3 GPa) and formation of diaplectic glasses without melting (Stöffler 1972; Stöffler & Langenhorst 1994) will take place. At extreme pressures of >50 GPa, partial or complete melting occurs, and extreme pressures of >100 GPa leads to complete vaporization (Fig. 2)(French 1998). The diagram (Fig. 2) depicts the shock-metamorphic "field" with respect to normal crustal metamorphism (note that the horizontal scale is logarithmic).

Quartz is one of most abundant minerals in the Earth's crust and its shock behaviour over a range of shock pressures has been well established (French 1998). PDFs in quartz are generated exclusively in impact related settings and occur as narrow spaced planar lamellae in several sets. They form as the atomic structure gets deformed, where quartz transforms
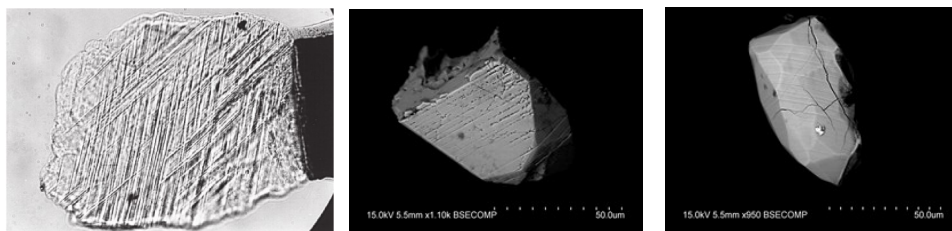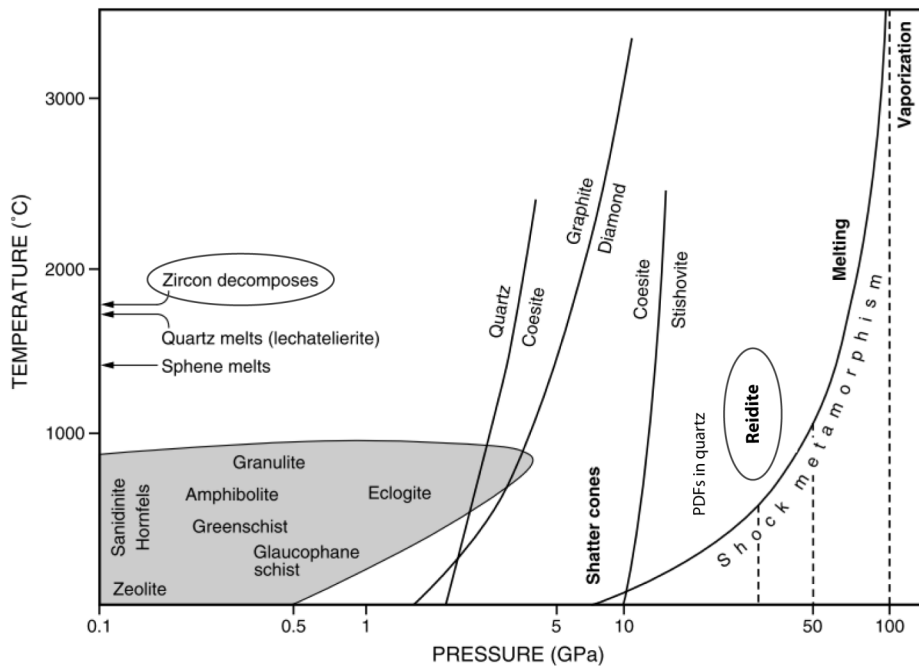

Figure 2. The diagram show a comparison between normal crustal metamorphism (and metamorphic facies) and shock metamorphism (modified from French 1998). Pictures below: polished quartz grain with PDFs (photo courtesy of G.A. Izett), two zircon grains from the Siljan impact structure displaying PDFs or PFs (Martell 2016).

Table 2. Main characteristics of zircon, baddeleyite and reidite (Modified from mindat)

Chemical formula	$ZrSiO_4$ (zircon)	ZrO_2 (baddeleyite)	$ZrSiO_4$ (reidite)
Crystal system	Tetragonal	Monoclinic	Tetragonal
Crystal class	Ditetragonal dipyramidal 4/m 2/m 2/m	Prismatic 2/m	Dipyramidal 4/m
Space group	$I4_1/amd$	$P2_1/b$	$I4_1/a$
Density (g/cm³)	4.6-4.7	5.5-6	5.2
Cleavage	[001] Indistinct	[001] Distinct	None

from mindat.org

into a distinct amorphous phase (Goltrant et al. 1991; Goltrant et al. 1992). Quartz polymorphs such as coesite and stishovite can support or verify an impact origin, either by themselves as constituents in impactites, or as disequilibrium assemblages with other silica products e.g. coesite + stishovite + quartz + silica glass. Similar shock features can be found in feldspar, but since feldspar and quartz generally occur in the same lithologies, identifying PDFs in quartz is a quicker method of establishing impact origin of a suspected crater. Planar microstructures similar to PDFs have been found in shocked zircon (Fig. 2; Leroux et al. 1999; Wittmann et al. 2006; Erickson et al. 2012; Martell 2016).

2.4. Shock features in zircon

As zircon ($ZrSiO_4$) has the ability of withstanding both high erosion rates and metamorphic temperatures (Hanchar & Miller 1993; Wittmann et al. 2006; Erickson et al. 2017) it enables investigation of mineral behaviour at extreme conditions. Further, its tendency to incorporate uranium (U) and thorium (Th) makes it a well-used geochronometer (Zhang et al. 2000; Erickson et al. 2017). Several ancient impact structures have been dated with zircon, for example the Sudbury impact structure (Krogh 1984), Vredefort crater (Kamo et al. 1996), and even zircon from a clast-rich impact-melt lunar sample, brought by the Apollo 17 mission (Nemchin et al. 2009). Zircon belongs to the tetragonal crystal system ($I4_1/amd$ and $Z=4$), and the ideal structure consists of alternating SiO_4 tetrahedra and ZrO_8 triangular dodecahedra that extends parallel to the crystallographic c-axis (Table 2; Finch & Hanchar 2003); together with baddeleyite (ZrO_2) it is the most common accessory mineral containing zirconium. Baddeleyite occurs in silica-undersaturated mafic rocks and these phases thus complement each other since both minerals can be dated with uranium-

lead (U-Pb) method.

Low-grade metamorphic zircon shows a variety of textures that are usually inherited from the protolith, and a common feature is metamorphic overgrowth and signs of resorption. Expected external morphologies are rounded or ovoid shapes, and the surface may have etching- or pitting marks (Hanchar & Miller 1993; Hoskin & Schaltegger 2003). Zircon microstructures that can be developed as a result of shock include the development of granular texture (e.g. Bohor et al. 1993; Wittmann et al. 2006), conversion to the ~10% denser scheelite structured high-pressure polymorph reidite (space group = $I4_1/a$) (Knittle & Williams 1993; Pidgeon et al. 2011) (Table 2), mechanical twins along (112) and (100) parallel deformation bands (Erickson et al. 2017). Some of these features are criteria diagnostic of a hypervelocity origin (Timms et al. 2017). Shock signatures in zircon can be an option in rocks where quartz is absent or rare, such as in Martian samples and in some terrestrial lithologies (Erickson et al. 2017).

2.5. Impactites

Impactites (Fig. 3) are rock that have been produced or altered in association with a terrestrial hypervelocity impact (French 1998). They can take various forms depending on formation process e.g. during the initial shock waves, the subsequent excavation flow and crater formation or the following modification processes. Shock characteristic features may be visible in outcrop, hand specimen and/or in thin section. Impactites are often heterogeneous (Dence 1971), but since no new mineral constituents are added in the processes, the composition of impactites will be close or a mixture of that of the target rocks, with the possible addition of meteoritic material, fusion of minerals with low melting points (Dressler & Reimold 2001), and post-impact alterations. Chemical differences between

the target rock and the impactite are thus mainly explained by reaction with vapors and solutions at high-temperature conditions, with near-surface crystallization and access to atmospheric oxygen (Dence 1971).

The classification of impactites is an active debate. The most recent nomenclature for impactites has been defined by Stöffler & Grieve (2007), who describes the term impactite as a *"collective term for all rocks affected by one or more hypervelocity impact(s) resulting from collision(s) of planetary bodies"*. The general model takes into account the location around or within the crater, sources of material, particle size, shock-metamorphic effects in minerals, textures in melt-rocks and relative percentage of the different components (matrix, inclusions, rock fragments) in breccia, but individual factors such as target lithology and the nature of the impactor will influence the final appearance of impactites. The classification is unique to impact generated rocks, but uses traditional terms such as breccia and melt-rocks.

2.5.1. Suevite

One characteristic rock type found in terrestrial impact structures of crystalline target is so called "suevite" (French 1998; Stöffler et al. 2013). Suevites are composed of bodies of melt and discrete fragments of rock, in a clastic matrix of similar but finer-grained materials (French 1998); breccia containing less than 1-2% of impact glass are often called "suevitic". The "original" suevite has its type locality in Ries crater in Germany (Von Engelhardt 1997; Stöffler et al. 2013). The rock consist of a fine-grained matrix with small (~1 cm) glassy bodies that constitute 5-15vol% of the rock (French 1998). Suevite may occur as *crater suevite ("fallback")*, *outer suevite ("fallout")*, or *dike suevite*, the latter in the parautochtonous crater basement and in crystalline megablocks around the crater. The IUGS Subcommission on the Systematics of Metamorphic rocks proposed a detailed definition of suevites in 2007 (as they have been described above; Stöffler & Grieve 2007). This definition has since been challenged - with the recommendation that "suevite" should be reserved for the Ries suevite and that other "suevites" should be classified as melt-bearing breccias or "suevitic" breccias – due to inconsistent use of the term, and new discoveries that the rocks may have had completely different genesis (Osinski & Pierazzo 2012; Osinski & Grieve 2017).

2.5.2. Formation of impact-melt rocks

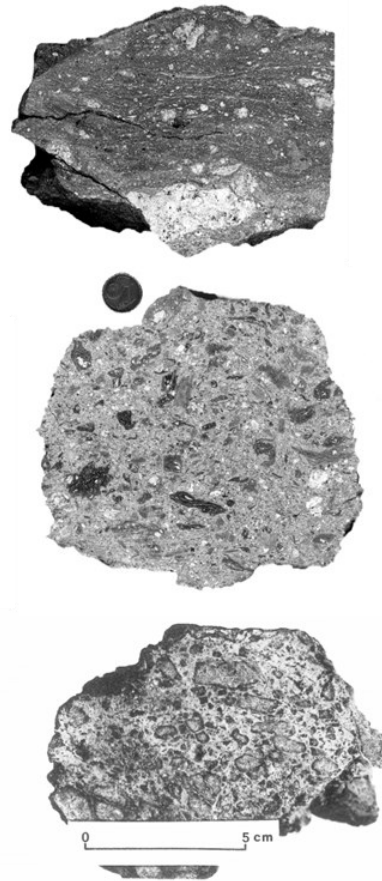Even though impact melt rocks can look very similar to igneous rocks, the formation of these is completely

Figure 3. Three types of impactites from Mien (starting from top): impact melt rock, "suevite" breccia (Photo courtesy Kord Ernstson) and crystalline breccia (from Stanfors 1976).

different. When the impactor hits the target rock, post-shock temperatures can rise to 2000°C which is well beyond the melting point of most rock-forming minerals. As the shock waves pass through the target rock, pressures will instantly return to normal causing complete melting of rocks close to "ground zero" (Fig. 4) and significant melting will occur above 40 GPa. Rock that has been subjected to complete melting or have been modified at lower pressures will contain distinctive shock features such as shock-metamorphosed inclusions, and will therefore be possible to distinguish from normal igneous rocks. The melt becomes part of the overall flow that opens up the transient crater, and the movement can occur at extreme speed. Original impact velocity may even be exceeded for ejected material of melted and vaporized rock at the point of impact. The ejected material can be seen as small spherules and larger glassy bodies around the impact structure. However, this represents a small part of the larger volumes of melt that are generated subsequently inside the crater. As seen in Figure 4, the larger volume of

melt is located in the center, and moves downward and upward towards the floor subsequent to the developing transient crater. When the melt reaches the bottom, it will start to move upwards, losing speed. At this point it can incorporate inclusions from the floor and walls, generating a series of impact-melt rock types, such as clast-rich impact melt breccia and impact-melt rock. The general location of these types is shown Figure 4. The inclusions will both slow- and cool-down the melt, and some of the melt that reaches the top of the crater walls will spread out around the crater similar to a lava flow. Since both melted material and inclusions derive from the target rock, the composition of all impact rocks will be similar to the target rocks; meteoritic contamination seen as chemical anomalies may be observed during chemical analysis.

In larger impact structures, most melt will remain as a layer within the crater and on top of breccia.

It has been observed that crater structures that formed in sedimentary rock will contain less impact melt rock than those in crystalline rock, regardless of size (e.g. Ries in Germany). Possible explanations are that the porous and sometimes volatile-rich sedimentary rock form small vesicular aggregates as they melt, which is ejected from the crater as a plume of expanding volatiles, leaving less melt within the structure (Kieffer & Simonds 1980). As the shock wave moves through the target rocks, peak pressure and post-shock temperatures rapidly drops further away from the center, forming a series of "hemispherical shells" around the point of impact that represents different shock pressures (Fig. 4) (French 1998).
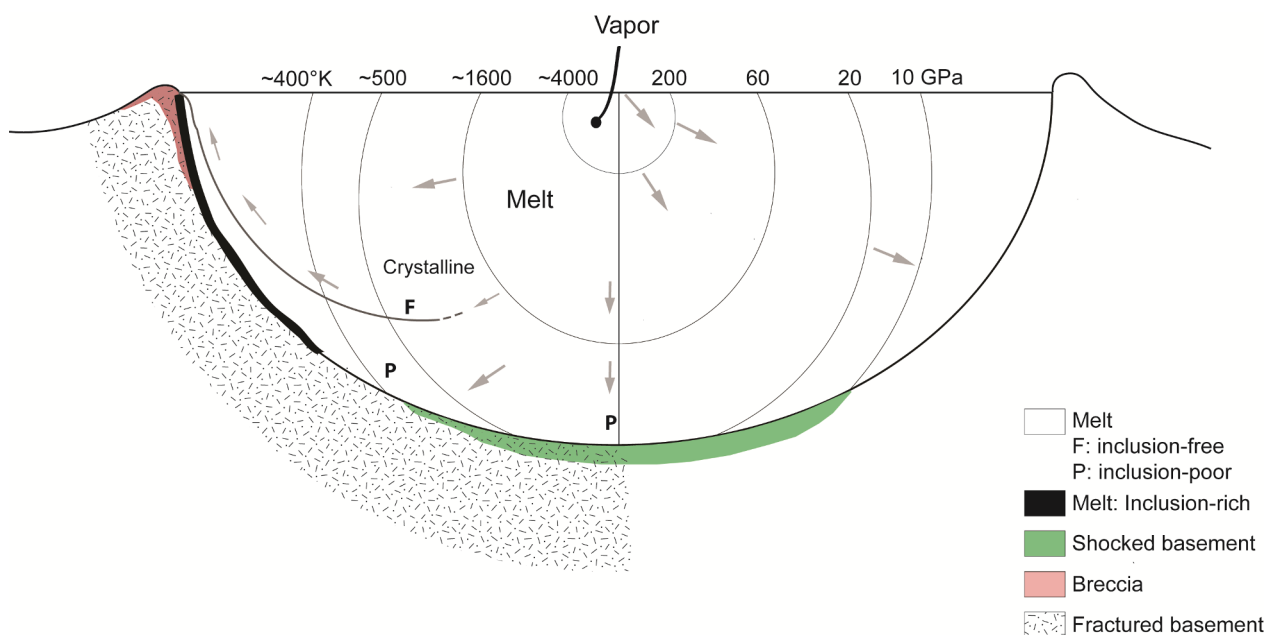

Figure 4. Formation of impact-melt rocks. Hemispherical "shells" of different shock pressures form as the projectile hits the target rock. Rock right underneath the impact point will be vaporized. Substantial volumes of melt will form at a slightly lower temperature and pressure; this melt will flow downward and upwards along the walls of the transient crater (Modified from French 1998).

3. Lake Mien impact structure

"Bergartsprofven se öfver hufvud alldeles icke ut som normala stelningsbergarter, och jag skulle nästa icke vilja visa ifrån mig den åsigten, att de hafva en full-komligt abnorm process att tacka för sin uppkomst."

(Translation: "The rock specimens do not at all look like normal eruptive rock; I would almost consider them to be the result of a completely abnormal process" (Holst 1890).

The Mien impact structure is located in Småland county, southeastern Sweden (56.41812°N 14.85785°E) (Fig. 5) and is one of Sweden's eight confirmed impact structures (Earth impact database 2018). The first to carry out an extensive geological investigation of Lake Mien was Nils Olof Holst who is the author of the quote above. He was also the first to document another typical feature – ballen-textured quartz – a shock induced texture in quartz consisting of spheroid shapes, now considered impact characteristic (Holst 1890; Ferrière et al. 2010). With some doubt, he made an, by that time, educated guess that the structure was the remnant of a tertiary volcano. This theory was more or less accepted until 1965 when Svensson & Wickman (1965) discovered coesite-bearing samples, which among other findings strongly indicated an impact origin of Lake Mien. Only a few articles related to the Mien impact structure has been published since the 70s, the most comprehensive being a doctoral thesis by Stanfors (1973). His work includes crater morphology, geophysical studies and detailed descriptions of the petrography.

The original rim diameter (pre-erosion) has been estimated to about 9 km (Åström 1998) and the current topographic diameter to 6-7 km (Bottomley et al. 1978). The energy required to generate a crater of this magnitude corresponds roughly to 1.17×10^4 Megatons TNT (calculated with parameters 2750 kg/m^3, 17m/s, 45 degrees; Marcus et al. 2010); more than 300 000 times the TNT equivalent of the bomb at Hiroshima (Kerr et al. 2005). The latest dating of the structure was conducted with the ^{40}Ar-^{39}Ar-method on melt rock samples and yielded an average age of 121±2.3 million years for the impact event (Bottomley et al. 1990).

3.1. Geology
The Mien lake is situated in the "Transscandinavian Igneous Belt" that stretches 1600 km from south-eastern Sweden to north-western Norway (Goodwin 2016), and the bedrock in the area consist of Precambrian granite and gneiss (1.8-1.4 Ga) intersected by
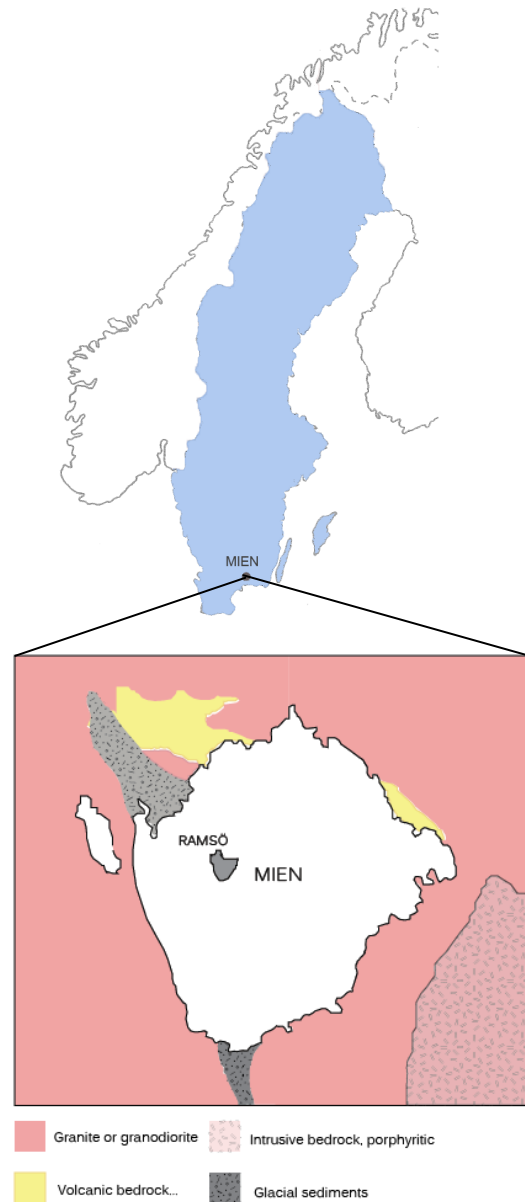

Figure 5. Map of Sweden and the location of Lake Mien. Close-up show dominating bedrock types in the area (Modified after Stanfors 1973 and SGU 2009).

diabase dikes (parallel to NNE; Stanfors 1969; Bottomley et al. 1978). The gneiss-granite is medium to coarse-grained and mainly constituted of quartz, microcline, plagioclase, biotite and hornblende, with minor sphene, zircon and apatite. Secondary constituents are chlorite, epidote and sericite (Stanfors 1969). The depression is filled by glaciofluvial deposits from the last glaciation (Svensson 1969); the moraine is generally only a few metres thick and immediately overlays the impact melt rock (Fig. 6A) in the central parts of the lake. The impact melt is more resistant to erosion than surrounding rock, and is seen as an elevated area on topographic maps (former central uplift) (Åström 1998). The depth in the lake generally varies between
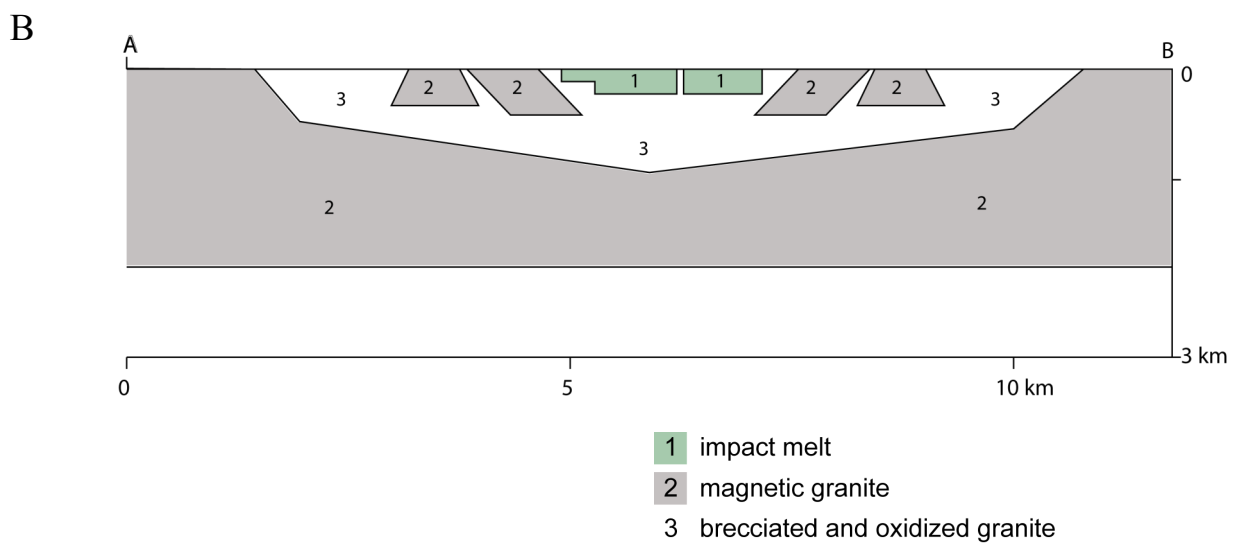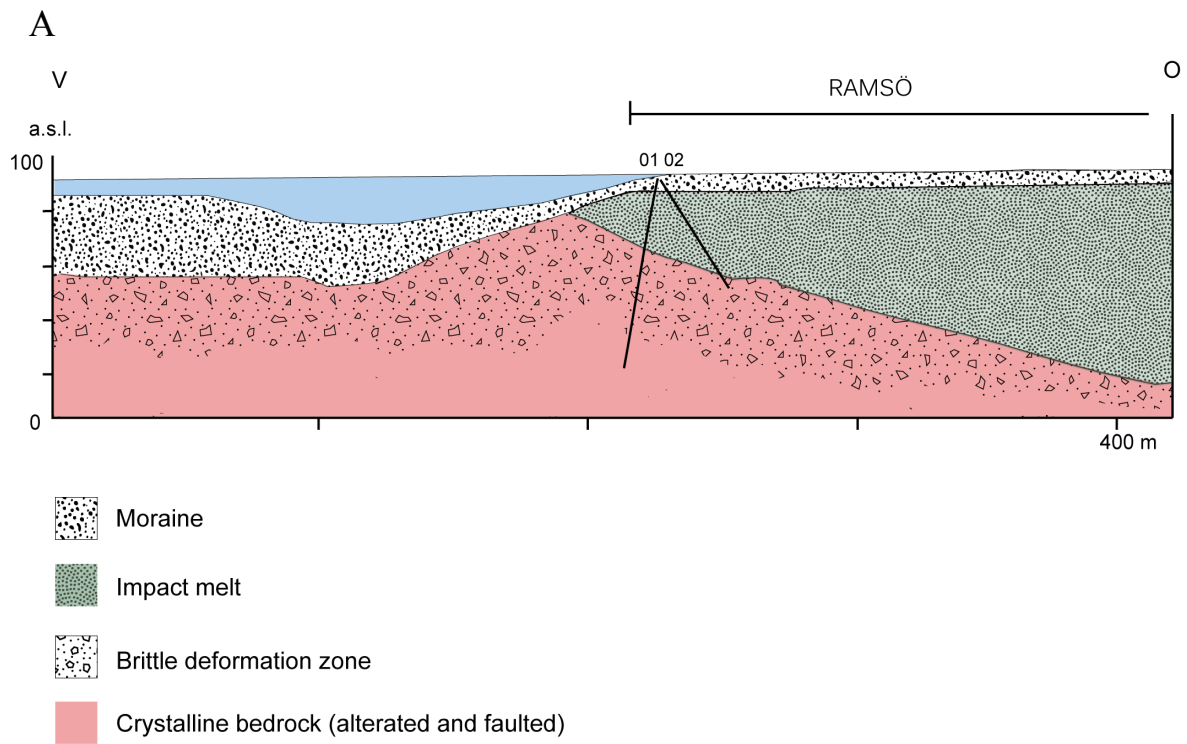
A

V

RAMSÖ   O

a.s.l.

100

01 02

0

400 m

Moraine

Impact melt

Brittle deformation zone

Crystalline bedrock (alterated and faulted)

B

A   B

3   2   2   1   1   2   2   3   0

3

2   2

3 km

0   5   10 km

1   impact melt

2   magnetic granite

3   brecciated and oxidized granite

Figure 6. A: Horizontal profile of a part of the lake and locations of drill-core 01 and 02. B: profile over the entire formation constructed from magnetic measurements (Modified from Stanfors 1969 & 1973 and Henkel 1982).

Figure 7. Drill-core logs of 01 and 02. Their location is marked in fig 6a (Modified from Stanfros 1969).

commonly as rhyolite ("Mien-rhyolite"; Stanfors 1973), and have a composition close to the target rock (Stanfors 1973; Henkel 1982). The term suevite recurs in several sources (Henkel 1982; Åström 1998), but its definition has recently been a subject of considerable debate (Osinski & Grieve 2017), why I choose to refer to these rocks as "suevite" breccia.

3.2. Materials and methods

Impactites of different lithologies were collected during an expedition to Mien in early fall 2017 (Fig. 8). These were found around the lake as loose rocks and in one old open-pit as a part of the moraine in the area. One un-shocked sample was collected close to the lake but outside the impact structure area (56.368815°N 14.856186°E) a thin section from this rock was made as a reference sample. Three impactites of different lithologies were chosen for further investigation: *Clast-rich impact melt rock;* an impact-melt rock with light coloured clasts surrounded by a dark fine-grained matrix. Shock textures in thin section include ballen quartz (with undulose extinction), and PDFs in quartz. *Clast-poor(er) impact melt rock;* an impact-melt rock similar to the clast-rich rock but with fewer clasts. Shock textures in thin section include ballen quartz (with undulose extinction) and PDFs in quartz. *"Suevite" breccia or melt-bearing breccia;* the matrix is fine-grained with inclusions of crystalline rock (light-coloured, ≤5 cm) and smaller devitrified melt fragments (dark-coloured, <1cm). The rock fragments originate from the host rock and are thus of granite composition. Shock textures in thin section include PDFs in quartz, shocked feldspar with "ladder texture" and melt fragments.

To enable identification of shock textures, backscatter electron (BSE) – and secondary electron (SE) images were obtained of manually separated zircon grains. The samples were prepared by manual crushing using a sledge hammer and a swing mill resulting in a fine-grained powder and loaded to a Wilfley-Holman 700 water-shaking table in order to separate heavy minerals according to the method by Söderlund & Johansson (2002). The residual was moved to a petri dish where magnetic minerals were removed using a magnetic pencil and zircon grains were handpicked using a pipette and a binocular microscope. The grains were then transferred and mounted on carbon tape. To describe exterior shock-metamorphic features, SE and BSE imaging was carried out with a Tescan Mira3 High Resolution Schottky FE-SEM equipped with Oxford EDS and EBSD system and a CL system located at the department of

2-20 metres with the deepest point being 42 metres, located northeast of the Island Ramsö (Stanfors 1969).

The only outcrops available in the area are gneissic granite, why four drillings were carried out in year 1973 at the small island Ramsö in the northwestern part of the lake (Fig. 6A & 7). Bore holes were drilled right over a positive magnetic anomaly, later shown to be the result of remnant magnetization in the impact melt sheet (Henkel 1982; Henkel 1992). The melt sheet was estimated to a diameter of 2 km and a thickness of 200 m (Fig. 6B). The drill-cores (Fig. 7) show that the rock above the crystalline basement consist of more or less shock-metamorphosed layers, mostly of impact melt (20-25 m), but also a small horizon of "suevite" breccia and brecciated granitic gneissic layers (Stanfors 1969; Stanfors 1973). The impact-melt rocks have previously been classified as lava-like rocks (Stanfors 1969), the less specific "Mienite" (Henkel 1992; Åström 1998) and most

Geology, Lund University, Sweden. The same equipment and settings were used for studies of internal textures after grains had been cast in epoxy and polished to mid-plane.

One grain from a thin section of the clast-poor impact melt rock was selected for SEM-EBSD analysis with the aim of obtaining data on crystallographic orientations of granules in granular zircon and to identify potential high pressure polymorphs. Due to time limits of this thesis, only one grain was examined with this method. The chosen thin section contained the most suitable granular grains for the purpose - and this particular grain was used because of its good quality, relatively large size and fully granular texture. To get good quality data, the thin section had to be polished with colloidal silica and then coated with a ~5 nm thick carbon layer. Softwares Mambo and Tango (included in the Channel 5 software from Oxford instruments) were used for post-analysis, i.e. the construction of pole figures and an orientation map. Data was cleaned up by noise-reduction i.e. "wild-spike" that replaces single mis-indexed pixels with neighbour zero solution extrapolation.

Four grains were examined with Raman spectroscopy located at the department of Biology at Lund University with the aim of identifying compositional differences between shocked and unshocked zircon from both in- and outside the impact structure, respectively. An unrelated perfectly crystalline zircon grain from the Varberg charnockite was used as a reference sample. Spectra were acquired in the range ~100-1100 cm^{-1} to cover main zircon frequency peaks, and the laser was set to 532 nm. Slightly different settings of accumulations and ND filter were used during round two. Detailed operating settings of both Raman and EBSD can be found in Table 3 and 4.
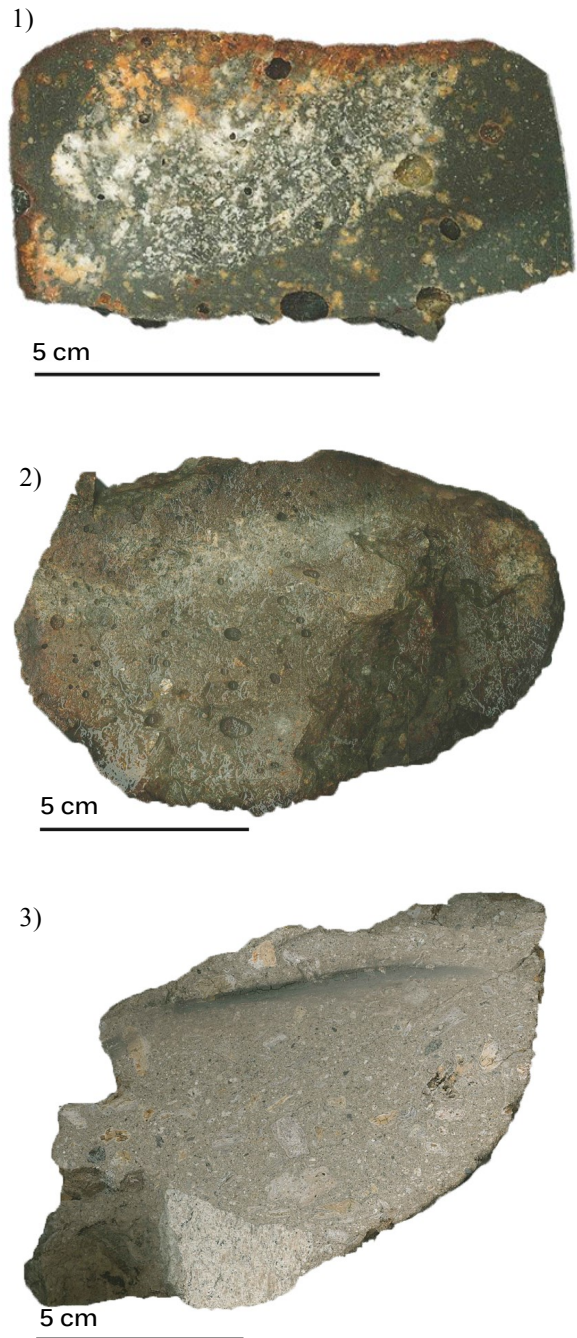

Figure 8. Left: photos from the expedition to Mien, collection of impactites. Above: Three impactites used in this study 1) clast-rich impact melt rock; 2) clast-poor impact melt rock with a fairly homogenous fine-grained matrix; 3) "suevite" or melt-fragment breccia.

16

3.2.1 .Operating settings

Table 3. Operating settings for Raman analysis, slightly different settings were used during round two (marked *).

Settings Raman (shocked zircon)	
Instrument	LabRAM HR Evol
Acq. time (s)	2
Accumulations	2/10*
Range (cm-¹)	100-1100
Binning	1
Objective	x100
Grating	1200 gr/mm
ND Filter	50%/25%*
Laser (nm)	532

* Second analysis of Varberg charnockite zircon and zircon outside the Mien impact structure

Table 4. Operating settings for SEM-EBSD

SEM	
Model	Tescan Mira3
EBSD acquisition system	Oxford instruments Aztec
EBSD processing software	Channel 5.10
Acceleration voltage (kV)	15
Working distance (mm)	15
Tilt (deg) - EBSD	70
Carbon coat (nm)	<5
EBSD match units	
Zircon	Am.Mineral (1979)
Baddeleyite	JACGAR (1996)
Reidite	Reidite 30.88 Gpa (CRY-file created with data from MinCryst infocard 2004)
EBSP acquisition, indexing and processing	
EBSP acquisition speed (Hz)	2.5
EBSP background (frames)	64
EBSP binning	4x4
EBSP gain	High
Hough resolution	60
Band detection	8
Step size (μm)	0.3
Number of points	55488
Mean angular deviation (MAD)	
Zircon	0.74
Baddeleyite	1.25
Reidite	1.15
Softwares	Mambo, Tango
EBSD noice reduction routine	
Wildspike correction	Yes
Nearest neighbour zero solution extrapolation	Yes

4. Results

4.1. Microfeatures

A total of 257 zircon grains from the clast-rich impact melt rock (n=123), clast-poor impact melt rock (n=75) and the "suevite" breccia (n=88) were sampled and studied. From these, a total of 131 grains were recovered and polished to mid-section.

SEM imaging revealed two dominating features: granular (e.g. Bohor et al. 1993; Wittmann et al. 2006) and microporous texture (e.g. Dempster & Chung 2013; Zhang et al. 2011; Singleton et al. 2015). An explanation of how the division of textures was made is described in Table 5. More than two thirds of the grains from the impact melt rocks contain micropores, as opposed to the "suevite" breccia where less than one-third have this feature (Diagram 1 and 2). In all rock types, micropores were more frequently occurring as an interior texture.

Granules were identified at the surface of approximately one third of the impact melt rock grains, and the texture can be penetrative since granules also occur within polished grains. Only ~19% of "suevite" breccia grains have granular texture, and when found, both size and distribution of the granules is generally smaller than in the other two lithologies. The occurrence of both textures within the same grain is more common in the impact melt rocks than in the "suevite" breccia. A complimentary cathodoluminescence (CL) imaging was performed on one granular grain from the clast-rich impact melt rock (Fig. 13H), revealing no internal zonation pattern. Taken together, the two textures occur more frequently in the impact melt rocks than in the "suevite" breccia, with a slight difference between the two impact melt rocks.

Zircon from the granite sample obtained outside the impact structure did not exhibit any shock features. Uranium-rich bright spots were detected with energy-dispersive x-ray spectrometry (EDS; section 4.3.). All SEM images are included in the appendix.

Table 5. Short descriptions of microfeatures and a reference guide to figures.

| Microtextures	Figure no.			Description
	Clast-rich	Clast-poor	"Suevite"	
1 Granular	9	13	15 A-C	Clusters of polycrystalline aggregates either confined to a minor area of the grain or covering the entire grain (e.g. Wittmann et al. 2006). Granules may be as small as <1μm each.
2 Microporous	10	14 C-D		A spongy (Yang Liu et al. 2015) and generally inclusion-poor type of texture. Pores may be confined into separate domains with smooth surroundings. They also occur as "trails" and together with other micro-features.
3 Linear features	10 E-L		15 D-E	Some grains have planar features, either as trails of pores or as planar microstructures.
5 Other	11, 12	14 E-J	15 F-K	Examples include: marks or fractures that occur in noticeable patterns. These marks can be small isolated areas or cover a large portion of the grain. Several grains, especially in the "suevite" breccia contain a surface texture of grooves and/or "furrows".
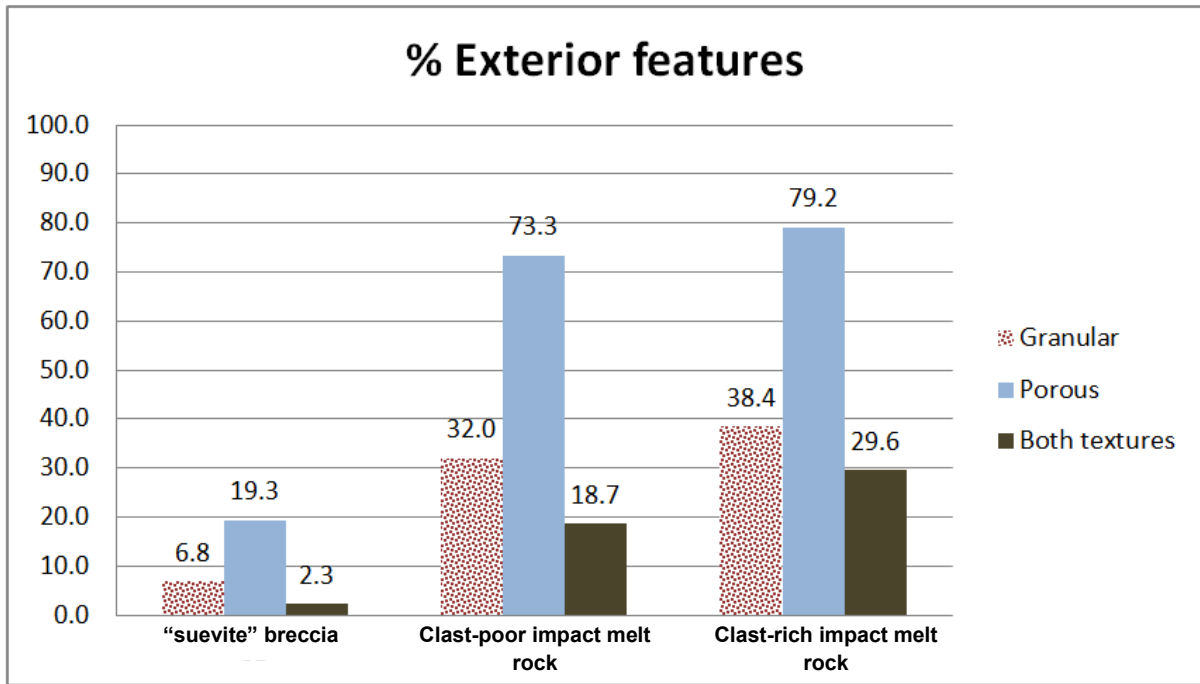
Diagram 1. Percentage of grains from the analyzed samples that display granular and/or microporous exterior texture. Both features can occur within a single grain, thus the total percentage of each lithology may exceed 100%.
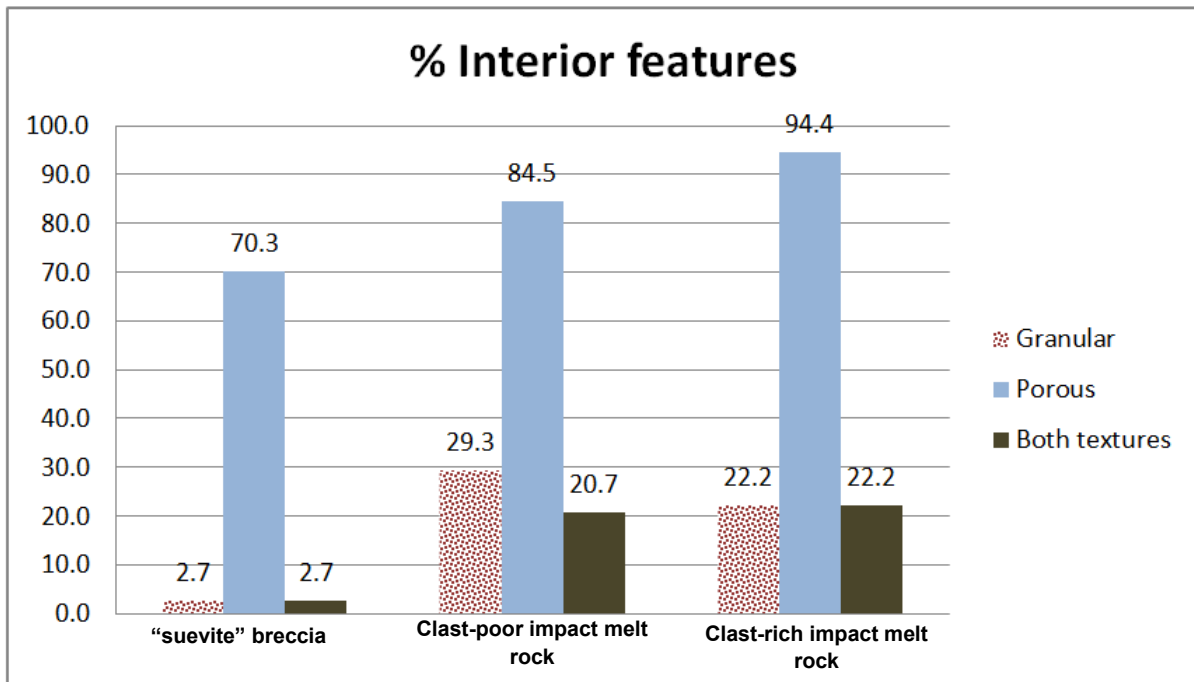

Diagram 2. Percentage of grains from the analyzed samples that display granular and/or microporous interior texture. Both features can occur within a single grain, thus the total percentage of each lithology may exceed 100%.

4.1.1. Clast-rich impact melt rock

Forty-eight of the total 123 zircon grains are either fully granular or contain clusters of granules (Fig. 9A-K). Ninety-nine zircon grains contain micropores, making this the most common shock-feature (Fig. 10A-L). Pores can be aligned as trails or confined to specific areas or patches; an example of the latter is seen in Figure 10D - this grain is relatively euhedral with smooth areas surrounding the porous patches. Thirty-six grains were studied for interior textures; micropores are present in almost all grains either as trails or patches, making this the most common feature in both polished and unpolished samples.

GRANULAR

Two representative grains with a fully granular texture are shown in Figure 9A and C, the size of single granules is generally 1-5µm and the shape is rounded to elongate. Three granules differ from the other by their euhedral shape and length of ~5µm; these can be seen in the close-up image (Fig. 9D). Grain in Figure 9K is a grain fragment with a fully granular texture with granules varying in size between 1-4µm.

Grains in Figure 9B and 9E-J are examples of partly granular grains, meaning that the surface contains either one or several clusters of granules, e.g. in Figure 9E-G where they are located at the absolute edge of one of the tips of the grain, or as in Figure 9B where they form a larger granular region at the upper part of the grain, adjacent to a homogenous area; the granules appear less distinctive in the contact to this area. The size of single granules ranges between <1µm (Fig. 9E-G) and up to 5µm (Fig. 9B). Grain in Figure 9H is rounded with fractures radiating out from one point at the upper part. Granules occur where the fractures intersect (see arrow), and have a size of ~4µm. The surface also contains micropores. The interior has a "spongy" texture (Yang Liu et al. 2015). Grain in Figure 9I is rounded and contain small, <1µm, granules that are concentrated along fractures at the right part of the grain. The left part of the grain is homogenous and smooth. The interior of the grain has a spongy texture similar to that of the grain in Figure 9H. Grain in Figure 9J contain granules at the upper part and as seen in the close-up, granules have rounded but irregular shapes and are poorly defined. The rest of the grain is relatively smooth.

MICROPOROUS

Grain in Figure 10A is a rounded elongated grain with deep "ring-shaped" fractures surrounding a porous patch.

Three representative grains with microporous patches are shown in Figure 10B-D. Grain in Figure 10B and C are both are rounded grains with one microporous domain with a size of ~17µm (Fig. 10C) or more (Fig. 10B) that has a gradual boundary to the surrounding surface of the grain. The rest of the surface is homogenous without notable fractures. Grain in Figure 10D is euhedral and has at least four distinct rounded microporous patches. Fractures are crosscutting the grain and a discontinuous fracture ranging N-S (shown by arrow) transforms into a trail of pores at the lower part as it encounters one of the porous patches.

Pores can also occur as isolated vesicles aligned as trails (Fig. 10F), or occur together with other features (Fig 10E and G). Grain in Figure 10E has a partly porous lower tip and except from one fracture, the rest of the surface is homogenous; noteworthy however is an elevated linear feature at the upper part of the grain following the longest axis (see arrow). Grain in Figure 10G is an elongated grain with deep parallel trenches following the longest axis of the grain. Within and adjacent to these are micropores. The rest of the grain surface is uneven and seemingly homogenous.

OTHER

Beside the two dominating textures (porous and granular) in this rock type, other conspicuous but less common textures will be described in this section. Planar microstructures and/or planar deformation features (PDFs) have been reported from zircon previously (Bohor et al. 1993; Erickson et al. 2013); four grains from the clast-rich impact melt rock show linear features but unlike pristine PDFs, these consist either of trails of pores inside the grains (Fig. 10H-I and L) or "bands" at the surface (Fig. 10K). Figure 10H and 10L are grain fragments polished to midsection, exposing several parallel lines consisting of pores or vesicles with a spacing between lines of <1µm. Grain in Figure 10L have at least five individual lines constituted by pores at the lower part of the grain (arrow), and in grain Figure 10I it is possible to identify three major lines, but these consist of larger pores than Figure 10L, and are slightly curved. One major fracture runs parallel adjacent to these trails. Grain in Figures 10K show the surface of a rounded grain that have "bands" or planar features that unlike the other two fragments (Fig. 10H and 10L), do not consist of pores. The planar feature consist of two elevated and homogenous bands with a width of ~2µm, and the close-up show where these intersect. The rest of the grain is homogenous and has one fracture going N-S to the left of the bands, and one deep fracture to the right of the bands.
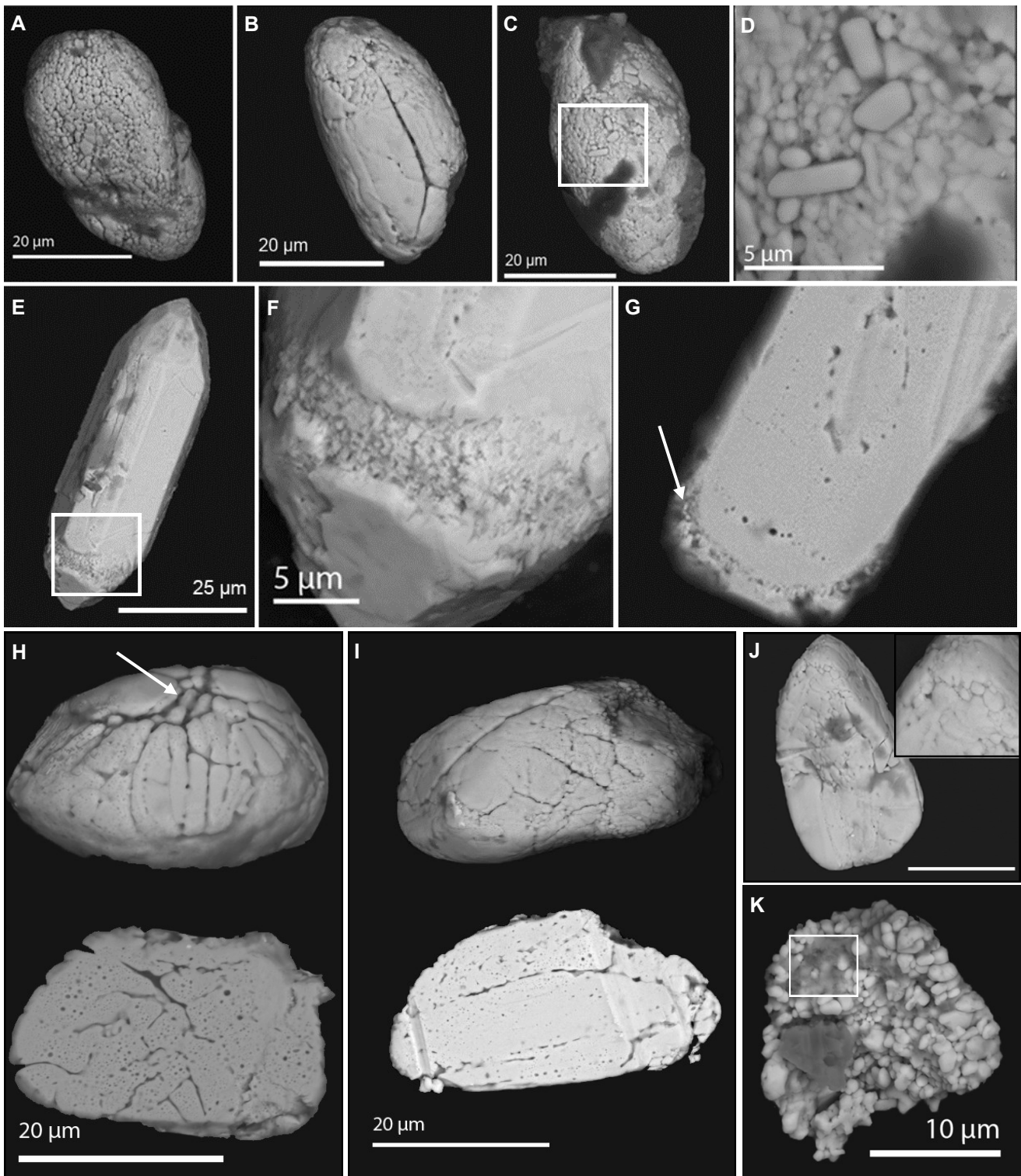
Figure 9. Compilation of backscatter images of fully granular or partly granular zircon grains from the clast-rich impact melt rock. A: Fully granular grain. B: Partly granular grain. D: Fully granular grain, close-up of three well-defined granules in D. E: Euhedral grain with granules at the lower tip. F: Close-up of granules from E, the white square marks the location. G: the same grain as in E-F but when polished to mid-section, granules are still visible (see arrow). H: Upper picture show the exterior of a grain with fractures radiating out from one point marked by the arrow. In between these fractures are large (~4μm) sized granules. The lower picture show the same grain when polished to mid-section. I: Partly granular grain, granules are confined to the right part of the grain, the lower picture show the same grain when polished to mid-section. J: Fully granular grain fragment. K: Grain with poorly defined granules at the upper tip, better seen in close-up.
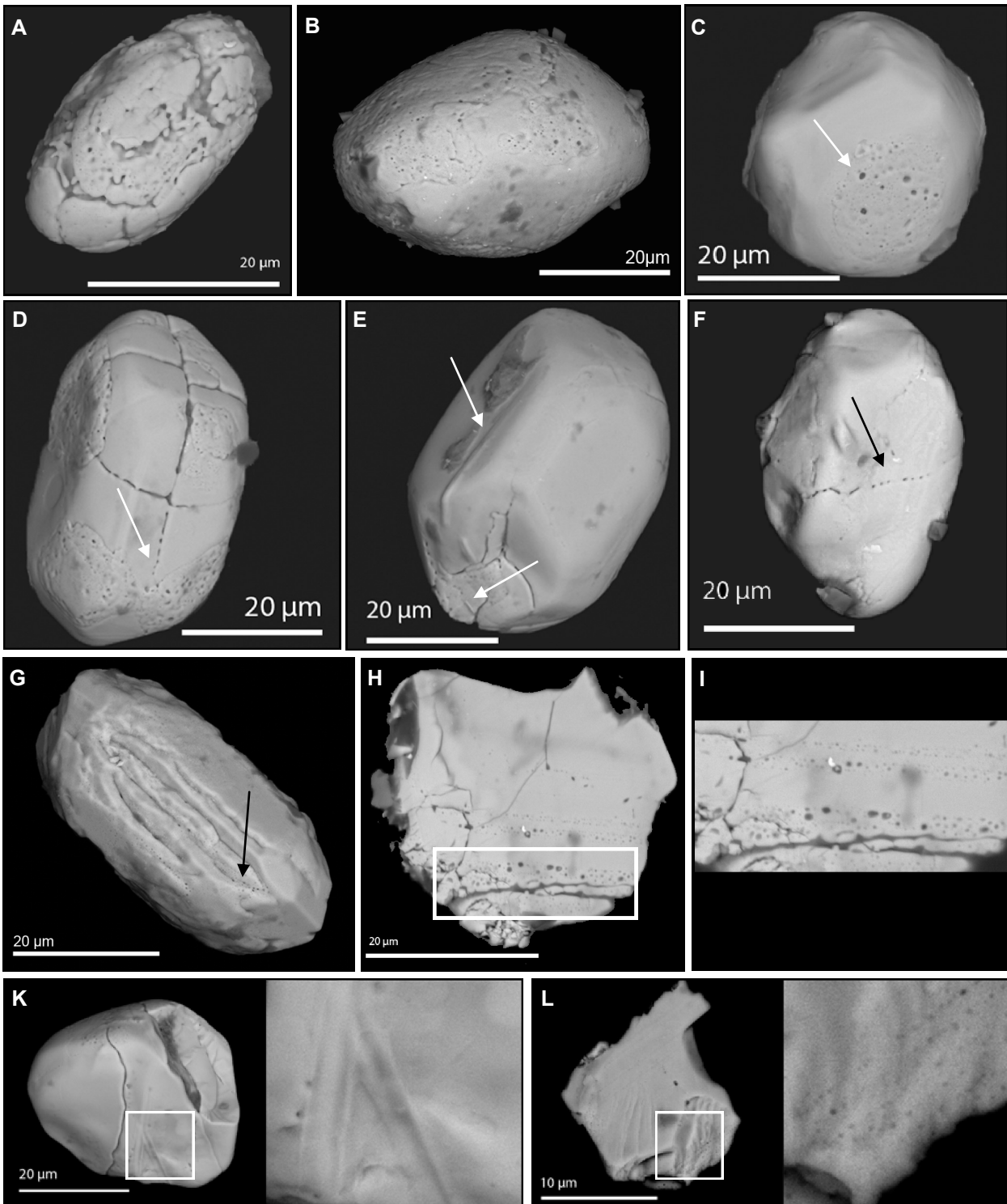
Figure 10. Compilation of backscatter images of zircon grains containing micropores from the clast-rich impact melt rock. A: Rounded grain with "ring-shaped" fractures and microporous texture. B: Rounded grain with porous patches. C: Rounded grain with one distinct porous patch (arrow). D: Euhedral grain with at least four distinct microporous patches. E: Grain with micropores at the lower tip (arrow) and an elevated features following the c-axis (arrow). F: Rounded grain with one trail of pores going E-W in picture (arrow). G: An elongated grain with deep parallel "trenches" containing micropores (arrow). H: Grain fragment with distinct trails of pores or vesicles at the lower part of the grain, better seen in the close-up, I: close-up of pores. K: Rounded grain with two planar "bands", the close-up show where these intersect. L: Grain fragment with at least 5 individual lines consisting of pores, better seen in the close-up.

Figure 11A-B show two rounded grains with microporous areas and conspicuous white specks, these have not been further analysed. The specks are forming clusters in both grains, in Figure 11A, the cluster is confined the lower part of the grain, adjacent to an upper microporous area; the contact between those can be seen in the close-up. The grain in Figure 11B consists of two "parts" divided by a fracture running NW-SE. The right side of the grain is fractured and porous, and the left side is homogenous apart from a cluster of white specks.

Two grains contain a distinct surface texture of small, rounded and seemingly homogenous elevations or "mounds" (Figure 12A-B). Grain in Figure 12A is an elongated grain with deep fractures at the upper left side of the grain and "mounds" at the lower part of the grain; this feature is shown in a close-up. Figure 12B have a similar texture, the grain is relatively euhedral with "mounds" at the lower left side of the grain (shown by arrow).

Grain in Figure 12C is a sub-rounded grain with separate "vugs" at the upper part of the grain, shown by the white arrow. Grain in Figure 12D is a rounded grain with several vugs similar to those in 12C, the rest of the surface has alternating smooth patches and porous texture, with a gradual boundary between the two textures. Grain in Figure 12E-F are close-ups of two grains showing a surface texture that consist of non-planar alternating shallow and deeper fractures.

4.1.2. Clast-poor impact melt rock
Almost a third of the total 75 zircon grains has granular texture (Fig. 13A-J and 14A-B), and 55 contain micropores (Fig. 14C-D). Other conspicuous textures include "furrows" (Fig. 14G) and crescentic fractures (Fig. 14J). The size of these textures ranges from just a few μm to larger coherent regions that covers the whole (visible) side of the grain. Remnants of these

textures were not observed in polished sections. Fifty-eight grains were studied for interior textures. A majority of these grains contain micropores (e.g. Fig. 13B) and almost a third contains some form of granular texture (e.g. Fig. 13G).

GRANULAR
Different types of granules are identified; Figure 13A-B show the same grain both when unpolished and when polished to midsection. It is an elongated grain with several exterior fractures, and granules are mainly concentrated at the center and the lower part of the grain. The granules are generally rounded and have a size <1μm, with a few exceptions where they are elongated and the longest axis can be ~1μm. Granules can occur both as isolated from the surrounding surface or gradually merge into other homogenous parts of the surface (see close-up). The upper part of the grain contains no granules and is fractured. The interior contains micropores or small (<1μm) vesicles that follow a distinct zonation pattern (Fig. 13B). Grain in Figure 13D is a close-up of fractures and granules adjacent to each other. Granules are generally elongated and between 1-5μm in length. Figure 13E-H shows a granular grain; in Figure 13E is the unpolished grain, with at least 50% of the surface having a granular texture. The other non-granular part is homogenous and the contact between these two areas is gradual. Granules have a size of ~1μm and varying shapes, the difference between the appearances of granules is best seen in 13F. A cluster with a width of ~2,5 μm of rounded granules (size of individual granules <1μm) run E-W in the picture. Above and underneath this region are larger elongated granules, with their longest axis seemingly parallel to that of the host grain. In the close-up are also examples of homogenous areas and the transition between these and the granules (arrows). Figure 13G show the interior of the grain is completely granular. In Figure 13H is a CL-image of the interior that is homogenous. Grains in Figure 13I-J and in Figure 14A-B both contain granules with a size of <1 μm and mi-
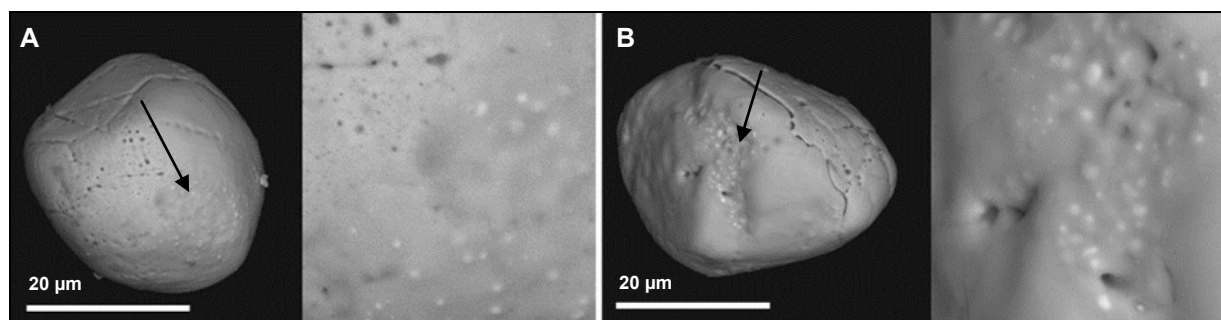

Figure 11. Backscatter images of two zircon grains from the clast-rich impact melt rock. Both A and B contain clusters of white "specks" (arrows).
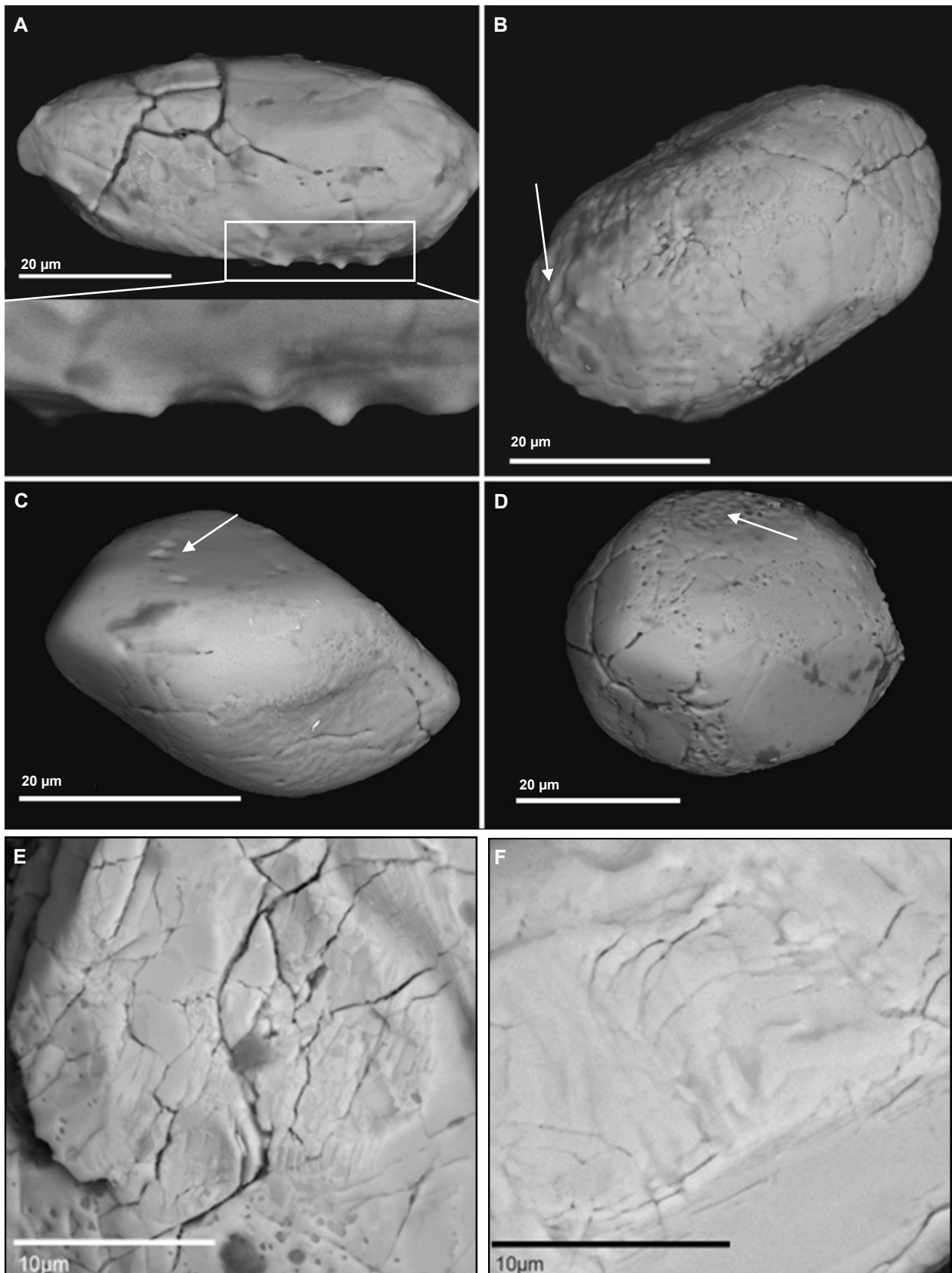
Figure 12. Compilation of backscatter images of zircon grains from the clast-rich impact melt rock. A: Rounded and elongated grain with a surface texture of small, seemingly homogenous "mounds" at the lower part of the picture, better seen in the close-up. B: a grain with "mounds" similar to those in picture A (arrow), the rest of the grain is fractured. C: Grain with three distinct "vugs" at the upper part (arrow). D: Grain with several "vugs" similar to those in C, the rest of the grain contain pores and fractures. E: Close-up of a surface texture consisting of non-planar fractures. F: surface texture of non-planar fractures, similar to E.

24

cropores at the surface. Grain in Figure 13I-J is an angular and fractured grain with granules at the upper part of the grain (see close-up). The granules follow a distinct line separating them from the outermost part of the grain. Grain in Figure 14A is an elongated grain with fractures, the most distinct fracture is located at the lower part of the grain (close-up Fig. 14B) and contain small granules with a size of <1μm.

MICROPOROUS

Porous grains in this sample are similar to those in the clast-rich impact melt rock. One grain from the clast-poor impact melt rock is shown in Figure 14C-D; the exterior of this grain is anhedral and relatively smooth with few fractures, and the interior has a "euhedral" core that appear homogenous, surrounded by a microporous outer rim.

OTHER

Grain in Figure 14E is an elongated euhedral grain with several distinct surface features; the central part consist of one (or possibly two) homogenous regions, surrounded by a porous or "spongy" texture. Grain in Figure 14F is a grain fragment with a crinkled web-like surface texture.

The clast-poor impact melt rock contains several grains with different types of conspicuous "furrows" at the surface. This texture is best expressed in Figure 14G, where the close-up shows that the main direction of furrows is N-S (with a spacing between furrows of <1μm) and that they are intersected by smaller perpendicular furrows. Grain in Figure 14H is rounded and contain both granules in and along one of the deeper fractures, the close-up show some of these granules and a patch with small (<1μm) irregular grooves. Grain in Figure 14I is a rounded grain with small pits and fractures, the close-up show a smooth "band" next to these small fractures (<1μm in length) at the surface. One distinct fracture is filled with a brighter material that has not been analysed. Grain in Figure 14J is a relatively euhedral grain with crescentic marks or fractures at the upper part of the grain, shown in close-up.

4.1.3. "Suevite" breccia

Of in total 88 zircon grains, more than half of the grains have a surface texture resembling "corrosion", best described as grooves with irregular rims (Fig. 15G -I), that only occurs in the "suevite" breccia. The texture can resemble pores, but "corrosion" marks are generally larger, shallower and has uneven margins. Micropores do occur in some grains but not as fre-

quently as in the two impact melt rocks. Six grains contain granular texture and only one grain is entirely granular (Fig. 15A-C); other grains have more subtle granular patches. One set of planar fractures (PFs) occur in two grains (Fig. 15D-E) with a distance of ~3μm between PFs. A total of 37 zircon grains were polished to midsection and from these, almost a third lack obvious shock features. Compared to the unpolished grains (19%) a very high percentage of the interiors (70%) contain micropores. Micropores are generally are generally less well defined and occur in smaller patches than in the impact melt rocks. Only one grain has an interior granular texture.

GRANULAR

Grain in Figure 15A-C has an exterior and interior granular texture. Granules are confined to the center of the grain, with a gradual boundary to the surrounding, which is fractured and anhedral. The close-up image show a SE-image of the exterior, with granules having a size of <1μm. As seen in this image, granules also seem to occur within one the major surface fractures.

OTHER

Two grains contains PDFs or PFs (Fig. 15D-E). Grain D in the figure is an angular fragment with at least four visible straight lamellae aligned in N-S, with spacing between lamellae of ~2-5μm. Grain E in the same figure is a rounded grain with one visible set of PFs, marked with an arrow. Figure 15F-K is a compilation of grains with conspicuous surface textures. Grain in Figure 15F is a grain fragment with rounded elongated pits ~3μm in length with "tails" (see close-up) covering most of the surface. Figure 15G-I show grains with marks typical for the "suevite" breccia. In Figure 15G, is a euhedral grain with irregular vugs at the surface. A similar feature is seen in Figure 15H-I where the marks are seemingly shallower coherent areas with irregular (Fig. 15H) or "lobate" rims (Fig. 15I). Figure 15J show a euhedral grain where a part of the original surface is missing, this area contains poorly defined micropores. Grain in Figure 15K is a rounded grain with irregular fractures at the surface crossing each other at different angles. Four main parallel fractures extend N-S, and from these, smaller and narrower fractures are branching out.
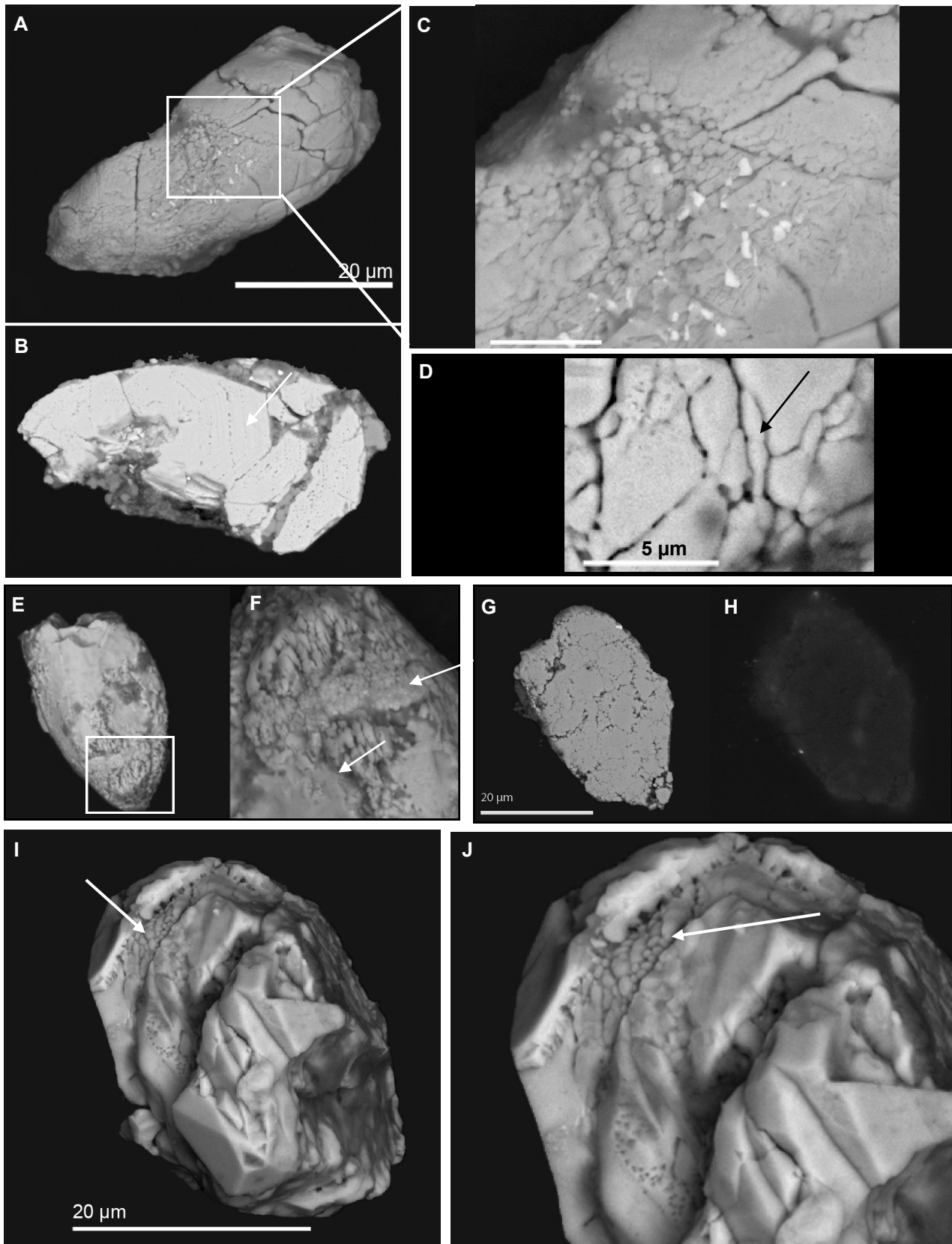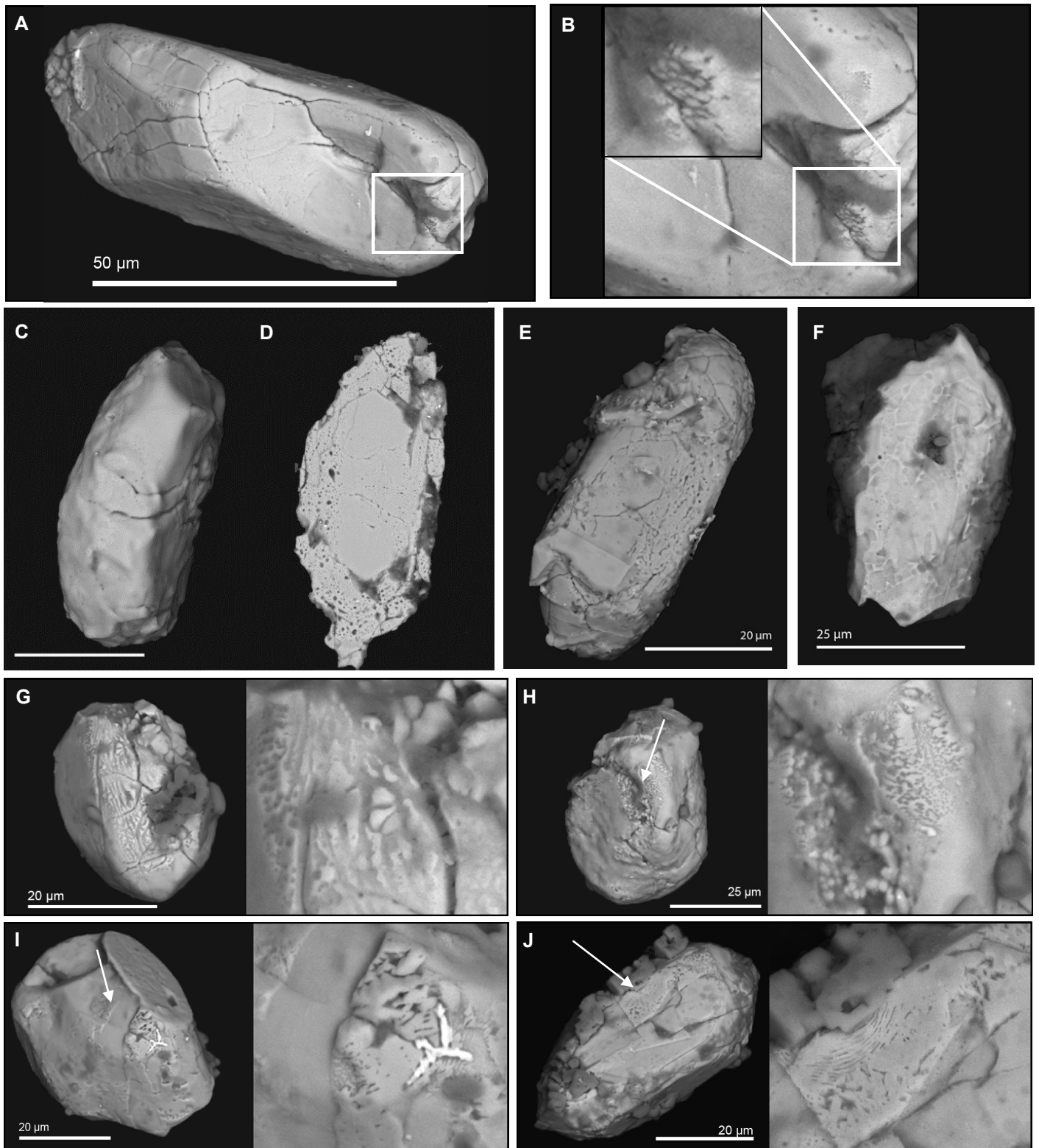
Figure 13. Compilation of backscatter images of granular zircon grains from the clast-poor impact melt rock. A: Elongated grain with granular texture. B: The interior of the grain in A, showing micropores following a zonation. C: Close-up of granules from A. D: Close-up of a grain containing granules in between fractures. E: Partly granular grain, the upper part is homogenous. The white square marks the location of the close-up. F: Close-up of granules, a band of <1µm-sized granules crosscut larger granules. G:The interior of grain E, showing a fully granular texture. H: The same grain in CL, showing no interior zonation. I: Angular grain fragment with granules following a distinct "line" separating them from the outermost part of the grain (arrow). J: Close-up of the previous grain, the arrow show granules.

26

Figure 14. Compilation of backscatter images of zircon grains with various textures, from the clast-poor impact melt rock A: Elongated grain with granules in a fracture, white square show location of close-up. B: Two close-ups of granules from previous image. C: Grain with a exterior surface that is anhedral and relatively smooth with few fractures. The interior of the grain (D) has a "euhedral" core that appears smooth and homogenous, surrounded by a microporous outer rim. E: An elongated grain where the central part consist of one (or possibly two) homogenous regions, surrounded by a porous or "spongy" texture. F: a grain fragment with a "crinkled" surface texture. G: Rounded grain with "furrows". H: Rounded grain with granules adjacent to a patch with µm-sized grooves. I: Rounded grain with a "smooth" band (arrow and close-up), and small fractures. J: grain with crescentic marks or fractures.
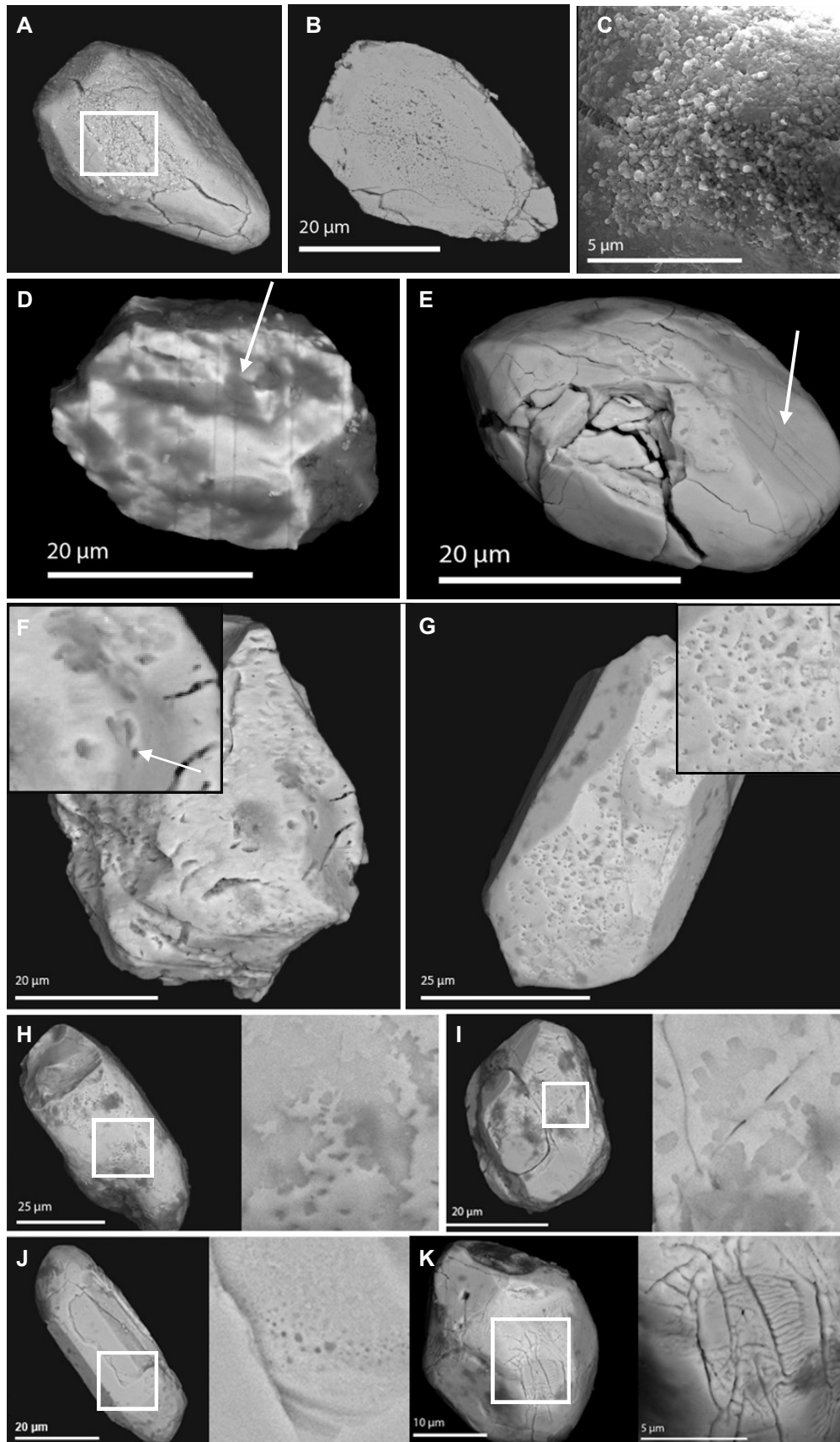
Figure 15. Compilation of backscatter images of zircon grains with various textures, from the "suevite" breccia. A: Granular grain, white square mark the location for the close-up. B: The same grain polished to mid-section, exposing granular texture at the center of the grain. C: close-up of granules from the same grain as in A-B. D: Grain fragment with planar microstructures ranging N-S in the image. E: Grain with one set of planar microstructures (arrow). F: Grain fragment with small pits with "tails", an example is shown in the close-up with the arrow pointing at the tail.. G: Euhedral grain with irregular vugs at the surface. H: Grain with shallow coherent areas with irregular rims. I: Surface texture similar to that in H, but the shallow areas have rounded rims. J: Elongated euhedral grain with a part of the surface "missing", this area contain poorly defined micropores. K: Rounded grain with irregular fractures.

4.2. Thin sections

Thin sections from all rock types were studied in optical microscope, Figure 16 show one representative quartz grain from each lithology. Quartz with "ballen" texture and quartz with PDFs were found in both impact melt rocks. Figure 16A show a quartz grain from the clast-poor impact melt rock with "ballen" texture, consisting of "spheroidal" shapes adjacent (or penetrating) to each other; size of individual "ballen" ranges between ~50-100 μm. Figure 16B is a quartz grain from the clast-rich impact melt rock, displaying at least 2 sets of PFs, with a spacing between lamellae of ~50 μm. Figure 16C is a quartz grain from the "suevite" breccia with at least 2 sets of PDFs, with spacing between lamellae of <5μm.

4.3. Energy dispersive x-ray spectrometry (EDS) analyses

EDS-analyses were made with the objective of 1) establishing the composition of different types of bright spots, and 2) detecting differences between a seemingly homogenous area and a surrounding porous rim. These features were first identified during SEM imaging.

Elemental spectra were acquired from two grains containing bright spots; 1) from an unpolished grain from the clast-poor impact melt rock (Fig. 17A) with a bright inclusion, and from 2) a grain obtained outside the Mien crater area, with brighter domains visible in SEM (Fig 17B). The EDS spectral analysis showed that the bright areas contain uranium, whereas the darker domains do not. EDS-analysis was also conducted on one granular grain from a thin section of the clast-poor impact melt rock, where several granules contained white inclusions (Fig. 18). As seen in Figure 18, granules with inclusions are localized along the rims of the grain or close to voids inside the grain. The analysis showed that the Si is lower in the bright spots, confirming a ZrO_2 phase (Fig. 18).
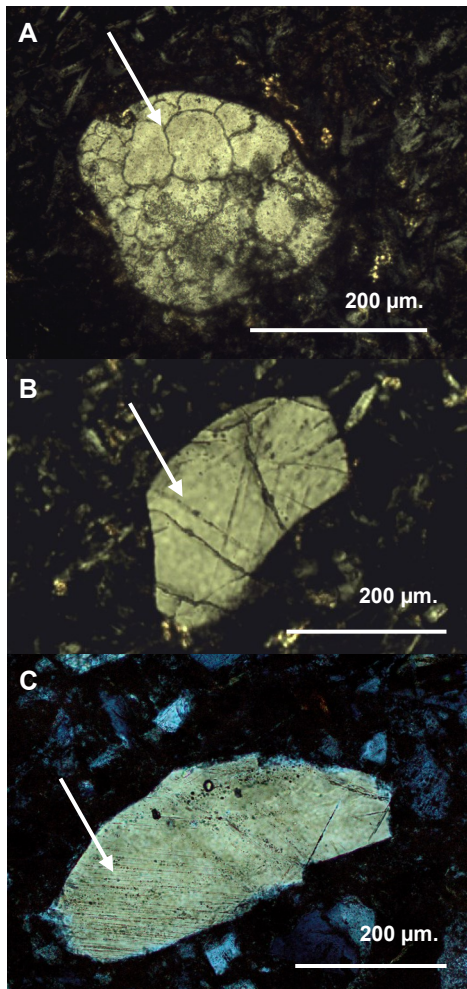
Figure 16. Close-up of thin sections. A: quartz grain from the clast-poor impact melt rock, displaying "ballen" texture. B: a quartz grain from the clast-rich impact melt rock with two sets of PDFs. C: a quartz grain from the "suevite" breccia displaying PDFs.
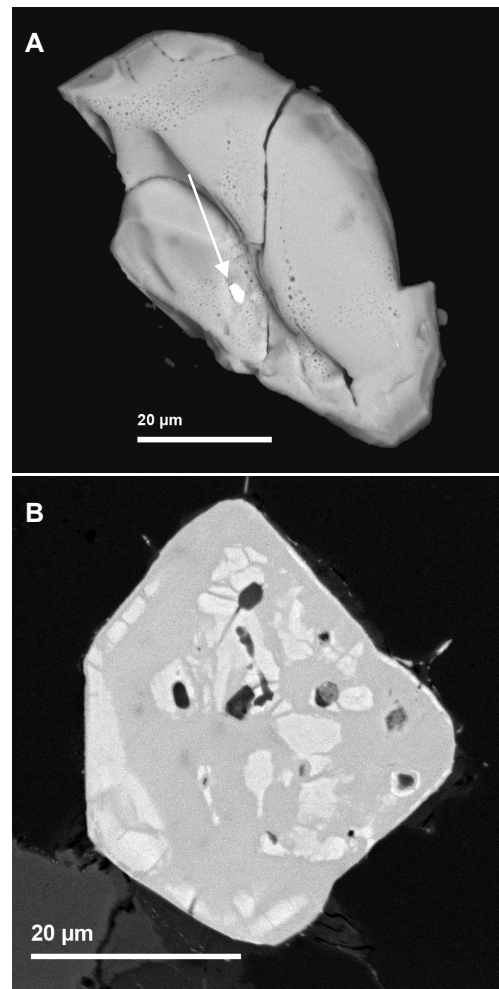
Figure 17. BSE images showing, A: grain from the clast-poor impact melt rock with a white inclusions showing U-peaks (black arrow). B: grain from outside the affected crater area, lighter areas has U-peaks.
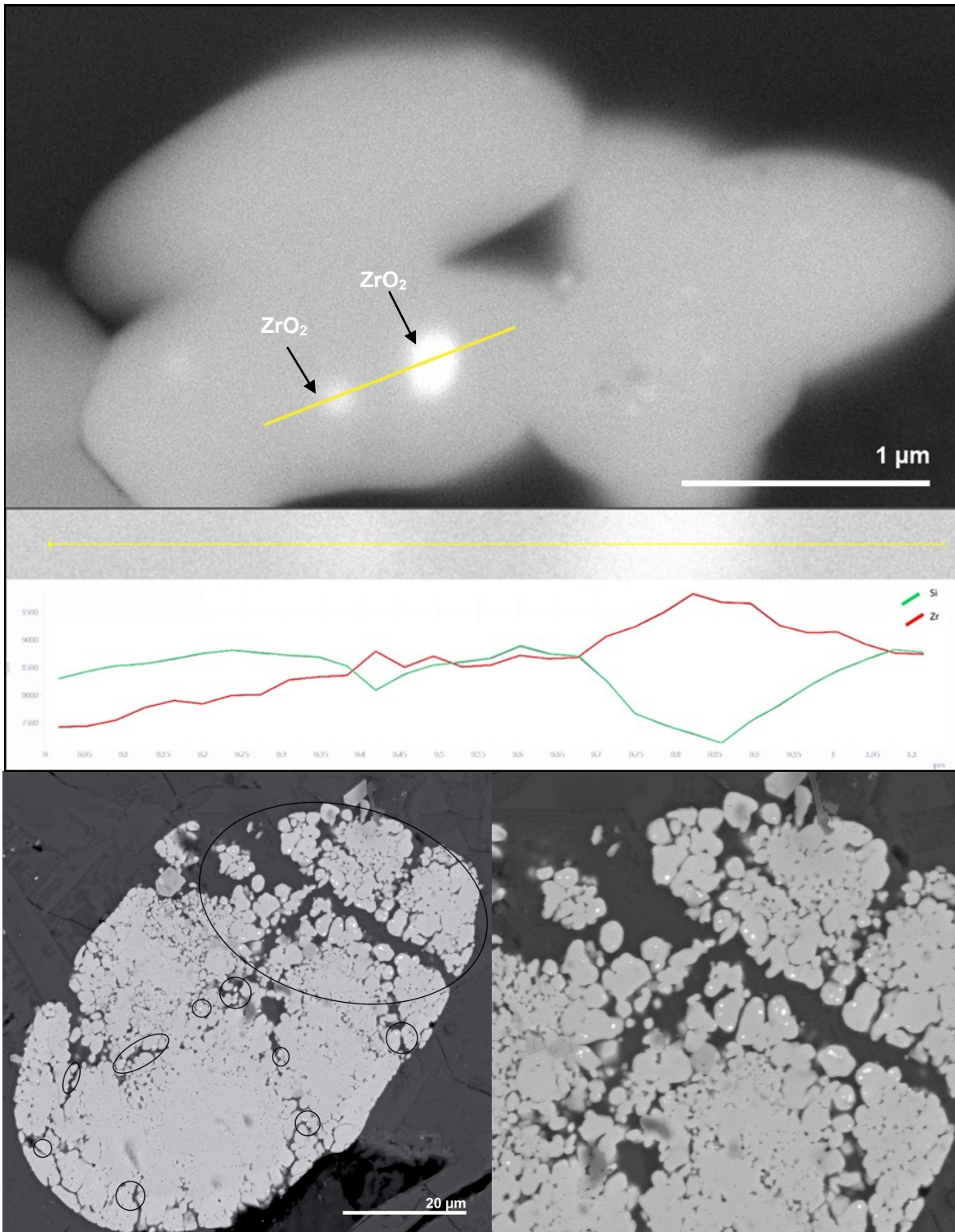
Figure 18. BSE image of a granular grain in a thin section from the clast-poor impact melt rock. EDS analysis of white inclusions in granules (yellow) show that these inclusions have a lower Si-content and higher Zr-content than the surrounding. Due to the small size of inclusions, the analysis will be affected by the surrounding why Si is indexed in the spectra. Picture to the lower left shows a granular grain from the same thin section with several white inclusions. The black circles indicate the location of some clusters of inclusions that are generally located at the rims of the granules and along "voids". The picture to the lower right is a close-up of the area inside the black circle.
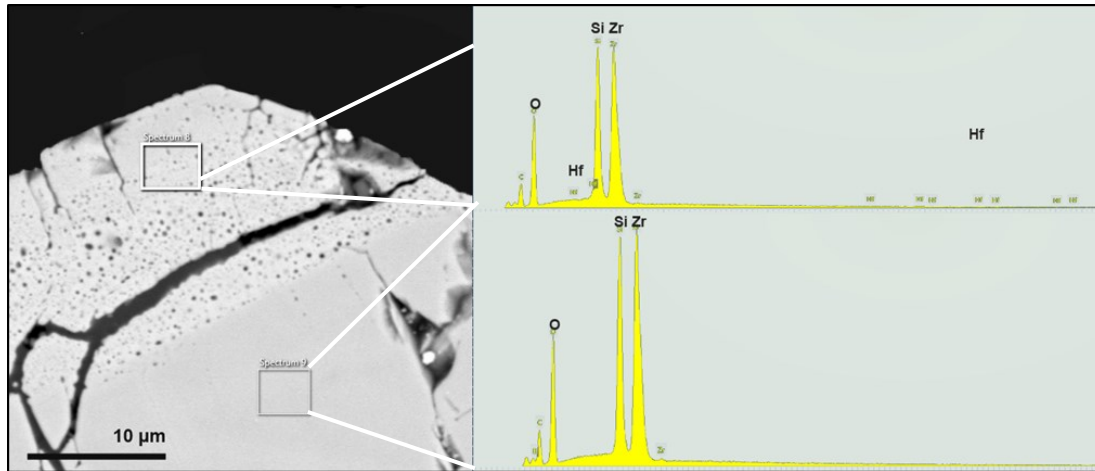
Figure 19. EDS mapping was conducted on a partially porous grain from the clast-poor impact melt rock. Two sites were analyzed – one porous and one homogenous. The two spectra show that the porous area has Hf-peaks whereas the homogenous area does not show these peaks.

Figure 19 show a partially microporous grain with a homogenous core and porous rims where both textures were analyzed for elemental differences. The only noticeable difference between those two spectra is that the porous rim contains hafnium.

4.4. Electron backscatter diffraction (EBSD)

EBSD analysis was conducted on a fully granular grain, 60 μm across longest axis, found in a thin section of the clast poor impact-melt rock. An orientation map with IPF (inverted pole figure) coloring scheme was constructed from obtained data (Fig. 20), and shows a systematic relationship of the neoblasts, seen in pole figures as three clusters of 90° perpendicular crystallographic orientations with coincidence between and (001). Previous EDS-analysis of the grain did not detect other phases than zircon, however, this specific orientation relationship is indicative of the transformation of and reversion from reidite to zircon (Cavosie et al. 2016), so called "Former reidite in granular neoblastic zircon" (FRIGN zircon; Cavosie A. J. et al. 2018). Neoblasts aligned with (110) (blue in EBSD map) are comprised of clusters of granules with a size of up to 15 μm. Individual granules has a size varying between 1-7 μm when measuring their longest axis, and some scattered neoblasts have a size <1 μm. Misorientation plots show that clusters with angles between 85°-95° coincide with pole (110). Local lack of EBSD pattern is due to holes between granules.

4.5. Raman spectroscopic analysis

Raman spectroscopy was conducted on four zircon grains

(Table 6); two from the clast-poor impact melt rock (Fig. 21) - each chosen as representative from their respective texture category - one from outside the crater area and one perfectly crystalline from the Varberg charnockite (Fig. 21) used as a reference sample.

Approximately 20 spectra were obtained for each analyzed site in the porous and the granular grain. A mean value for each site is plotted in the diagrams 3 and 4 (Fig. 21). All spectra but the Varberg charnockite have broad peaks shifted to the left of the zircon characteristic peak at ~1007 cm^{-1}, usually as an effect of radiation damage (Nasdala et al. 1995; Ming et al. 2000). The degree of crystallinity (Nasdala et al. 1995) is presented in Table 7, showing that the spectrum of the reference sample is characteristic for a well crystallized zircon and that the samples from Mien are metamict. The Varberg zircon peaks are narrower and more distinct than the Mien samples (Diagram 4), and show low intensities between the main peaks. The melted part of the porous grain (site P3) recorded relatively few peaks (Diagram 3) and has a steep positive slope due to the lack of crystallinity. Both Mien samples display a peak at ~145cm^{-1} which is indicative of crystalline t-ZrO$_2$. Also, a slight elevation is visible at 261 cm^{-1}, close to the frequency of the t-ZrO$_2$ peak at 259 cm^{-1}. In the sample obtained outside the Mien area, a peak at ~639 cm^{-1} almost coincides with the t-ZrO$_2$ peak at 641 cm^{-1}.
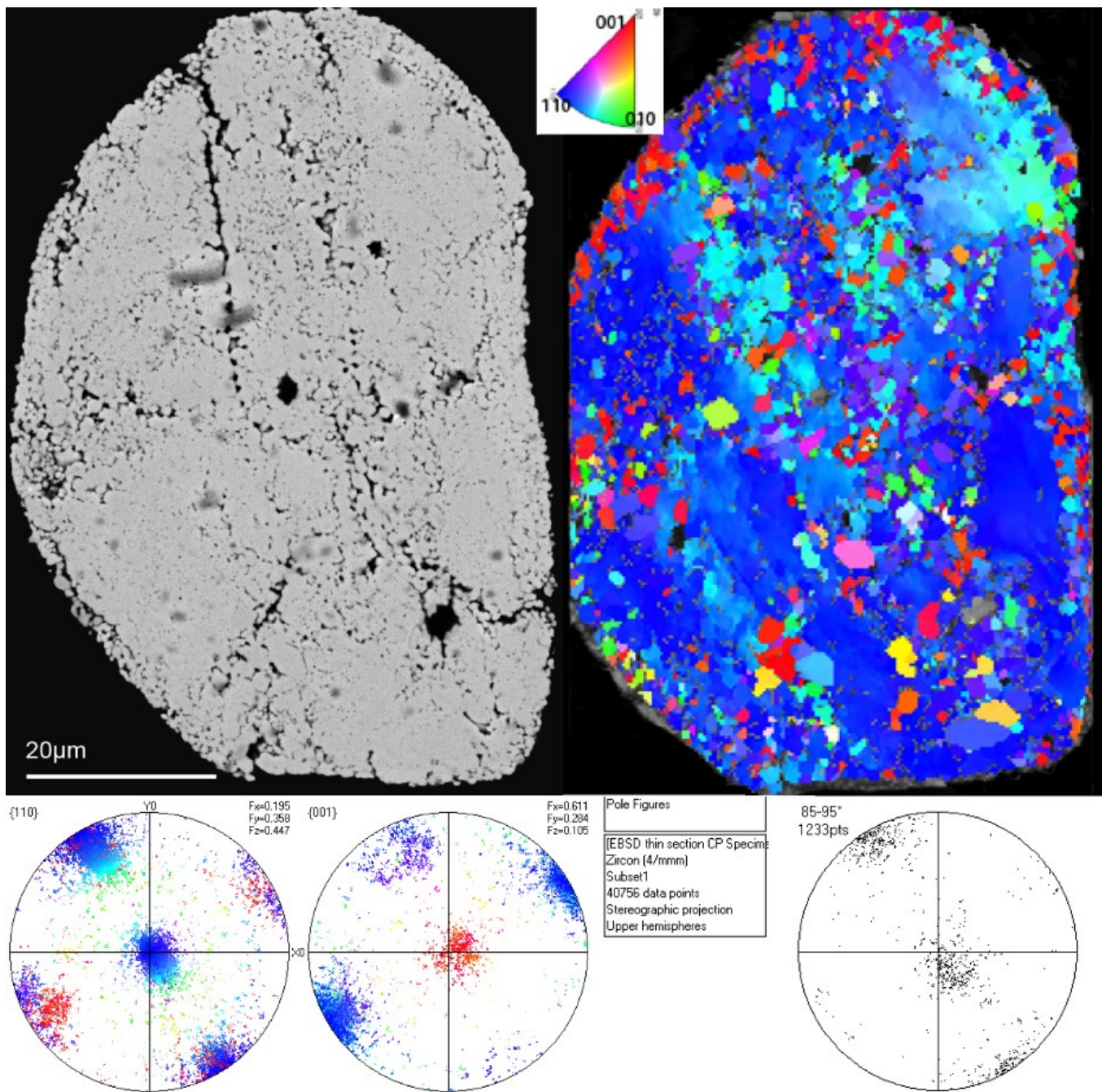
Figure 20. BSE image and corresponding EBSD map of a granular grain from the clast-poor impact melt rock. Pole figures show a perpendicular systematic misorientation between neoblasts with a relationship of 90° between three orientations, and coincidence between (110) and (001). This relationship coincides with former presence of reidite. Misorientation map show that angles between 85°-95° coincide with pole (110). All pole figures are plotted with a stereographic projection in upper hemisphere.
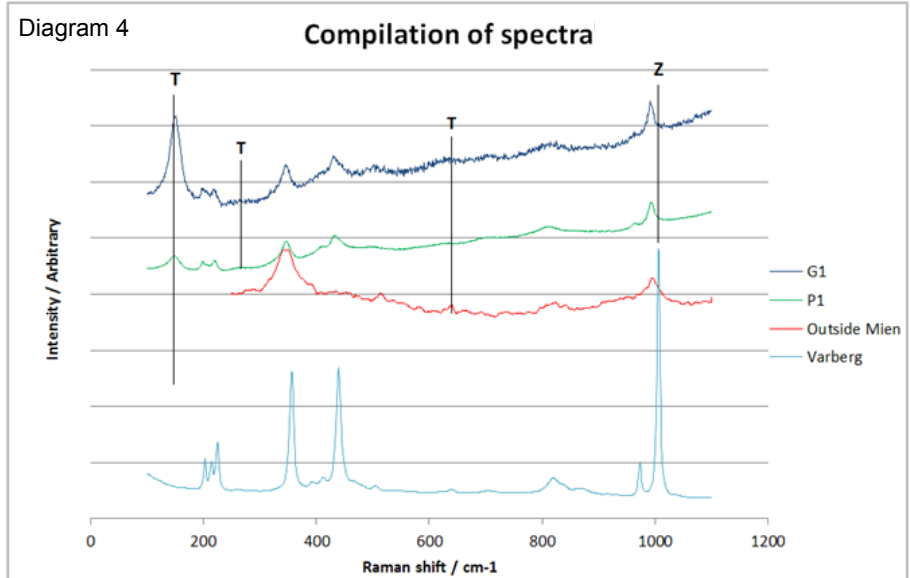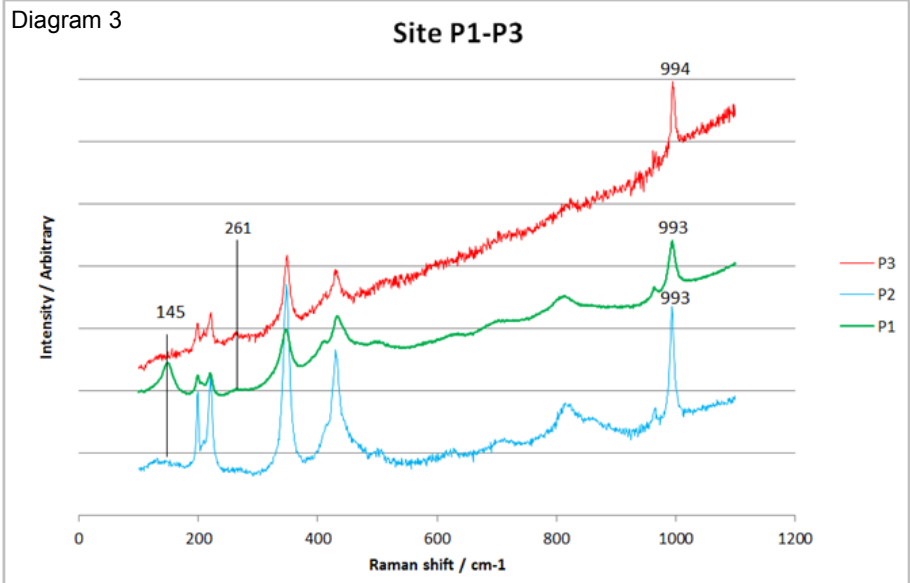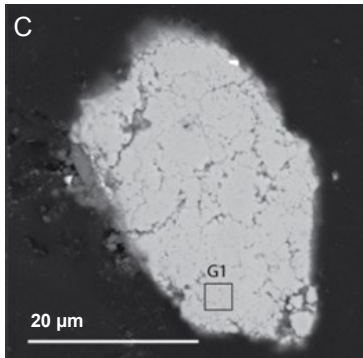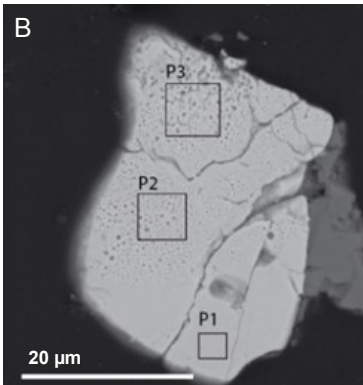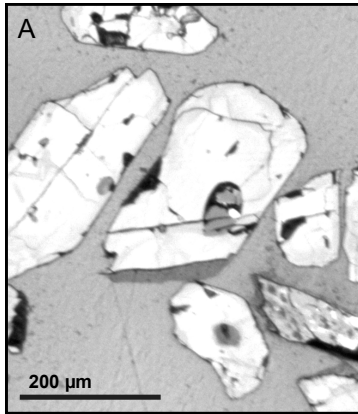
Figure 21. A: Raman image of the Varberg Charnockite. B: BSE image of a partly porous grain from the clast-poor impact melt rock. C: BSE image of a granular grain from the clast-poor impact melt rock. The analyzed sites are marked with boxes.

Diagram 3: Three representative spectra showing sites P1-P3 from the porous Mien zircon. All are shifted to the left of the zircon characteristic peak at ~1007 cm^{-1}. Diagram 4: A comparison between a perfectly crystalline zircon from the Varberg charnockite, a zircon from the area outside Mien impact structure, and two shocked grains: a porous zircon grain (P1) and a granular zircon grain (G1). Z= zircon T= tetragonal ZrO_2.

Table 6. Four grains were analyzed with Raman. Spectra were acquired from the sites described in the table.

	Analyzed sites	
1	Porous Mien zircon P1-P3	Spectra's from three sites were acquired; one seemingly homogenous area without pores (P1), one porous area (P2) and one porous-melted area (P3).
2	Granular Mien zircon G1	A fully granular grain where spectra's from two sites were acquired, both located close to the rim of the grain. Spectra's were nearly identical why only site G1 is shown in the diagram.
3	Granite sample outside crater area	One spectra is shown in diagram 2. The zircon had a halo and was radiation damaged.
4	Varberg Charnockite	All spectra's were acquired from a homogenous area without visible fractures.

33

Table 7. Crystallinity based on the v3 (SiO₄) Raman band (Nasdala et al. 1995) of the different analyzed samples. Half-width was not measured, but it is possible to visually distinguish an increased broadening of peaks compared to Varberg (diagram 2) as the grains become more metamict.

	Structural state band (cm^{-1})	$v3(SiO_4)$
		v
Varberg	very well crystallized	1007
P1	metamict	993
G1	metamict	992
Outside Mien	metamict	993

5. Discussion

5.1. Short summary of results

Textures interpreted to be related to shock have been found in zircon from Mien; and when possible, these have been assigned to known corresponding pressures and temperatures (Timms 2017). The result is both a textural study and the proposal of a P-T diagram for both the two types of impact melt rock and the "suevite" breccia from the Mien impact structure. In the textural study, main focus has been two frequently occurring microfeatures: granular texture and microporous texture. Results from the EBSD analysis on a granular grain showed a perfect match with so-called "former reidite in granular neoblastic zircon" (FRIGN zircon); a fairly newly constrained orientation relationship between granules and to date only described from a few other impact settings. This finding demonstrates former presence of the zircon high-pressure polymorph reidite and can thus be added to the list of high-pressure polymorphs found in Mien. This study also demonstrates that all zircon grains in this study were metamict, a result that have implications on P-T estimations. In many cases, shock textures were only observable on the exterior surface of the grains; this can be of importance when looking for shock signatures in polished sections.

5.2. Microtextures in zircon

5.2.1. Granular texture

Granular texture occurred in grains from all rock types, either as fully granular or partly granular grains. The appearance of the granules differs somewhat between grains and lithologies, and Figure 22 suggest how these may relate to (increasing) shock pressure. In the last stage/picture the granular surface seems melted, probably as an effect of temperature rather than pressure. Granules occurring in fractures (possibly first stage of granulization), are generally larger than granules in fully granulized grains.

Granular or polycrystalline zircon is found in metamorphic settings, and is a product of tectonic shear zones or progressive metamorphism (Söderlund et al. 2008; Beckman et al. 2017) or shock metamorphism (Cavosie et al. 2016; Cavosie et al. 2018). In amphibolite facies metamorphic zircon from Herrestad, the formation of polycrystalline textures in association with baddeleyite was interpreted as progressive breakdown of baddeleyite, resulting in granular textures (Beckman et al. 2017) and the aggregates were interpreted as being the end product between baddeleyite reacting with a silica rich fluid. This means that granular textures similar to the ones observed in Mien zircon do not exclusively form under impact metamorphic conditions. To confirm that granules formed as neoblasts during impact, Mien zircon was obtained from unaffected bedrock outside the crater area and compared to shocked zircon in impact-melt rocks and "suevite" breccia. The absence of granular grains in un-shocked rock, and the occurrence of granular/polycrystalline texture in shocked zircon - sometimes together with ZrO₂ - suggest that the texture is related to the impact event. Further, systematic orientations of granules in one grain indicate a former high-pressure phase only found in impact settings.

In a compilation of case studies on shock metamorphic zircon by Timms et al. (2017) all suggested P-T paths show that granular textures in zircon form late in the P-T history experienced by the grain, and the formation could be either due to the reversion from reidite to zircon by heating above 1200°C (Timms et al. 2017) or where formerly dissociated zircon at 1673°C (Kaiser et al. 2008) is reconstituted through the process of ZrO₂ grains reacting with silica saturated impact melt (Timms et al. 2017).

Formation of planar microstructures and granules may be favoured by radiation damage, which creates zones of weakness within the zircon (Schmieder et al. 2015). If zircon from Mien was al-

ready metamict at the time of impact as suggested by the Raman analysis, this could have increased the possibility of forming impact-triggered granularization. Different degrees of metamictization could possibly be one reason why some grains contain granules and others do not.

5.2.2. Microporous texture

In the impact melt rock samples, porous texture often occurs in confined areas both at the surface and inside the zircon grains, similar to a "unusual vesicular texture" previously described by Singleton et al. (2015). They interpreted the pores as a texture forming just below the melting point of zircon. Porous texture has also been found together with granular texture in zircon from the lunar meteorite Dhofar 458, suggested to be the result of melting and degassing processes (Zhang et al. 2011). Porous texture was not observed in zircon grains obtained from outside the Mien crater area and the formation of the texture would therefore be related to the impact event. Metamorphic zircon with microporous inclusion-rich texture, similar to the texture found in Mien, has been described by Hay & Dempster (2009). In their samples, pores were confined to multiple areas related to growth zones, and were slightly enriched in Fe at the expense of Si and Zr. They suggested that porous areas might be associated with an absence or restricted fluid access. Radiation damage can favour formation of porous texture (as well as granular texture), since irradiation makes zircon 2-3 times more susceptible to dissolution. Presence of hydrothermal fluids is expected in impact-settings, and elevated temperatures generates even higher dissolution rates (Hay & Dempster 2009). In Mien, pores do not always concentrate along growth zones and can occur seemingly randomly. It is likely that fluids were involved in the formation of porous texture in Mien, and that the formation was favoured in weakened shocked zircon grains as opposed to the un-shocked (but still metamict) grains outside the structure.

Zircon grains from the clast-poor impact melt rock have a feature best described as trails of pores, similar to the "suspicious trails of bubbles" and "bands of pores" from the Popigai Crater and the Chixulub Crater reported by Wittmann et al. (2006), a feature that they interpreted as remnants of decorated PDFs. These pore trails would therefore have a different formation mechanism than the porous zircon previously described. The pore trails in Mien zircon most likely originate from PDFs, meaning that these grains would have experienced shock conditions of at least ~40 GPa

(Leroux et al. 1999).

5.3. Ballen quartz

Quartz with ballen texture was found in thin sections from the Mien impact melt rocks, and ballen textured quartz in impactites from Mien have previously been studied in greater detail by Ferrière et al. (2009). The texture form as amoeboid clusters with egg-formed "bubbles" or spheroids intersecting each other, and are similar in form to lechatelierite inclusions found in some impact glasses from Mien (Carstens 1975). Ballen quartz occurs exclusively within diaplectic quartz glass and lechatelierite (Ferrière et al. 2009), two high pressure phases that requires pressures of ~35 GPa and ~50 GPa respectively (Stöffler & Langenhorst 1994). Annealing experiments have shown that formation of ballen quartz (or quartz with ballen-like features) requires temperatures of >1200°C (Short
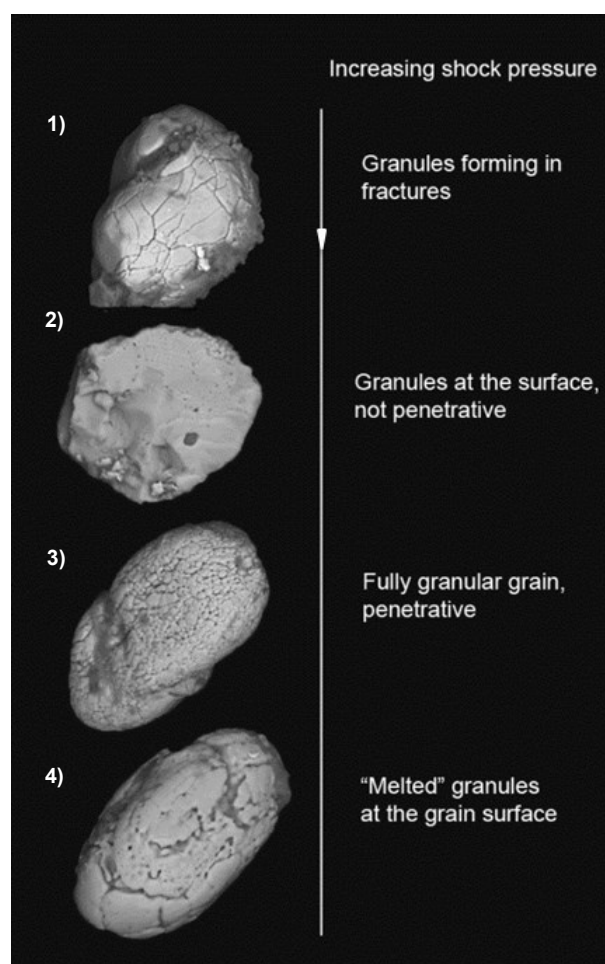

Figure 22. Four stages of microtextures possibly relating to increasing shock pressure; 1) a fractured grain with small granules in between fractures. 2-3) are grains granulized to different degrees, and in 4) the surface texture (and granules) also seem to have been affected by high temperatures.

1970). Ballen quartz is the result of back-transformation and exists in different variants, meaning it should not be used as the only shock pressure indicator in a sample. However, as a complement to other findings in this study it does contribute to constraining P/T conditions since the pressure must have exceeded ~35 GPa for the formation of diaplectic glass.

5.4. Reidite formation (FRGN zircon)

Natural reidite has only been found at a few localities (Wittmann et al. 2006), for example in distal ejecta from the Eocene Chesapeake bay impact (Glass & Liu 2001), in a suevite melt fragment from the Ries crater (Timms et al. 2017), and in shocked zircon from the Stac Fada Member in northwestern Scotland (Reddy et al. 2015). Two types of reidite are most commonly reported: lamellar reidite and granular reidite. The formation process of these two types is dependent on the degree of radiation damage; in pre-metamict zircon the transformation to reidite may be inhibited since the martensitic transformation process requires a pre-existing zircon lattice (Kusaba et al. 1985). Lamellar reidite on the other hand, seem restricted to non-metamict domains in zircon where it preferentially forms in the crystalline rim (Cavosie et al. 2015; Reddy S.M. et al. 2015; Timms et al. 2017). No reidite was found in Mien zircon, and since lamellae propagation would be restrained by lattice defects (Timms 2017), absence of lamellar reidite is expected. However, granular reidite forms preferentially in a partially metamict core since these domains are more elastically compliant, and thus function as nucleation sites (Timms et al. 2017).

Reversion from reidite to zircon – so called FRGN zircon (Cavosie et al. 2018) - can occur via symmetrically equivalent relationships that results in zircon neoblasts that inherits the crystallographic orientation of the reidite phase. The EBSD analysis of granular Mien zircon show this type of relationship and indirectly confirms reidite, since granules with systematic ~90° misorientation - meaning that <110> of the neoblasts is aligned with [001] of the host grain – is unanimous with the presence of FRGN zircon (Fig. 20; Cavosie et al. 2016; Cavosie et al. 2018). Since reidite formation preceded the growth of zircon neoblasts, the latter most likely formed during a decompression stage when the grain returned to the zircon stability field. The implication is that the systematic orthogonal disorientation relationship (~ 90° around <110>) between the neoblasts can be used as an indicator of the reversion from reidite to zircon. EBSD analysis was performed on one single zircon grain from Mien, which showed systematically ordered granules. If granules in other grains are oriented randomly, they could have formed as a solid state transformation from ZrO_2 phases, zircon or reidite but with following physical rotation within the silicate melt (Timms et al. 2017). However, even if the granules would not be the result of back-transformation from reidite, they crystallized late in the P-T history of the impact melt after the stabilization of zircon below 1673°C.

The transformation to reidite could have been affected if zircon from Mien was metamict before the impact, causing a problem when determining peak pressure- and temperature based on the occurrence of the polymorph. Lang et al. (2008) simulated radiation damage in zircon, and observed that the transformation to reidite happened at much higher static pressure (~36 GPa) in ion beam irradiated zircon than in non-irradiated zircon. The expanded stability field is a result of the interplay between pressure, the formation of nanoscale damage domains, and ion beam induced amorphization. Compressibility can also be affected by zircon composition and presence of trace elements (Van Westrenen et al. 2004). In pure zircon the transformation from zircon to reidite starts at pressures around 19.7 GPa, and the transformation takes place more easily and at a lower pressure than in impure natural zircon (Van Westrenen et al. 2004). Elevated levels of Hafnium (Hf), a zircon isostructural and common trace element (Speer & Cooper 1982), were detected in porous Mien zircon. Zircon will easier get metamict if Hf is present in the grain, and particularly Hf-rich zones tend to contain more compositional substitutions for Zr and Si (Speer & Cooper 1982). As for Mien, these two considerations could imply that the transformation to reidite took place at a higher pressure than would otherwise be expected.

Besides EBSD, Raman analysis was conducted with the aim of pinpointing reidite (Fig. 21). Knittle & Williams (1993) experimentally attributed specific Raman frequency peaks to reidite (scheelite-structured zircon). Several authors have used these peaks to identify reidite (Gucsik 2007; Chen et al. 2013). In site P1 of the Mien zircon, a minor peak at 408 cm^{-1} corresponds to reidite. However, all Raman spectra's of the shocked zircon grains displayed frequency shifts of the 1007 cm^{-1} band, making it impossible to use the spectra to identify reidite. Frequency shifts can be explained by e.g. the degree of radiation damage (Nasdala et al. 1995), occurrence of impurities (Speer & Cooper 1982), strain from the shockwaves or high-

pressure induced deformation (Gucsik 2007). The degree of metamictization can be estimated from a (theoretical) well crystallized zircon, where the half-width of the antisymmetric stretching vibration band (B_{Ig} of the SiO_4 tetrahedra) has a frequency of ~1007 cm^{-1} (Nasdala et al. 1995)(Table 7). The reference sample in this study, The Varberg charnockite, is categorized as very well crystallized, with a major peak at 1007 cm^{-1}. Zircon grains within and outside the Mien impact structure have almost identical values skewed to the left of the main zircon peak (Table 7). Raman data confirm that Mien zircon are metamict and approximately to what degree, but this fact also inhibit the possibility to use Raman analysis as a method of identifying reidite.

5.5. Inclusions of ZrO_2

Several zircon grains from the clast-poor impact melt thin section have ZrO_2 inclusions inside the zircon neoblasts, similar to zircon grains from the Acraman melt rock (Schmieder et al. 2015) and from the Chixulub crater (Wittmann et al. 2006). Baddeleyite is expected in silica poor mafic and ultramafic rocks, but since the Mien impact melt rock derives from a granite (silica-saturated) host rock, the detection of ZrO_2 within granular zircon in these samples strongly implies that baddeleyite formation is impact-induced. If the growth of the zircon granules started after dissociation, consumption of ZrO_2 and sourcing of SiO_2 from the surrounding impact-melt could explain formation of baddeleyite (Schmieder et al. 2015; Timms et al. 2017). This means that the grain must have experienced post-decompression temperatures of at least 1690°C. Schmieder et al. (2015) assign ZrO_2-bearing granular zircon shock pressures in excess of 65-70 GPa. No crystallographic analysis has been made on Mien zircon with ZrO_2 inclusions so whether they are oriented systematically (as FRGN zircon) or not is unknown.

5.6. P-T constraints

One interesting implication of the shock textures registered in this study is that they collectively enable the construction of a P-T trajectory for the shocked zircon and possibly the impactite (Fig. 23 & 24). I have used the framework for "extreme thermobarometry" on zircon by Timms et al. (2017), which is based on two different approaches of either "direct evidence", or former presence of phases, by them referred to as "phase heritage". Examples of direct evidence can be preserved high-pressure phases such as reidite, diag-

nostic shock microstructures such as PDFs or twins in zircon or dissociation of zircon to ZrO_2 and SiO_2. The identification of FRGN zircon is an example of phase heritage, and the reversion from reidite indicates a pressure of ≥30 GPa for shock metamorphism (Timms et al. 2017 and references therein) Another example is zircon dissociation that may reveal former presence of cubic zirconia or tetragonal zirconia which yields temperature constraints of ≥2370 °C and ≥~1673 °C respectively.

The suggested P-T path (Fig. 24) for impact melt zircon in Mien is based on the P-T path for the Acraman zircon grains, that seem similar to this study (Schmieder et al. 2015; Timms et al. 2017). Both the Acraman zircon and the Mien zircon samples include granular grains, sometimes with ZrO_2-inclusions and FRGN zircon. The dissociation of zircon indicates high post-shock decompressions temperatures. Post-shock temperatures as high as 1500°C in non-porous quartzo-feldspathic rocks have previously been correlated with shock pressures of 60 GPa (Stöffler 1971). With this motivation, Timms et al. (2017) draws the conclusion that the Acraman zircon experienced shock pressures of at least 60 GPa, and that the melt rock was very close to "ground zero". As discussed earlier, the Mien zircon might have been metamict at the time of impact, which could have made them weaker to extreme shock conditions. A possible change in the phase stability field at high pressure caused by pre-metamictization (Lang et al. 2008) is therefore an important observation. Radiation damage can result in a unexpectedly low reidite content (Lang et al. 2008), so if disregarding temperature i.e. if it has no major influence on the reidite formation process, the usage of reidite as a peak-pressure indicator may actually give an estimation of the lower boundary of the pressure event (Lang et al. 2008). EBSD analysis was only conducted on one grain from Mien, so it is possible that other granular grains formed via other processes than the FRGN zircon, meaning that what state the zircon grains were in above 30 GPa remains unknown (high pressure polymorph or constituent oxides). This makes pressure estimates of these grains more speculative. However, the findings presented in this study indicate similar conditions for the Acraman zircon and the Mien impact melt rocks.

The "suevite" breccia displayed shock features corresponding to lower shock conditions than the impact melt rocks. Since melt fragments may derive from different locations in the transient crater (see explanation in background chapter), a P-T path for the breccia is not possible to establish. The diagram in

Figure 24 is based on granular grains and the rare occurrence of PDF-like features in zircon.

The exact shape of a suggested P-T trajectory is dependent on several unknown factors. The size, velocity and composition of the impactor would all have an impact on the shock metamorphic response of minerals and peak P-T experienced by the rocks. The position of the target rock itself relative to the impact site and the material properties of the target rock could also modify the shape of the P-T path. In Mien, the target rock was crystalline, but whether it was overlaid by a (now eroded) sedimentary layer has not been established. Also, the actual properties of the meteorite are unknown, though Earth Impact Database suggests a stone type meteorite.

5.7. Difference between impactites

Abundance and size of granular- and microporous textures in both impact melt rocks, and detection of FRGN zircon in the clast-poor impact melt rock, indicates that these rocks have experienced higher shock pressures than the "suevite" breccia. The higher abundance of penetrating granular textures in the clast-poor impact melt rocks could possibly be an indication that these have been subjected to higher shock pressures than the clast-rich. This is in accordance with the general stratigraphy of impactites (from bottom upwards): "suevite" breccia → clast rich impact melt rock → clast poor impact melt rock (Osinski & Grieve 2017). The exact location of the "suevite" breccia sample in relation to the center of the crater has not been established (e.g. outer suevite, crater suevite or dike

suevite). In stratigraphy descriptions from Mien, the "suevite"-layer occur underneath impact melt; however, the loose rock sample used in this study may not necessarily derive from this layer.

6. Conclusions

- Different types of shock related microfeatures in zircon are present from Mien, notably on granular texture and microporous texture. Some granular grains had inclusions of ZrO_2 inside neoblasts. This indicates dissociation of zircon at temperatures of ~1673°C.

- Shock textures in zircon reveal that the impact melt rocks have experienced higher shock than the "suevite" breccia. Granular texture occurred frequently in the impact melt rocks, but was generally absent, or present in small amounts, in the "suevite" breccia. Porous texture occurred in all impactites and might be connected to alteration processes rather than shock pressure or shock temperature.

- Detection of "Former Reidite in Granular Neoblasts", so called "FRIGN zircon" indicate that reidite was present during the impact, but later reverted to zircon. FRGN zircon has previously only been described from a handful of locations. The discovery of FRGN zircon in Mien is therefore important, not only because reveals details on the Mien impact, but it also complements current knowledge on zircon behaviour at shock conditions.
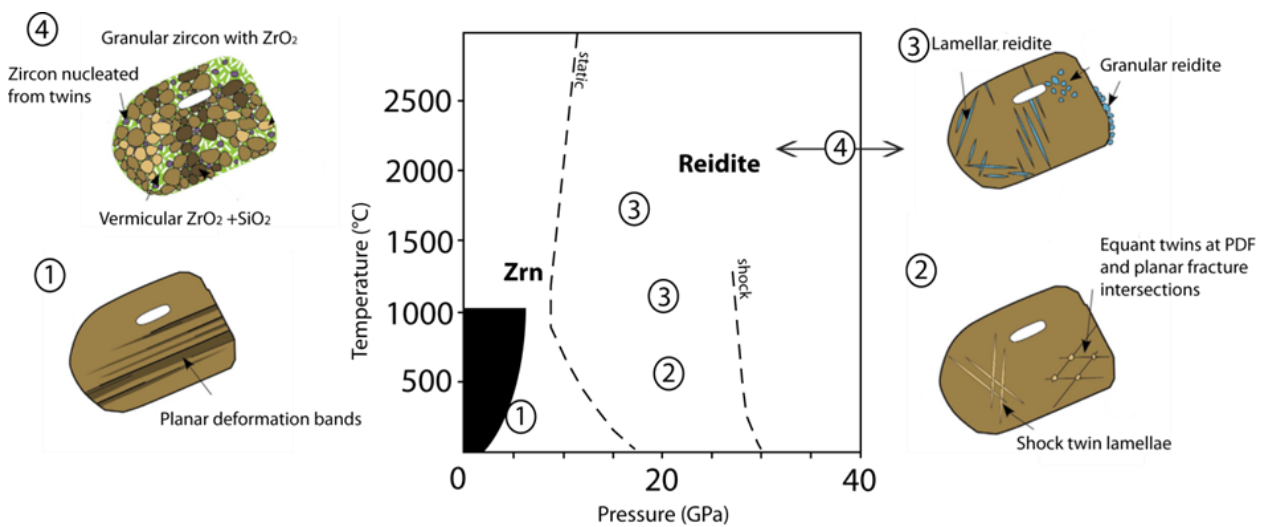
Figure 23. P-T-diagram of shock behaviour in zircon (Modified from Timms et al 2017)
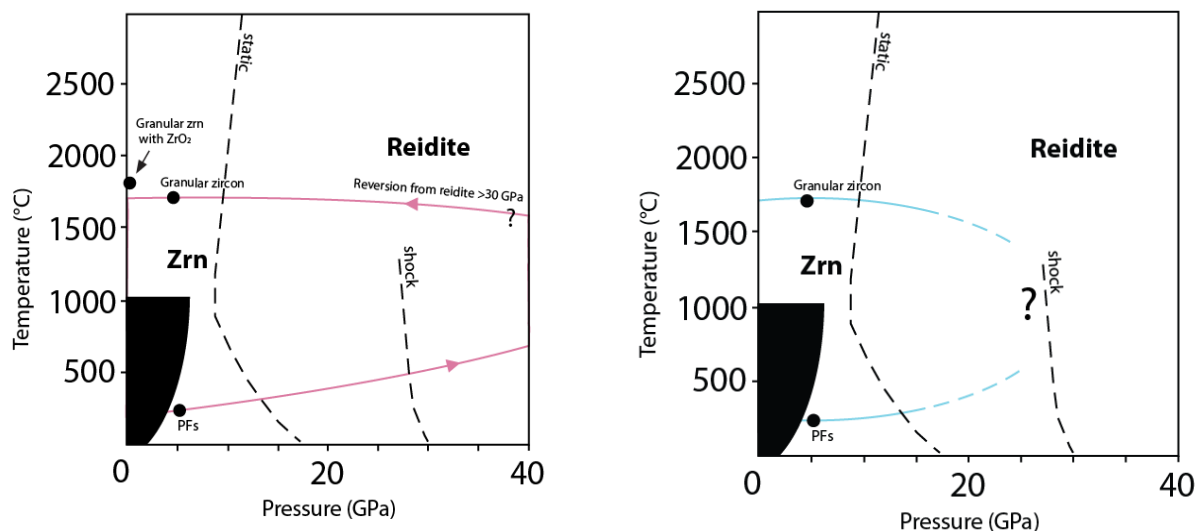
Figure 24. Suggested P-T paths for Mien zircon from impact melt rocks and "suevite" breccia based on P-T phase diagrams by Timms et al. 2017. The "suevite" breccia contains zircon that have been subjected to lower shock conditions than the impact-melt rocks and is based on the rare occurrence of granular zircon and planar fractures (PFs; possibly planar deformation features) in zircon.

- Raman analysis showed that all zircon grains in this study have accumulated radiation damage. This may have implications for determination of peak pressure and temperature.

- Altogether, the findings in this study have resulted in a P-T phase diagram for the Mien zircon, indicating temperatures >1500°C and pressures in excess of 60 GPa for zircon in impact melt rocks.

- Zircon is the only known terrestrial mineral that can record both temperature- and pressure at extreme conditions. Shock textures in zircon have been reported from terrestrial impact structures but also in extra-terrestrial materials such as in meteorites. Understanding how these specific textures relate to shock conditions can give valuable insights on the formation and evolution of impact craters on Earth and other planets in our solar system.

7. Future research

A suggestion for future research on Mien would be to explore the lateral distribution of shock textures, especially any occurrence of FRIGN zircon. The impactites used in this study were collected as loose rocks, and a study on drill-core material could be beneficial for further constraining of P-T conditions.

8. Acknowledgements

9. References

Earth Impact Database. Accessed 20180504, from http://www.passc.net/EarthImpactDatabase/mien.html.

2013a: Russian meteorite crash: LIVE UPDATES. *RT*.

2013b: Meteorites slam into Russia as meteor seen streaking through morning sky. CBS/AP.

Alvarez, L. W., Alvarez, W., Asaro, F. & Michel, H. V., 1980: *Extraterrestrial Cause for the Cretaceous-Tertiary Extinction*. 1095-1108 sid.

Åström, K., 1998: Seismic signature of the Lake Mien impact structure, southern Sweden: *Geophysical Journal International 135*, 215-231. doi: 10.1046/j.1365-246X.1998.00628.x

Beckman, V., Möller, C., Söderlund, U. & Andersson, J., 2017: Zircon Growth during Progressive Recrystallization of Gabbro to Garnet Amphibolite, Eastern Segment, Sveconorwegian Orogen: *Journal of Petrology 58*, 167-187. doi: 10.1093/petrology/egx009

Bottomley, R. J., York, D. & Grieve, R. a. F., 1978: 40Ar39 Ages of Scandinavian Impact Structures: I Mien and Siljan: *Contrib Mineral Petrol 68*, 79-84. doi: 0010,7999/78/0068/0079/

Bottomley, R. J., York, D. & Grieve, R. a. F., 1990: Argon-40-argon-39 dating of impact craters. *Lunar and Planetary Science Conference, 20th*. Houston. 421-431 s.

Brumfiel, G., 2013: Russian meteor largest in a century. *Nature News*. Springer Nature.

Carstens, H., 1975: Thermal history of impact melt rocks in the Fennoscandian shield: *Contributions to Mineralogy and Petrology 50*, 145-155. doi: 10.1007/bf00373334

Cavosie, A. J., Erickson, T. M. & Timms, N. E., 2015: Nanoscale records of ancient shock deformation: Reidite (ZrSiO4) in sandstone at the Ordovician Rock Elm impact crater: *Geology 43*, 315-318. doi: 10.1130/g36489.1

Cavosie, A. J., Timms, N. E., Erickson, T. M., Hagerty, J. J. & Hörz, F., 2016: Transformations to granular zircon revealed: Twinning, reidite, and ZrO2 in shocked zircon from Meteor Crater (Arizona, USA): *Geology 44*, 703-706. doi: 10.1130/G38043.1

Cavosie, A. J., Timms, N. E., Ferrière, L. & Rochette, P., 2018: Former Reidite in Granular Neoblastic Zircon (FRIGN Zircon) from the Luizi Impact Structure and Proposed Pantasma Structure. *49th Lunar and Planetary Science Conference*. Houston.

Chen, M., Yin, F., Li, X., Xie, X., Xiao, W. & Tan, D., 2013: Natural occurrence of reidite in the Xiuyan Crater of China: *Meteoritics & Planetary Science 48*, 796-805. doi: 10.1111/maps.12106

Dempster, T. & Chung, P., 2013: Metamorphic zircon: tracking fluid pathways and the implications for the preservation of detrital zircon. *Journal of the Geological Society 170*, 631-639. doi: 10.1144/jgs2012-063

Dence, M. R., 1971: Impact melts: *Journal of Geophysical Research 76*, 5552-5565. doi: 10.1029/JB076i023p05552

Dence, M. R., 1972: The nature and significance of terrestrial impact structures: *24th Int. Geol. Congr., Montreal*, 77-89.

Dressler, B. O. & Reimold, W. U., 2001: Terrestrial impact melt rocks and glasses: *Earth-Science Reviews 56*, 205-284. doi: https://doi.org/10.1016/S0012-8252(01)00064-2

Erickson, T. M., Cavosie, A. J., Moser, D. E., Barker, I. R. & Radovan, H. A., 2012: Correlating planar microstructures in shocked zircon from the Vredefort Dome at multiple scales: Crystallographic modeling, external and internal imaging, and EBSD structural analysis: *American Mineralogist 98*, 53-65. doi: 10.2138/am.2013.4165

Erickson, T. M., Pearce, M. A., Reddy, S. M., Timms, N. E., Cavosie, A. J., Bourdet, J., Rickard, W. D. A. & Nemchin, A. A., 2017: Microstructural constraints on the mechanisms of the transformation to reidite in naturally shocked zircon: *Contributions to Mineralogy and Petrology 172*, 6. doi: 10.1007/s00410-016-1322-0

Fassett, C. I., Head, J. W., Blewett, D. T., Chapman, C. R., Dickson, J. L., Murchie, S. L., Solomon, S. C. & Watters, T. R., 2009: Caloris impact basin: Exterior geomorphology, stratigraphy, morphometry, radial sculpture, and smooth plains deposits: *Earth and Planetary Science Letters 285*, 297-308. doi: https://doi.org/10.1016/j.epsl.2009.05.022

Ferrière, L., A Koeberl, C., C Libowitzky, E., Reimold, W., D Greshake, A. & B Brandstätter, F., 2010: *Ballen quartz and cristobalite in impactites: New investigations*. The geological Society of America.

Ferrière, L., Koeberl, C. & Reimold, W. U., 2009: Characterisation of ballen quartz and cristobalite in impact breccias: new observations and constraints on ballen formation: *European Journal of Mineralogy 21*, 203-217. doi: 10.1127/0935-1221/2009/0021-1898

Finch, R. J. & Hanchar, J. M., 2003: Structure and Chemistry of Zircon and Zircon-Group Minerals: *Reviews in Mineralogy and Geochemistry 53*, 1-25.

French, B. M., 1998: *Traces of Catastrophe: A Handbook of shock-Metamorphic Effects in Terrestrial Meteorite Impact Structures*. Lunar and Planetary Institute, Houston. 120 sid.

Frey, H., 1980: Crustal evolution of the early earth: The role of major impacts: *Precambrian Research 10*, 195-216. doi: https://doi.org/10.1016/0301-9268(80)90012-1

Glass, B. P. & Liu, S., 2001: Discovery of high-pressure ZrSiO4 polymorph in naturally occurring shock-metamorphosed zircons: *Geology 29*, 371-373. doi: 10.1130/0091-7613 (2001)029<0371:DOHPZP>2.0.CO;2

Glikson, A. Y., 2001: The astronomical connection of terrestrial evolution: crustal effects of post-3.8 Ga mega-impact clusters and evidence for major 3.2±0.1 Ga bombardment of the Earth–Moon system: *Journal of Geodynamics 32*, 205-229. doi: https://doi.org/10.1016/S0264-3707(01)00029-1

Goltrant, O., Cordier, P. & Doukhan, J.-C., 1991: Planar deformation features in shocked quartz; a transmission electron microscopy investigation: *Earth and Planetary Science Letters 106*, 103-115. doi: http://dx.doi.org/10.1016/0012-821X(91)90066-Q

Goltrant, O., Leroux, H., Doukhan, J.-C. & Cordier, P., 1992: Formation mechanisms of planar deformation features in naturally shocked quartz: *Physics of the Earth and Planetary Interiors 74*, 219-240. doi: http://dx.doi.org/10.1016/0031-9201(92)90012-K

Goodwin, A. M., 2016: *Precambrian Geology: The Dynamic Evolution of the Continental Crust*. Elsevier Science.

Grieve, R. a. F., 1991: Terrestrial impact: The record in the rocks*: *Contribution of the Geological Survey of Canada 26*, 175-194. doi: 10.1111/j.1945-5100.1991.tb01038.x

Gucsik, A., 2007: Micro-Raman spectroscopy of reidite as an impact-induced high pressure polymorph of zircon: experimental investigation and attempt to application: *47*.

Hanchar, J. M. & Miller, C. F., 1993: Zircon zonation patterns as revealed by cathodoluminescence and backscattered electron images: Implications for interpretation of complex crustal histories: *Chemical Geology 110*, 1-13. doi: 10.1016/0009-2541(93)90244-D

Hay, D. C. & Dempster, T., 2009: *Zircon Behaviour during Low-temperature Metamorphism*.

Henkel, H., 1982. The lake Mien structure. Geophysical department Report, Geological Survey of Sweden, 82-21 sid.

Henkel, H., 1992: Geophysical aspects of meteorite impact craters in eroded shield environment, with special emphasis on electric resistivity: *Tectonophysics 216*, 63-89. doi: https://doi.org/10.1016/0040-1951(92)90156-Z

Holst, N. O., 1890: Ryoliten vid sjön Mien (In Swedish). Stockholm, Sveriges Geologiska Undersökning, Serie C, Avhandlingar och Uppsatser. 50 s.

Hoskin, P. W. O. & Schaltegger, U., 2003: The Composition of Zircon and Igneous and Metamorphic Petrogenesis: *Reviews in Mineralogy and Geochemistry 53*, 27-62. doi: 10.2113/0530027

Kaiser, A., Lobert, M. & Telle, R., 2008: Thermal stability of zircon (ZrSiO4): *Journal of the European Ceramic Society 28*, 2199-2211. doi: https://doi.org/10.1016/j.jeurceramsoc.2007.12.040

Kamo, S. L., Lana, C. & Morgan, J. V., 2011: U–Pb ages of shocked zircon grains link distal K–Pg boundary sites in Spain and Italy with the Chicxulub impact: *Earth and Planetary Science Letters 310*, 401-408. doi: 10.1016/j.epsl.2011.08.031

Kamo, S. L., Reimold, W. U., Krogh, T. E. & Colliston, W. P., 1996: A 2.023 Ga age for the Vredefort impact event and a first report of shock metamorphosed zircons in pseudotachylitic breccias and Granophyre: *Earth and Planetary Science Letters*, 369-387.

Kerr, G., W Young, R., Cullings, H. & F Christy, R. 2005: Bomb parameters. *I* R. W. Young & G. D. Kerr (red.): *Reassessment of the atomic bomb radiation dosimetry for Hiroshima and Nagasaki Dosimetry system 2002 DS02 Volume 2*, 42-61, INIS.

Kieffer, S. W. & Simonds, C. H., 1980: The role of volatiles and lithology in the impact cratering process: *Reviews of Geophysics 18*, 143-181. doi: 10.1029/RG018i001p00143

Knittle, E. & Williams, Q., 1993: High-pressure Raman spectroscopy of ZrSiOoz Observation of the zircon to scheelite transition at 300 K: *American Mineralogist 78*, 245-252.

Krogh, T. E., 1984: Precise U-Pb zircon and baddeleyite ages for the Sudbury area.

Kusaba, K., Syono, Y., Kikuchi, M. & Fukuoka, K., 1985: Shock behavior of zircon; phase transition to scheelite structure and decomposition: *Earth and Planetary Science Letters 72*, 433-439.

Lang, M., Zhang, F., Lian, J., Trautmann, C., Neumann, R. & Ewing, R. C., 2008: Irradiation-induced stabilization of zircon (ZrSiO4) at high pressure: *Earth & Planetary Science Letters 269*, 291-295. doi: 10.1016/j.epsl.2008.02.027

Leroux, H., Reimold, W. U., Koeberl, C., Hornemann, U. & Doukhan, J. C., 1999: Experimental shock deformation in zircon: a transmission electron microscopic study: *Earth and Planetary Science Letters 169*, 291-301.

Marcus, R., Melosh, H. J. & Collins, G., 2010: Earth Impact Effects Program. Hämtad 23/4-2018

Martell, J., 2016: A study of shock-metamorphic features in zircon from the Siljan impact structure, Sweden: *Dissertations in Geology at Lund University*.

Melosh, H. J., 1989: *Impact cratering : a geologic process*. New York : Oxford University Press, 1989.

Ming, Z., Ekhard, K. H. S., Ian, F., Ann, G.-B., Philippe, D., Rodney, C. E., Andrew, M. C. & Hugues, L., 2000: Metamictization of zircon: Raman spectroscopic study: *Journal of Physics: Condensed Matter 12*, 1915.

Nasdala, L., Irmer, G. & Wolf, D., 1995: The degree of metamictization in zircon: a Raman spectroscopic study: *European Journal of Mineralogy 7*, 471-478.

Nemchin, A., Timms, N., Pidgeon, R., Geisler, T., Reddy, S. & Meyer, C., 2009: Timing of crystallization of the lunar magma ocean con-

strained by the oldest zircon: *Nature Geoscience 2*, 133-136. doi: 10.1038/ngeo417

Norman, M. D. & Nemchin, A. A., 2014: A 4.2 billion year old impact basin on the Moon: U–Pb dating of zirconolite and apatite in lunar melt rock 67955: *Earth and Planetary Science Letters 388*, 387-398. doi: https://doi.org/10.1016/j.epsl.2013.11.040

Osinski, G. R. & Grieve, R. a. F., 2017: "Suevites" of the West Clearwater Lake Impact Structure, Canada: A demonstration of the need for a revised classification scheme for impactites. *Lunar and Planetary Science XLVIII.*

Osinski, G. R. & Pierazzo, E., 2012: *Impact Cratering: Processes and Products*. John Wiley & Sons, Ltd**.** 309 sid.

Pidgeon, R. T., Nemchin, A. A. & Kamo, S. L., 2011: Comparison of structures in zircons from lunar and terrestrial impactites: *Canadian Journal of Earth Sciences 48*, 107-116.

Reddy S.M., Johnson T.E., Fischer S., Rickard W.D.A. & R.J.M., T., 2015: Precambrian reidite discovered in shocked zircon from the Stac Fada impactite, Scotland: *Geology 43*, 899-902. doi: 10.1130/G37066.1

Renne, P. R., Deino, A. L., Hilgen, F. J., Kuiper, K. F., Mark, D. F., Mitchell, W. S., Morgan, L. E., Mundil, R. & Smit, J., 2013: Time Scales of Critical Events Around the Cretaceous-Paleogene Boundary: *Science 339*, 684.

Schmieder, M., Tohver, E., Jourdan, F., Denyszyn, S. W. & Haines, P. W., 2015: Zircons from the Acraman impact melt rock (South Australia): Shock metamorphism, U–Pb and 40Ar/39Ar systematics, and implications for the isotopic dating of impact events: *Geochimica et Cosmochimica Acta*.

Short, N. M., 1970: Progressive shock metamorphism of quartzite ejecta from the Sedan nuclear explosion crater: *The Journal of Geology 78*, 705-723. doi: 10.1086/627572

Singleton, A. C., Osinski, G. R. & Shieh, S. R., 2015: Microscopic effects of shock metamorphism in zircons from the Haughton impact structure, Canada: *Geol. Soc.Am. Spec. Pap 518*, 135-148.

Söderlund, U., Hellström, F. A. & Kamo, S. L., 2008: Geochronology of high-pressure mafic granulite dykes in SW Sweden: tracking the P–T–t path of metamorphism using Hf isotopes in zircon and baddeleyite: *Journal of Metamorphic Geology 26*, 539-560. doi: 10.1111/j.1525-1314.2008.00776.x

Söderlund, U. & Johansson, L., 2002: A simple way to extract baddeleyite (ZrO2): *Geochem. Geophys. Geosyst. 3*, 7. doi: 10.1029/2001GC000212

Speer, J. A. & Cooper, B. J., 1982: Crystal structure of synthetic hafnon, HfSiO 4 , comparison with zircon and the actinide orthosilicates: *American Mineralogist 67*, 804-808.

Spudis P. D., Dayl, M. J. P. & Kramer, G., 2013: Geology and composition of the Orientale Basin impact melt sheet: *Journal of Geophysical Research: Planets 119*, 19-29. doi: 10.1002/2013JE004521

Stanfors, R., 1969: Lake Mien — An Astrobleme or a Volcano-Tectonic Structure: *Geologiska Föreningen i Stockholm Förhandlingar 91*, 73-86. doi: 10.1080/11035896909448425

Stanfors, R. 1973. *The Mien structure - a cryptoexplosive formation in the Fennoscandian basement.* Lunds Universitet.

Stöffler, D., 1971: Progressive metamorphism and classification of shocked and brecciated crystalline rocks at impact craters: *Journal of Geophysical Research 76*, 5541-5551. doi: doi:10.1029/JB076i023p05541

Stöffler, D., 1972: Deformation and transformation of rock-forming minerals by natural and experimental shock processes: I. Behaviour of minerals under shock-compression.: *Fortschritte der Mineralogie 49*, 50-113.

Stöffler, D., Artemieva, N. A., Wünnemann, K., Reimold, W. U., Jacob, J., Hansen, B. K. & Summerson, I. a. T., 2013: Ries crater and suevite revisited—Observations and modeling Part I: Observations: *Meteoritics & Planetary Science 48*, 515-589. doi: 10.1111/maps.12086

Stöffler, D. & Grieve, R. a. F. 2007: Towards a unified nomenclature of metamorphic petrology: Impactites. *I* D. Fettes & J. Desmons (red.): *Metamorphic Rocks: A Classification and Glossary of Terms, Recommendations of the International Union of Geological Sciences*. Cambridge University Press, Cambridge.

Stöffler, D. & Langenhorst, F., 1994: Shock metamorphism of quartz in nature and experiment: I. Basic observation and theory*: *Meteoritics 29*, 155-181. doi: 10.1111/j.1945-5100.1994.tb00670.x

Svensson, N.-B., 1969: Lake Mien, Southern Sweden — A Possible Astrobleme: *Geologiska Föreningen i Stockholm Förhandlingar 91*, 101-110. doi: 10.1080/11035896909448427

Svensson, N. B. & Wickman, F. E., 1965: Coesite from Lake Mien, Southern Sweden: *Nature 205*, 1202-1203.

Timms, N. E., Erickson, T. M., Pearce, M. A., Cavosie, A. J., Schmieder, M., Tohver, E., Reddy, S. M., Zanetti, M. R., Nemchin, A. A. & Wittmann, A., 2017: A pressure-temperature phase diagram for zircon at extreme conditions: *Earth-Science Reviews 165*, 185-202. doi: https://doi.org/10.1016/j.earscirev.2016.12.008

Timms, N. E., Healy, D. , Erickson, T. M., Nemchin, A. A., Pearce, M. A. And Cavosie, A. J 2017:

Role of Elastic Anisotropy in the Development of Deformation Microstructures in Zircon. *I* F. C. D. E. Moser, J. R. Darling, S. M. Reddy and K. Tait (red.): *Microstructural Geochronology*,

Van Westrenen, W., Frank, M. R., Hanchar, J. M., Yingwei, F., Finch, R. J. & Chang-Sheng, Z., 2004: In situ determination of the compressibility of synthetic pure zircon (ZrSiO[sub4]) and the onset of the zircon-reidite phase transition: *American Mineralogist 89*, 197-203.

Von Engelhardt, W., 1997: Suevite breccia of the Ries impact crater, Germany: Petrography, chemistry and shock metamorphism of crystalline rock clasts: *Meteoritics & Planetary Science 32*, 545-554. doi: 10.1111/j.1945-5100.1997.tb01299.x

Wittmann, A., Kenkmann, T., Schmitt, R. T. & Stöffler, D., 2006: Shock-metamorphosed zircon in terrestrial impact craters: *Meteoritics & Planetary Science 41*, 433-454. doi: 10.1111/j.1945-5100.2006.tb00472.x

Zhang, M., Salje, E. K. H., Farnan, I., Graeme-Barber, A., Daniel, P., Ewing, R. C., Clark, A. M. & Leroux, H., 2000: Metamictization of zircon: Raman spectroscopic study: *Journal of Physics: Condensed Matter 12*, 1915.

Zhang, A.-C., Hsu, W.-B., Li, X.-H., Ming, H.-L., Li, Q.-L., Liu, Y. & Tang, G.-Q., 2011: Impact melting of lunar meteorite Dhofar 458: Evidence from polycrystalline texture and decomposition of zircon. *Meteoritics & Planetary Science 46*, 103-115. doi: 10.1111/j.1945-5100.2010.01144.x

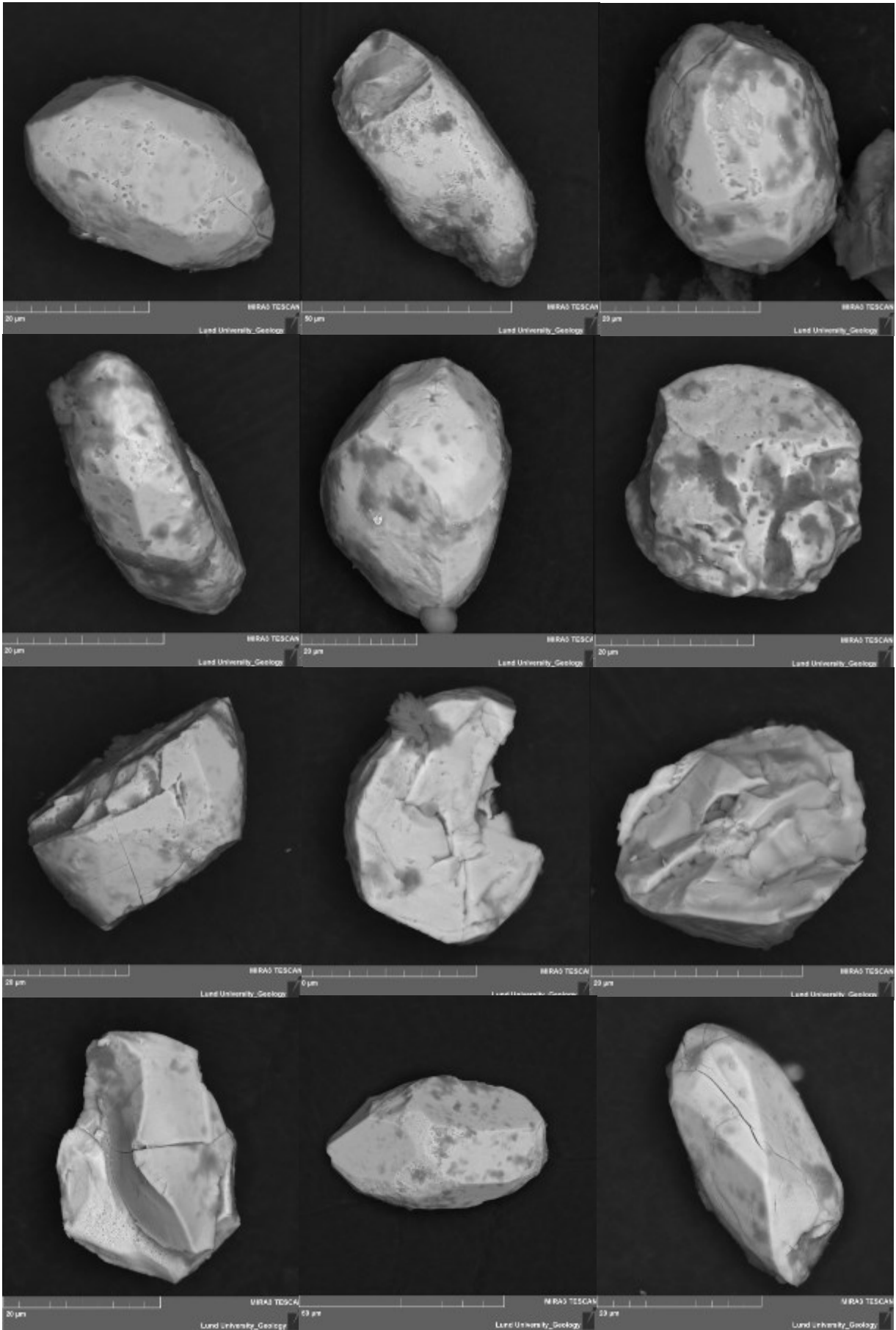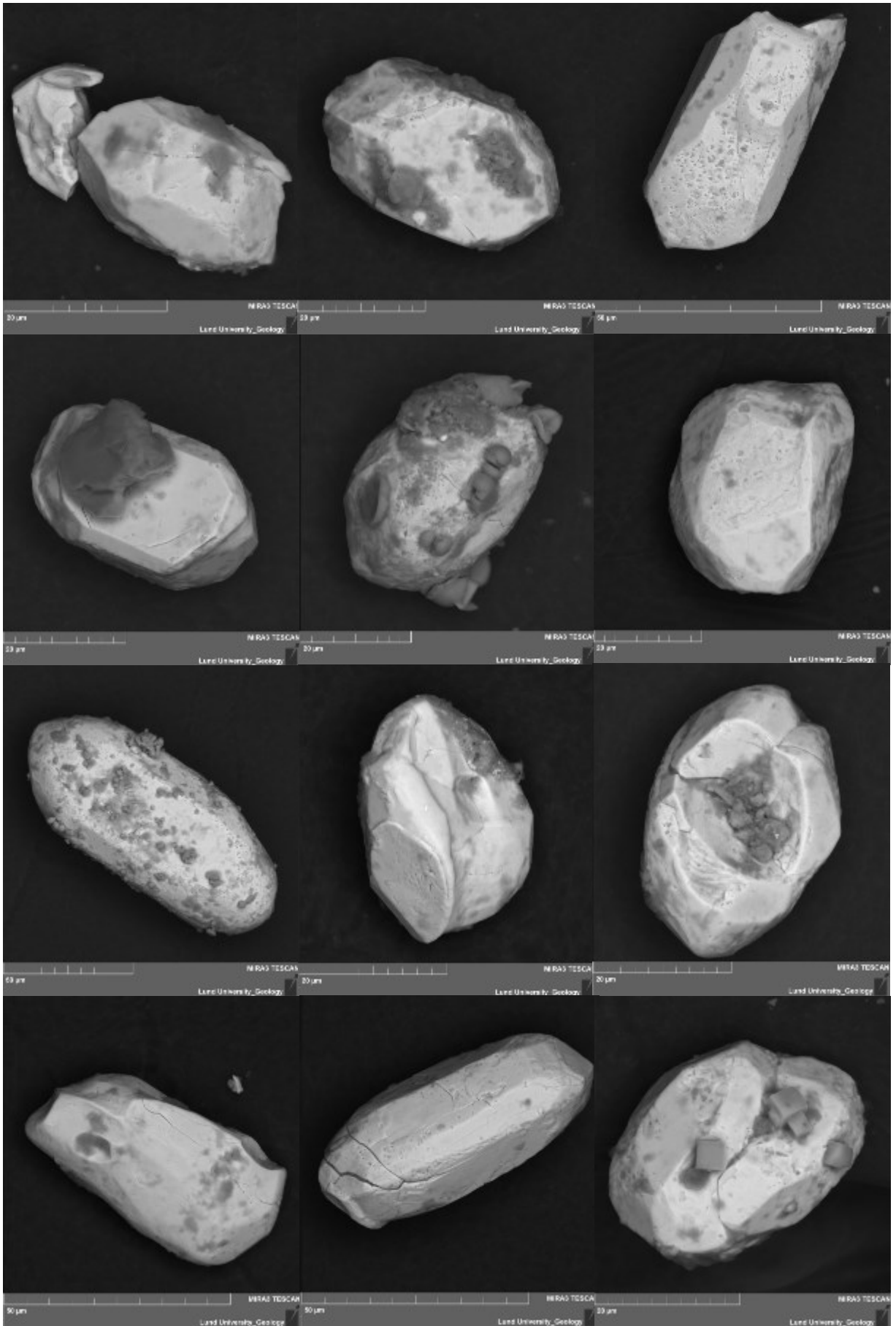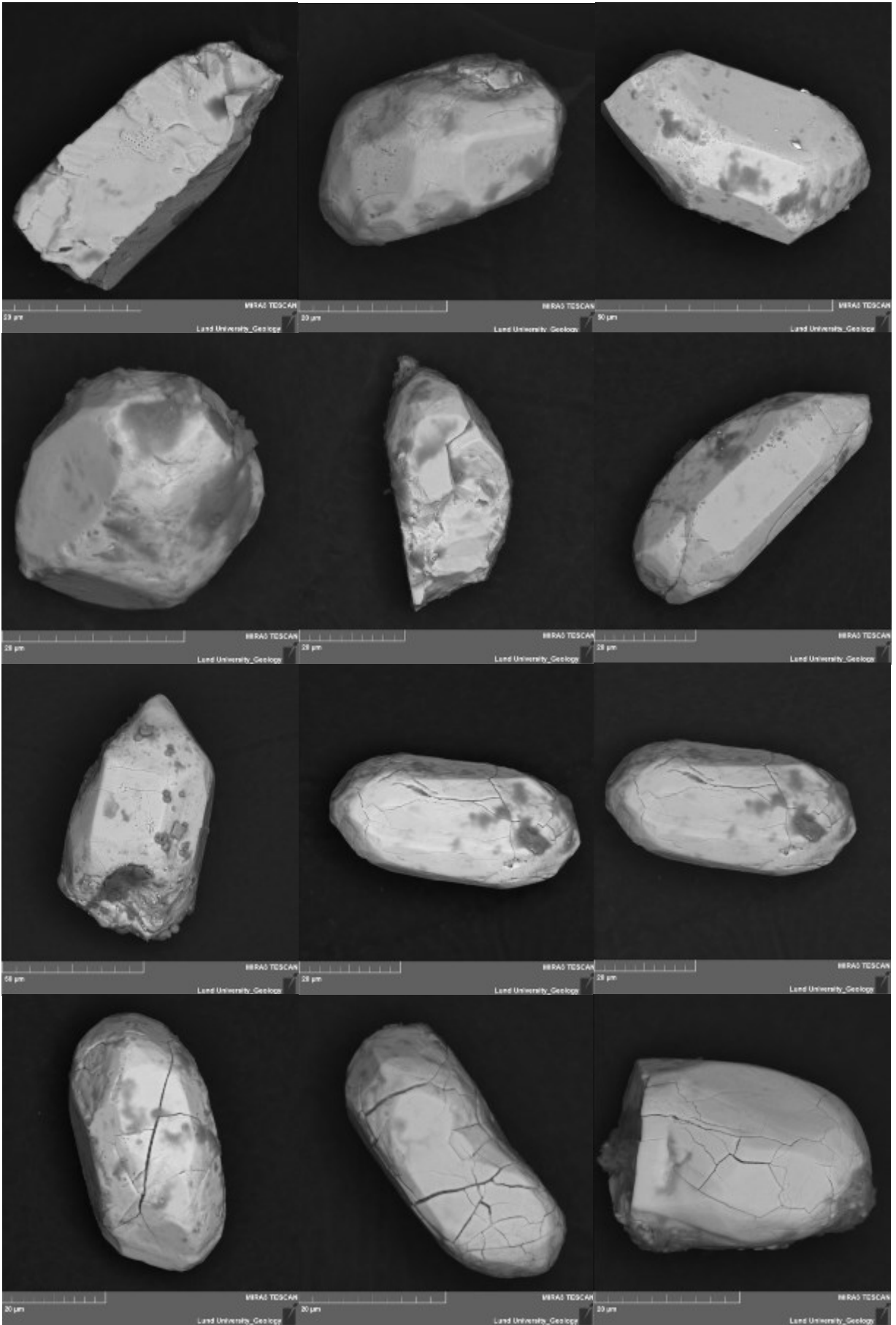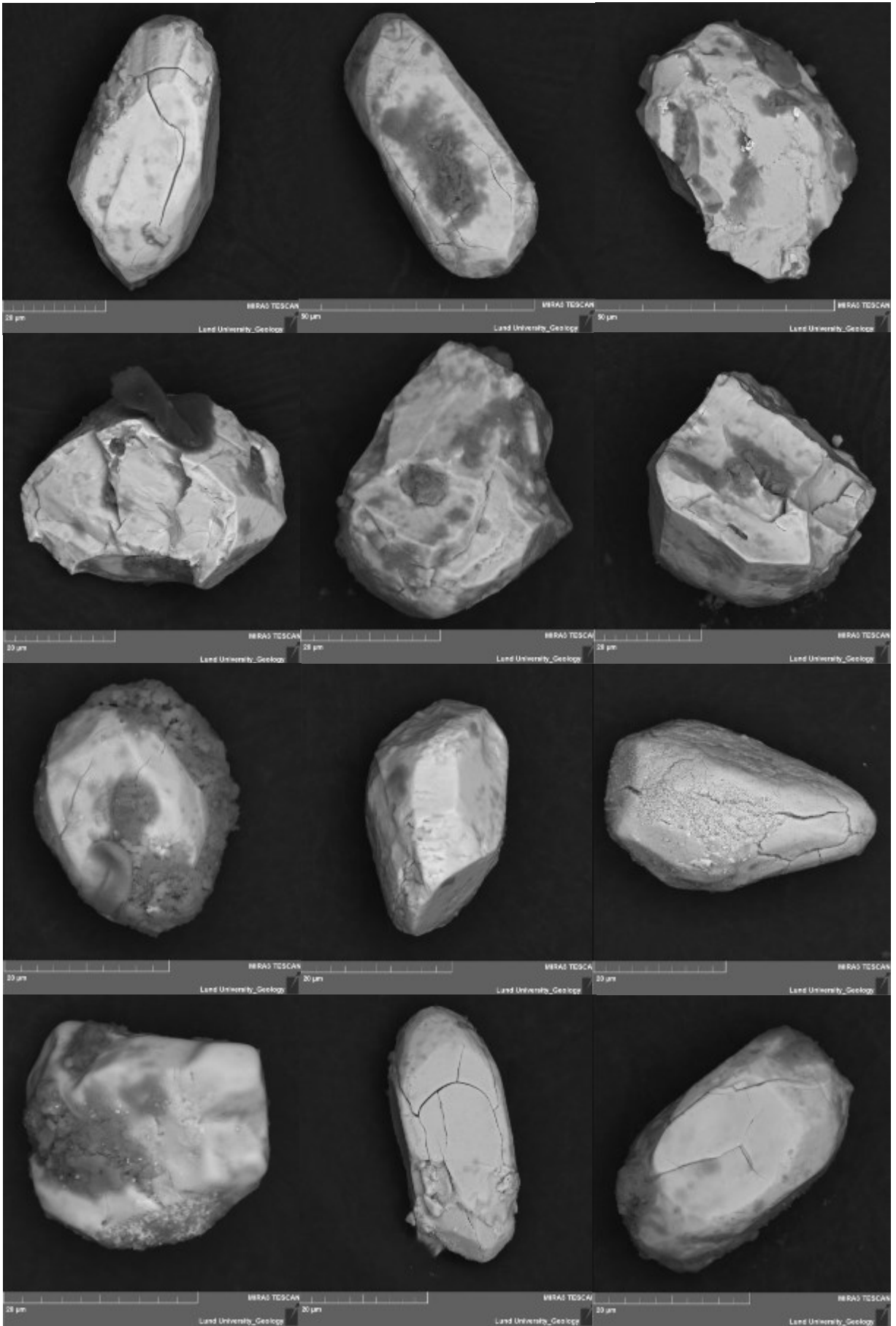# 10. Appendix

10.1 Clast-poor impact melt (SEM)
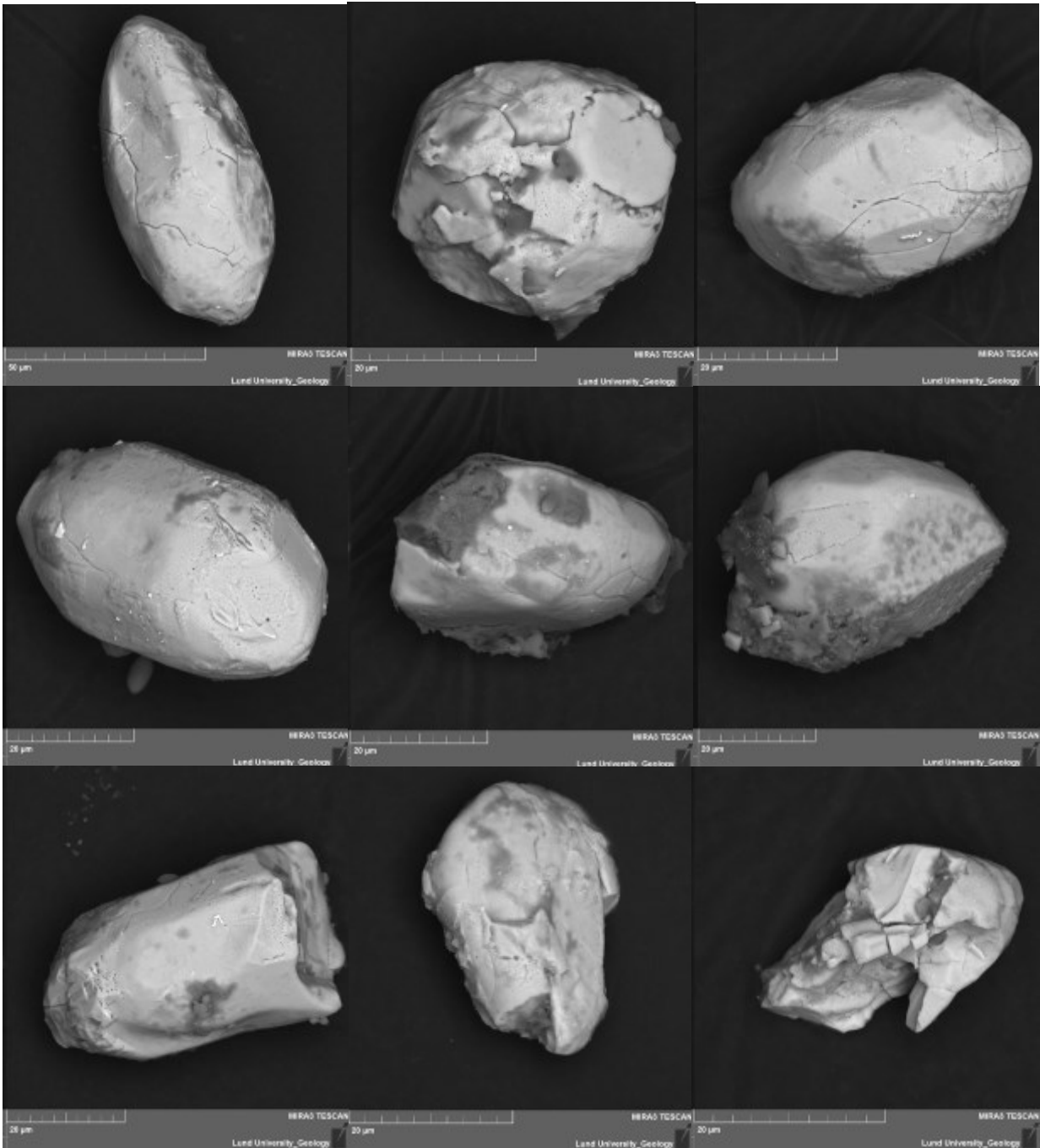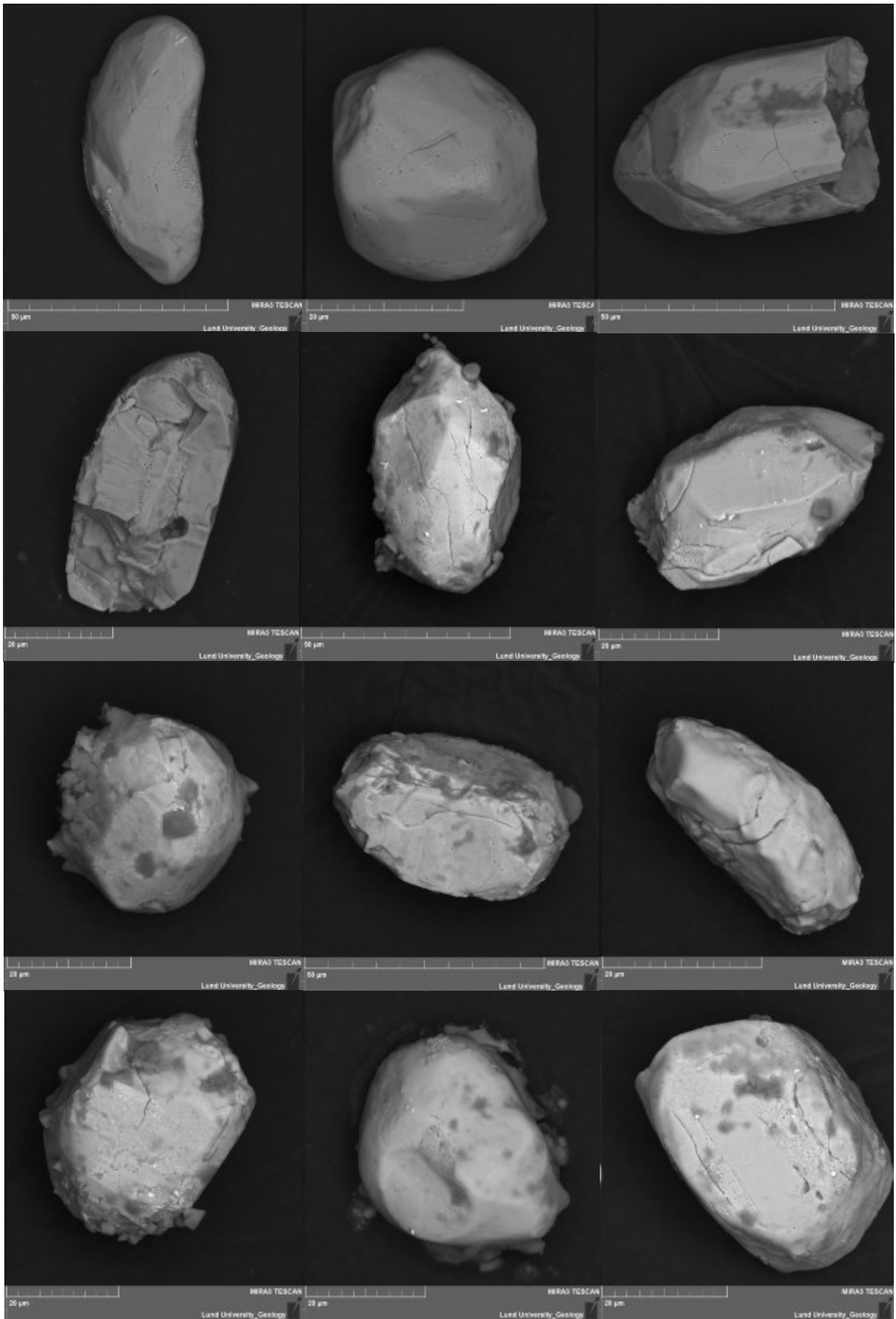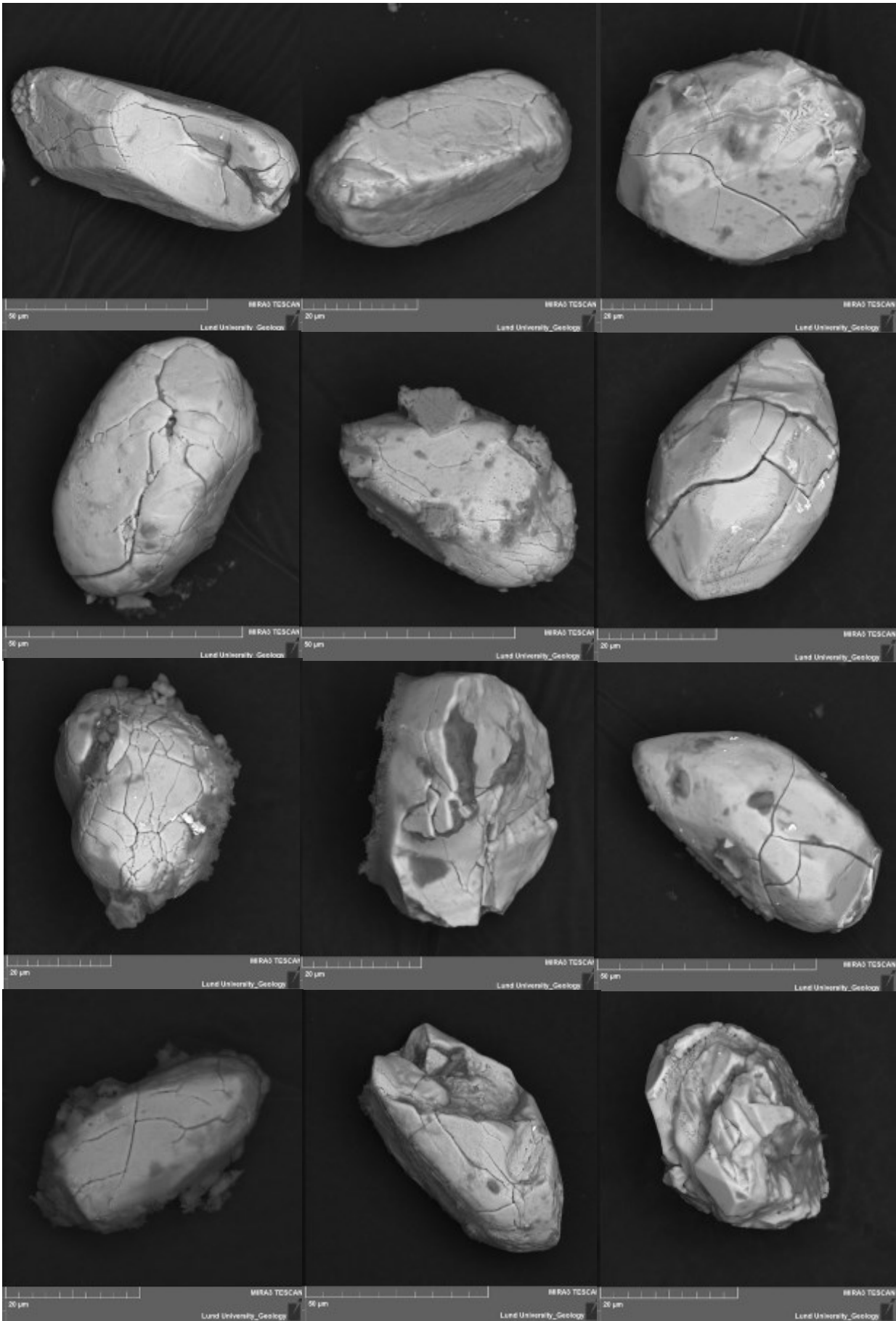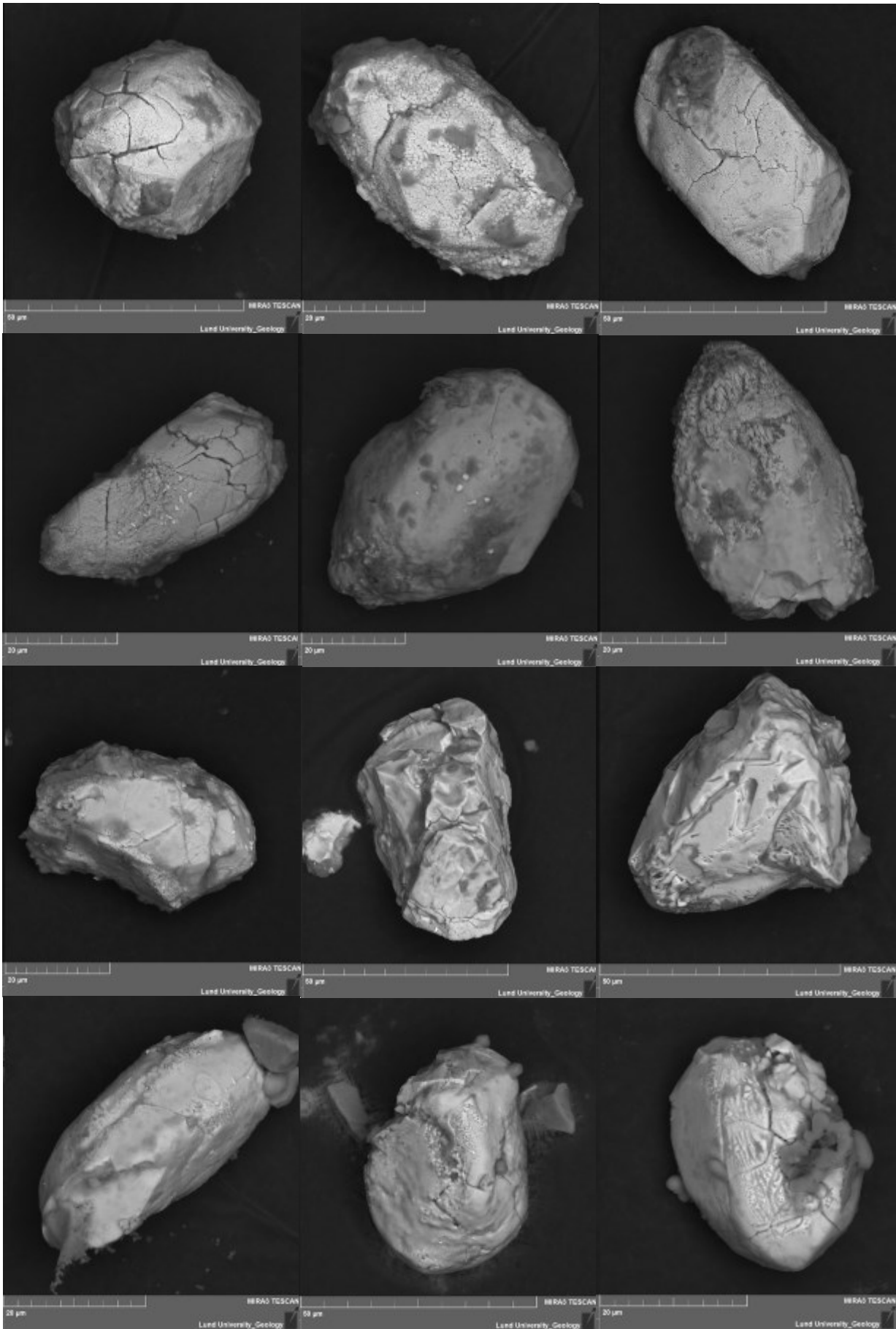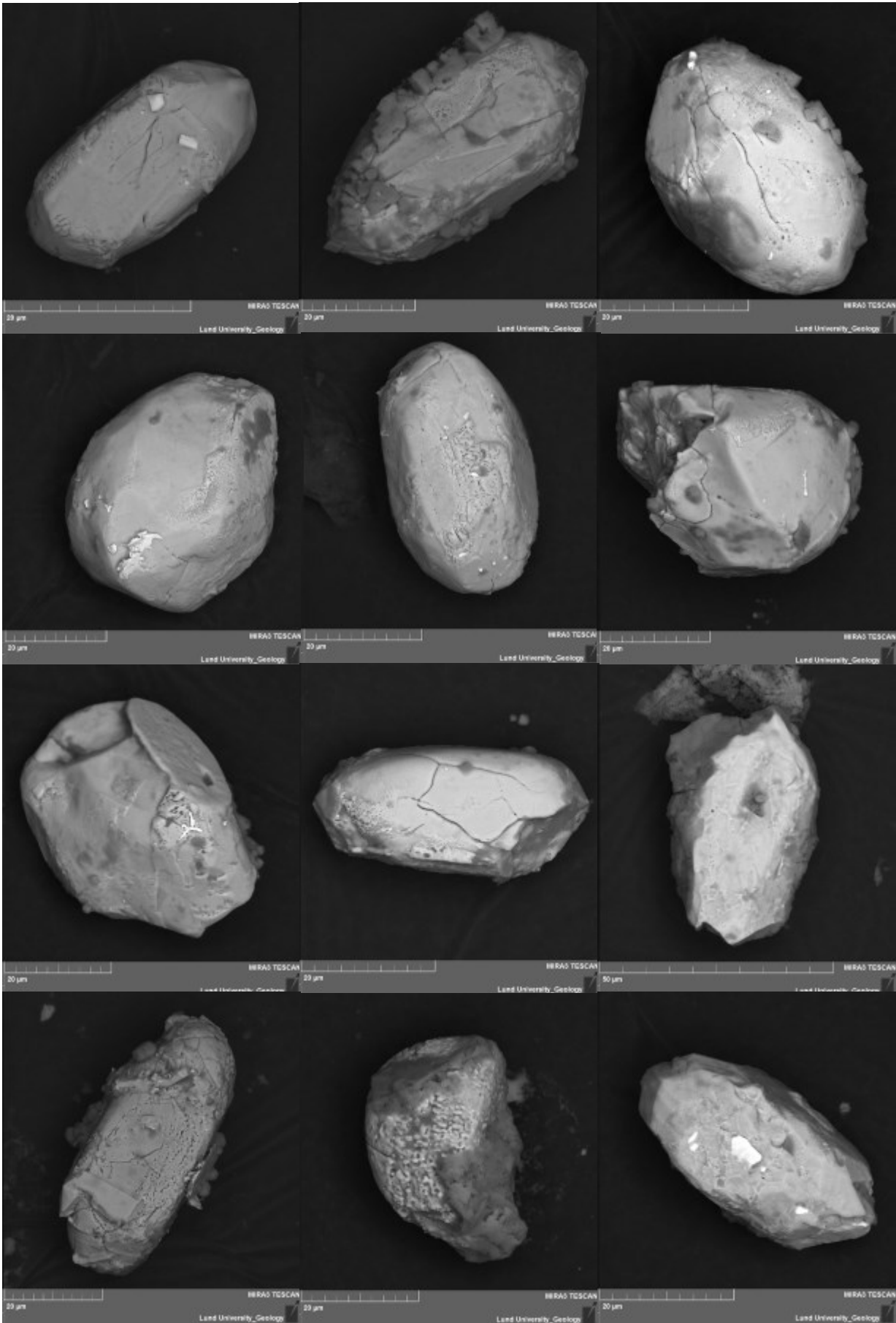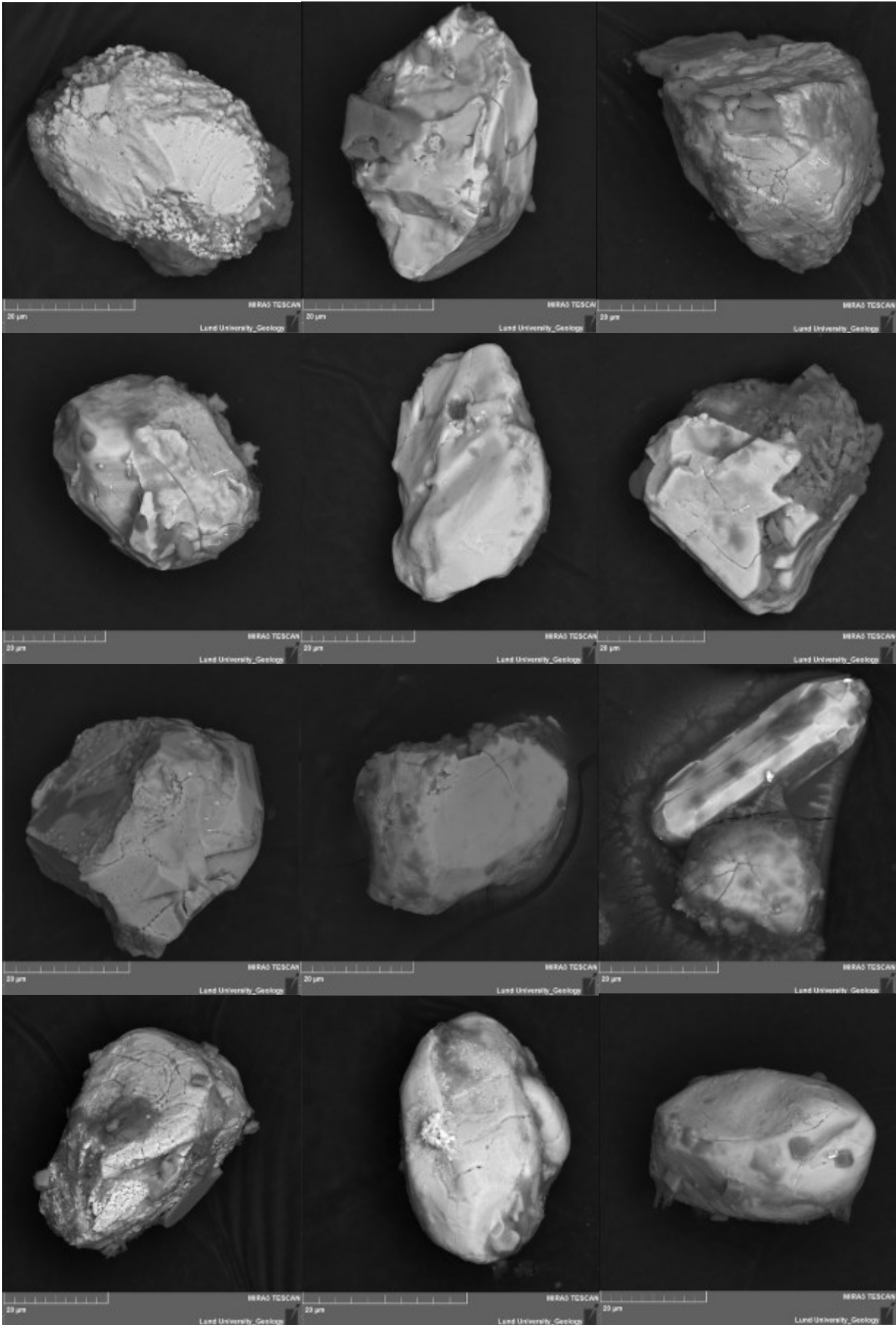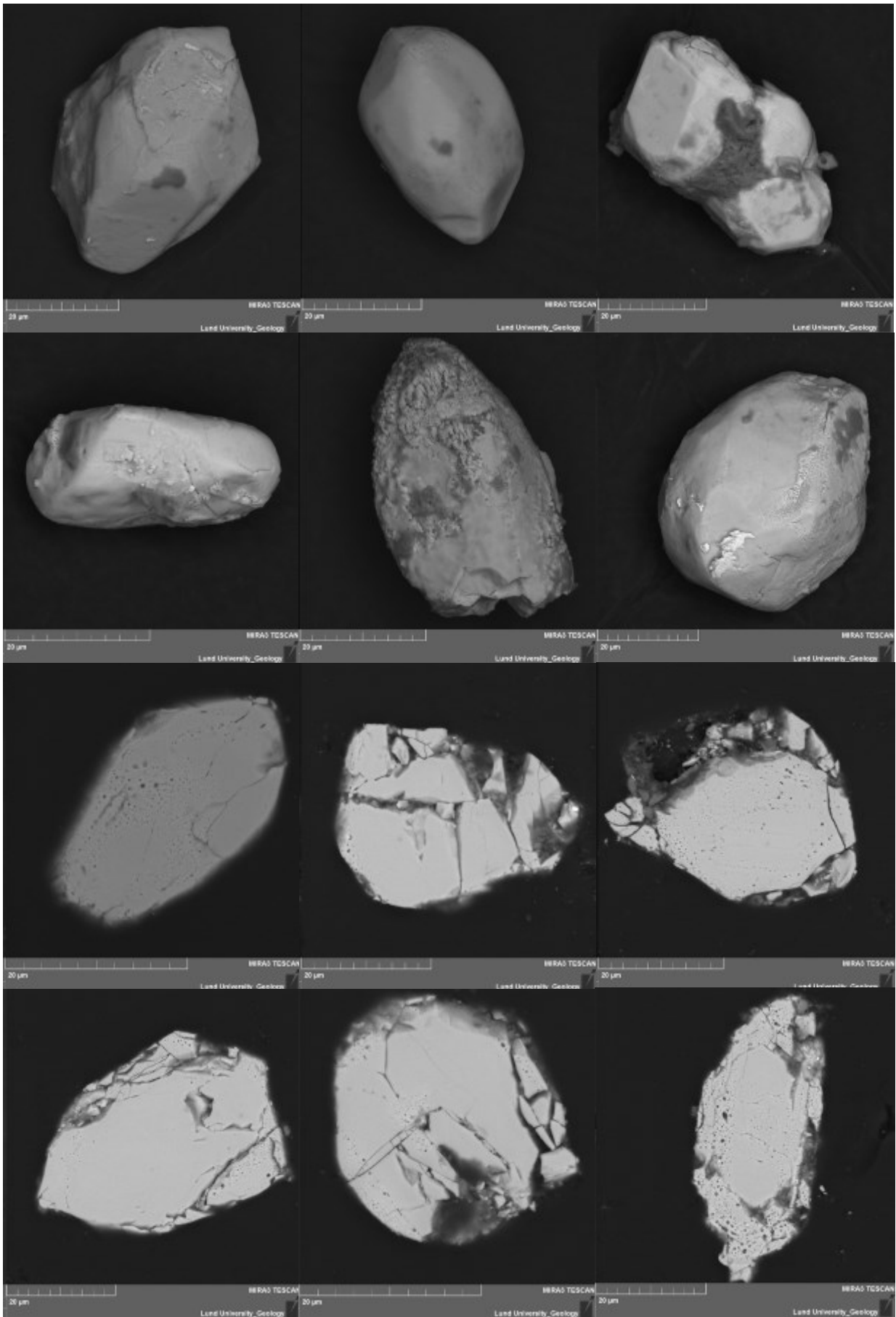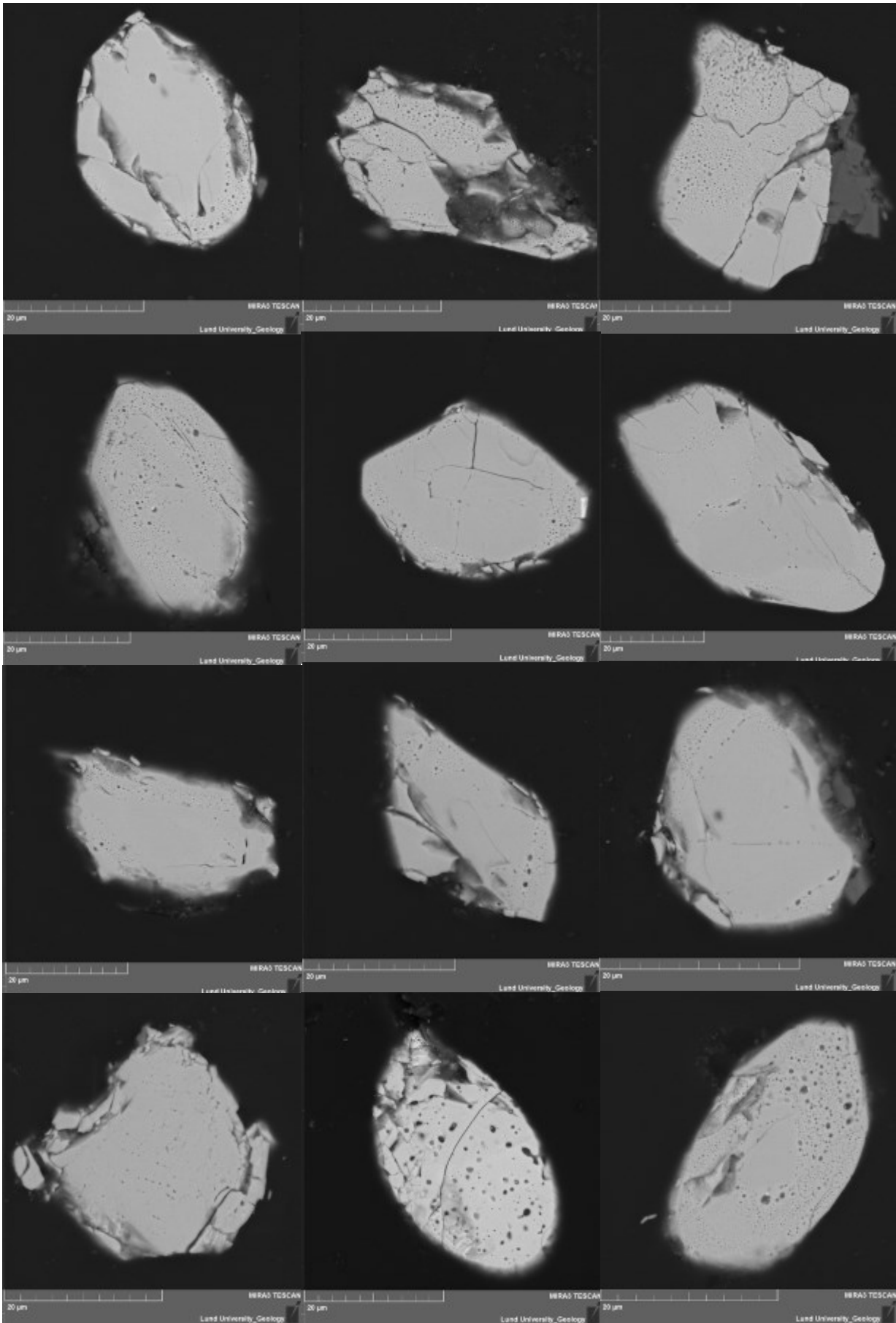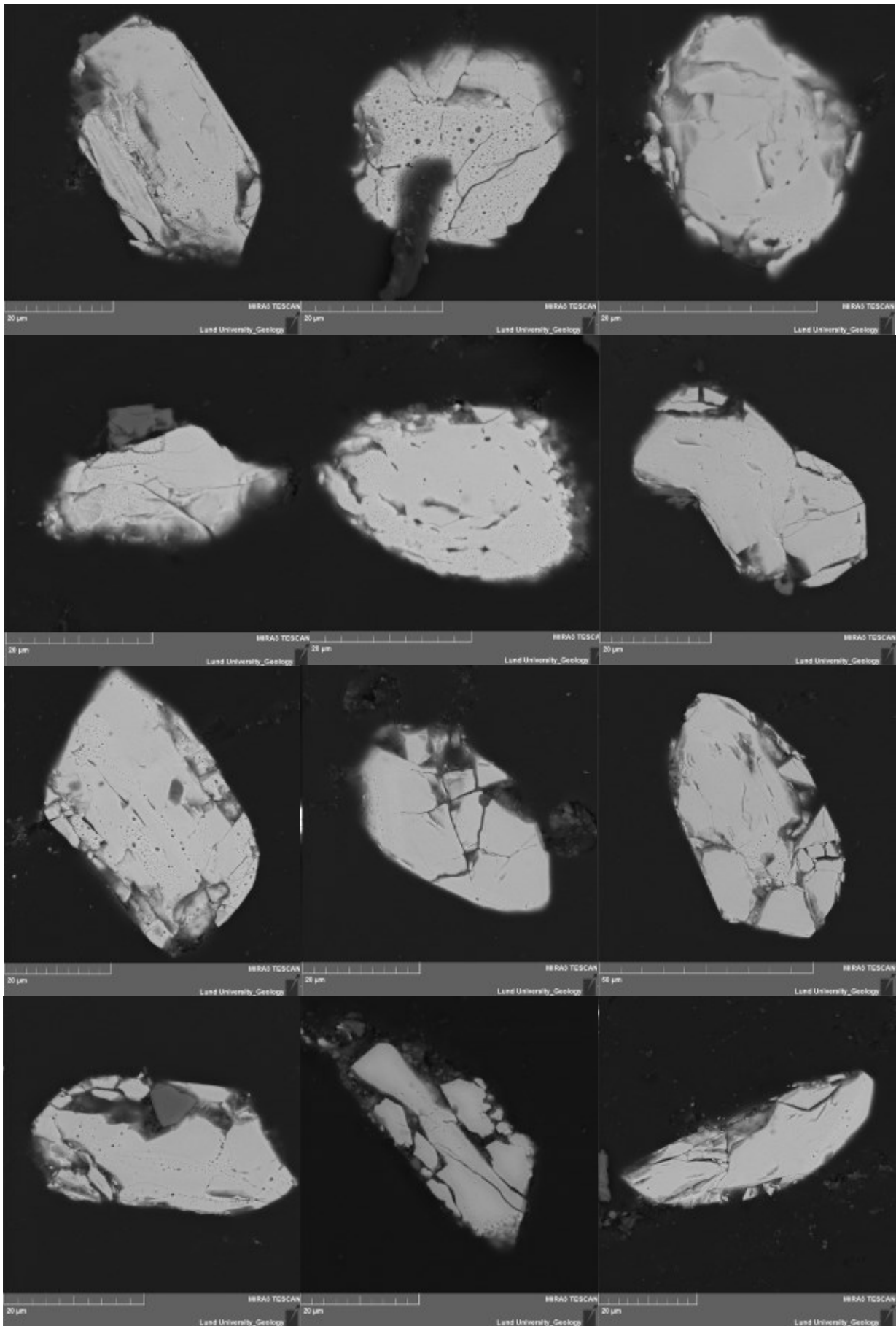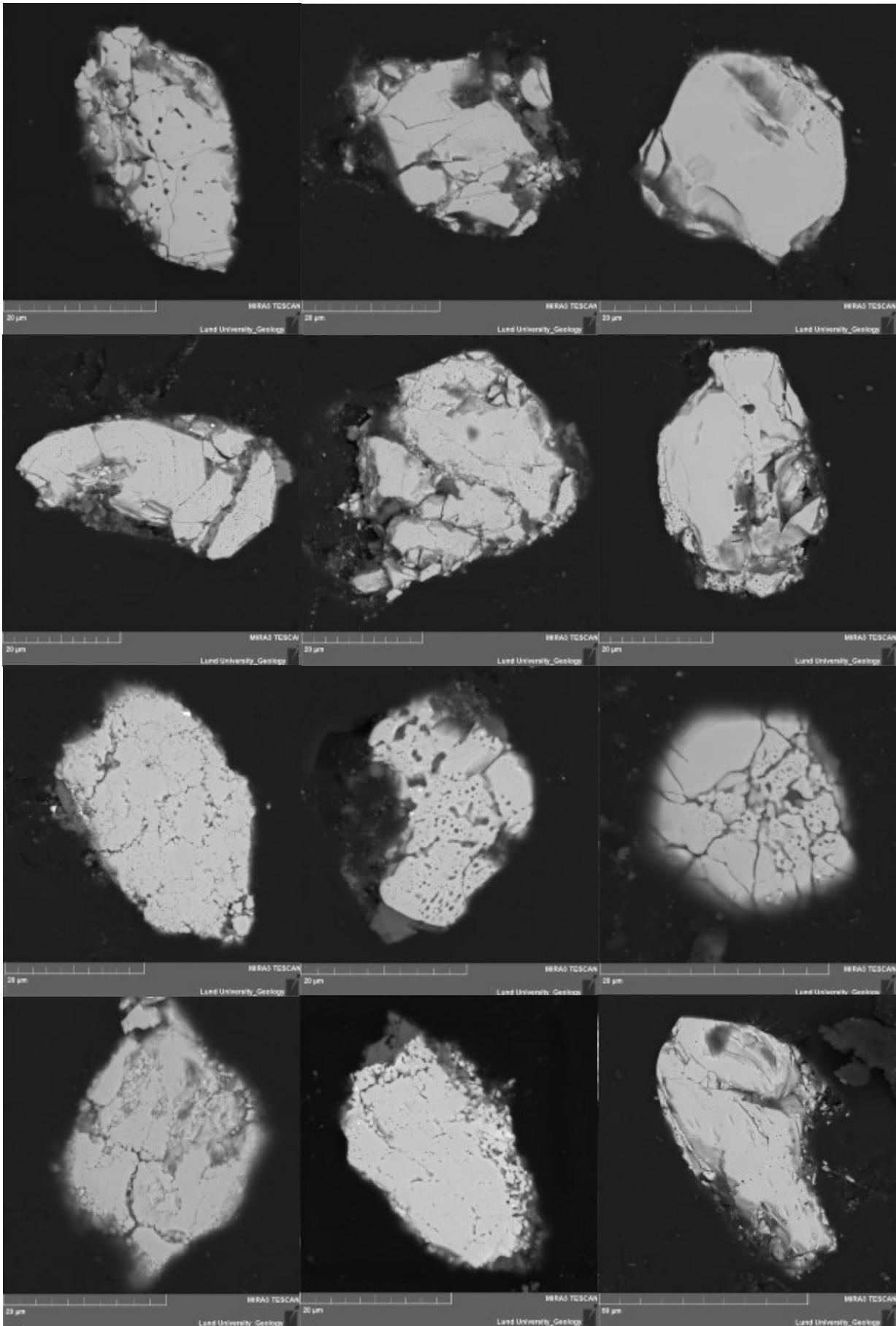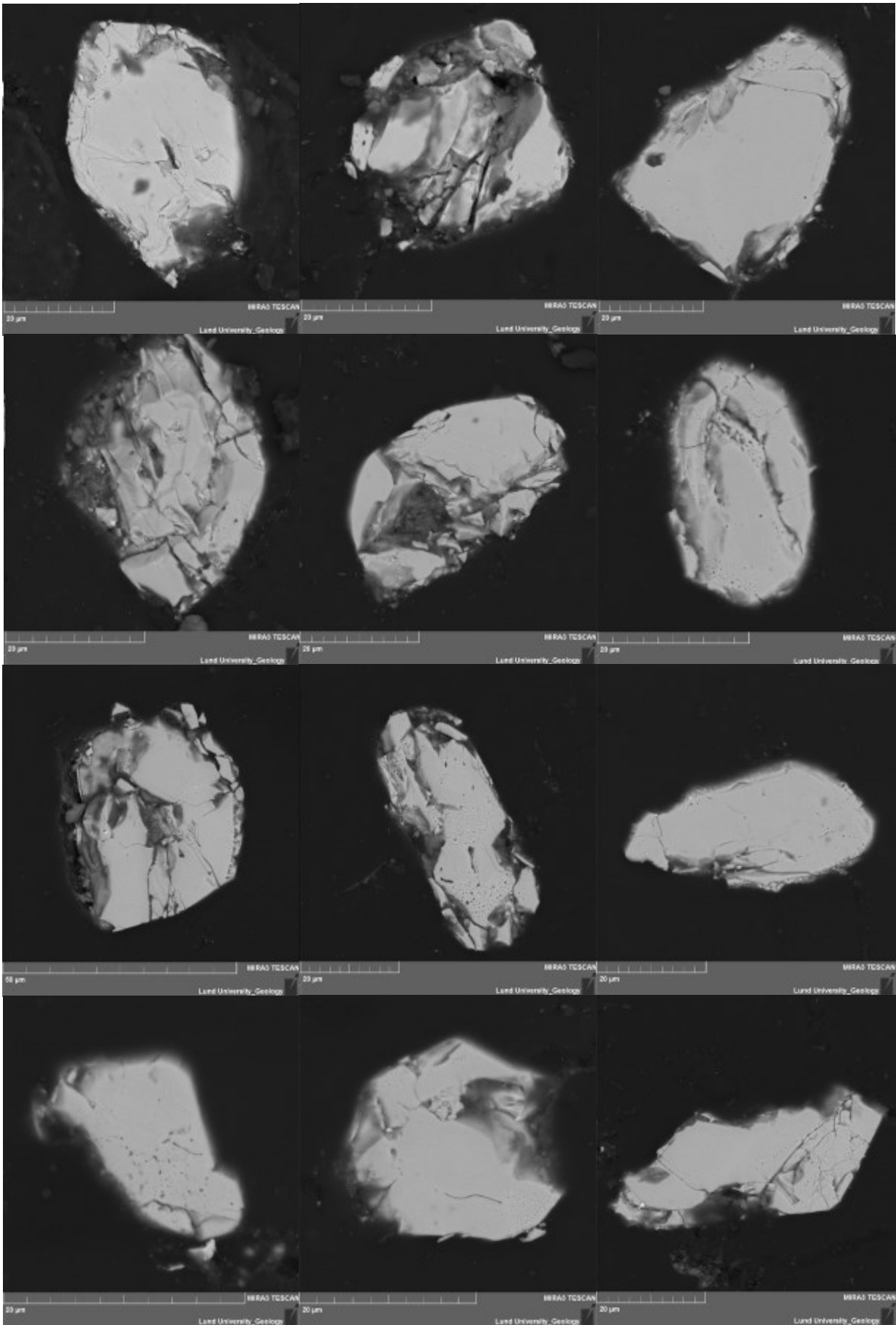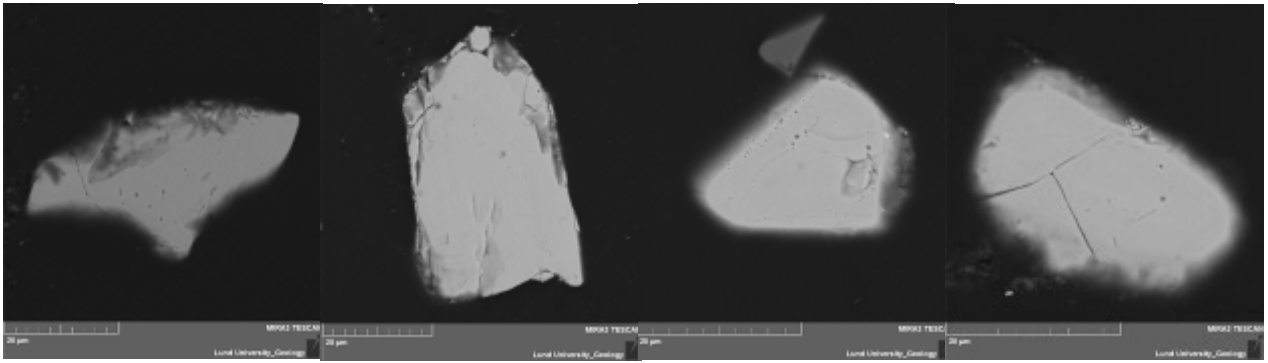
10.2 Clast-rich impact melt rock (SEM)
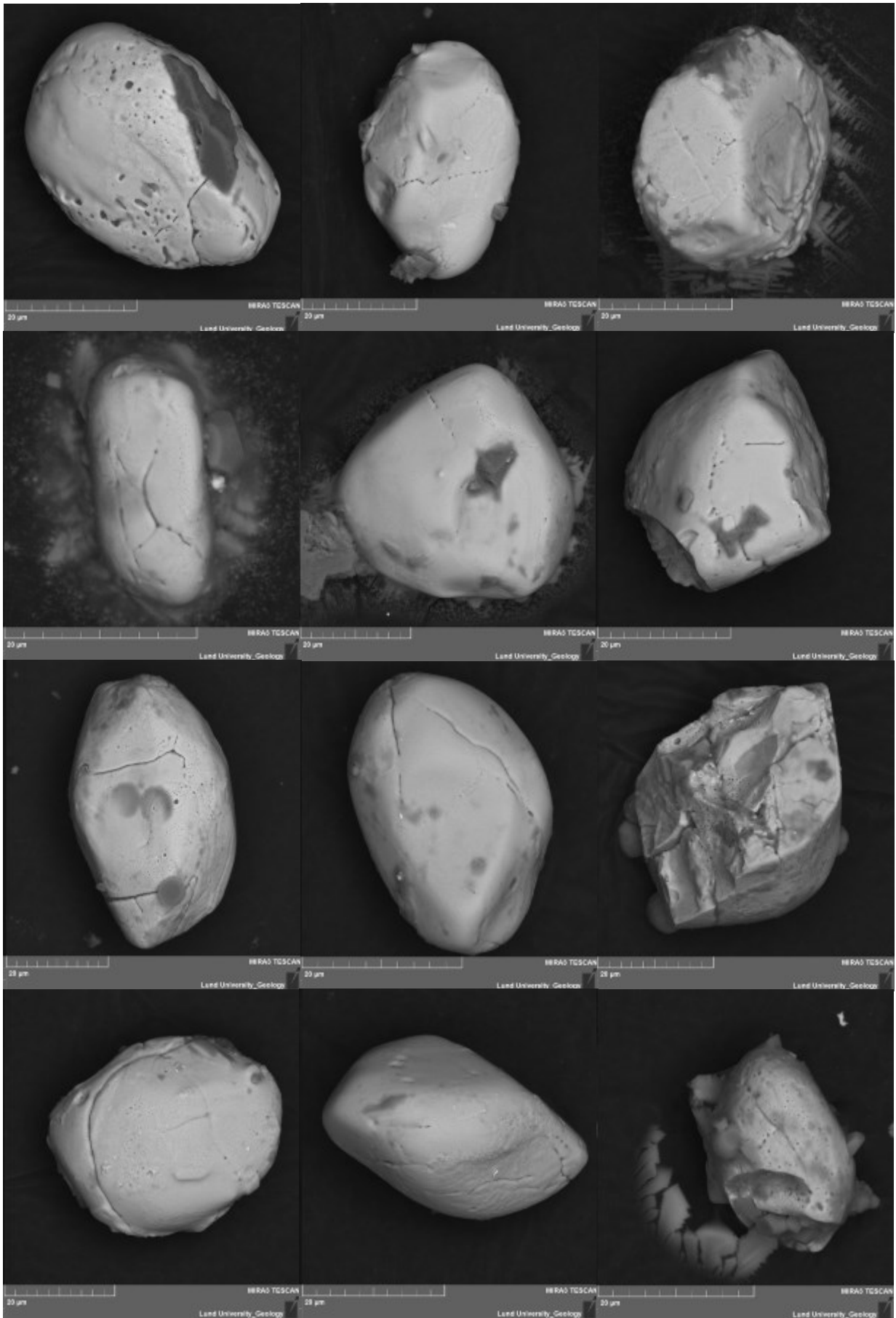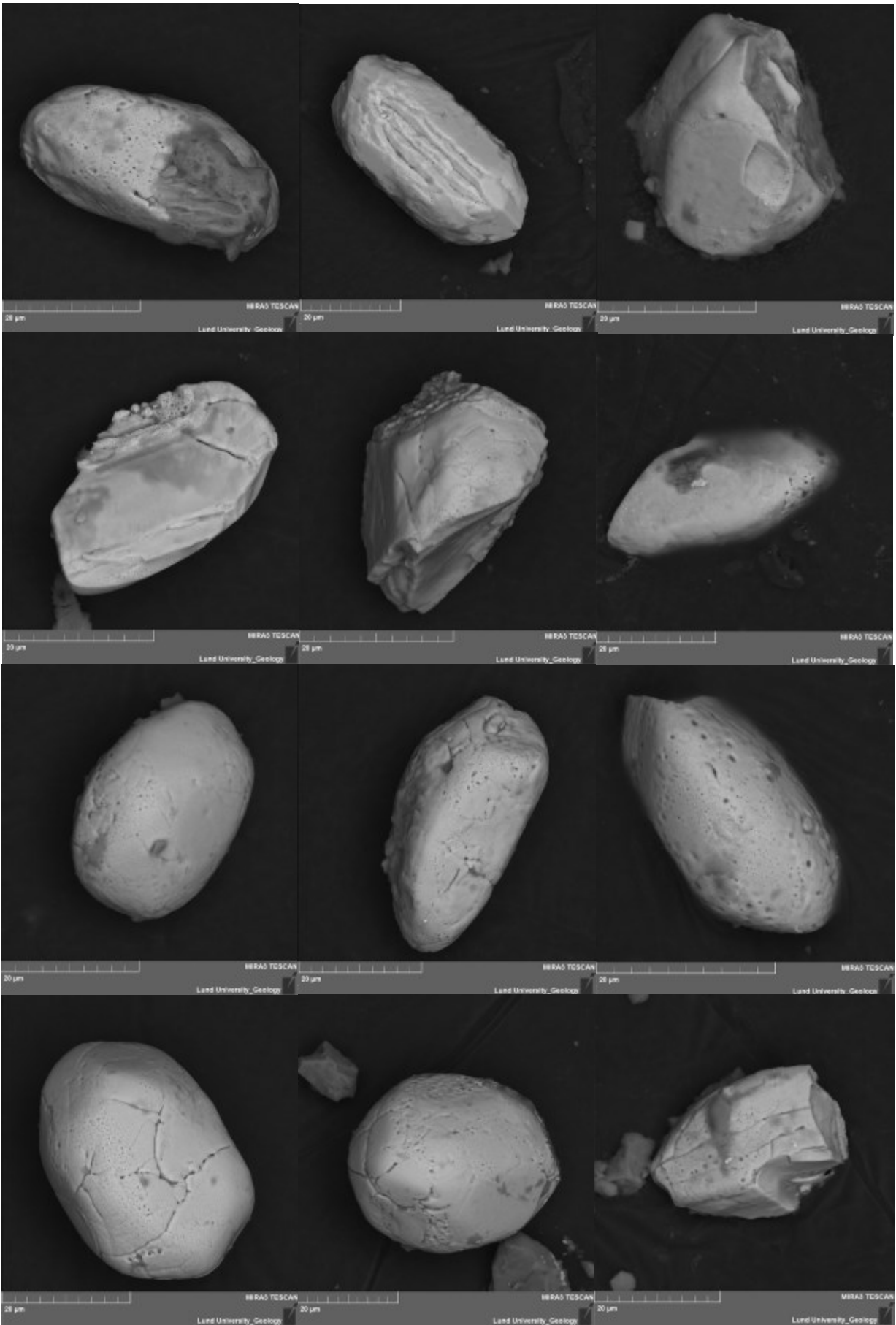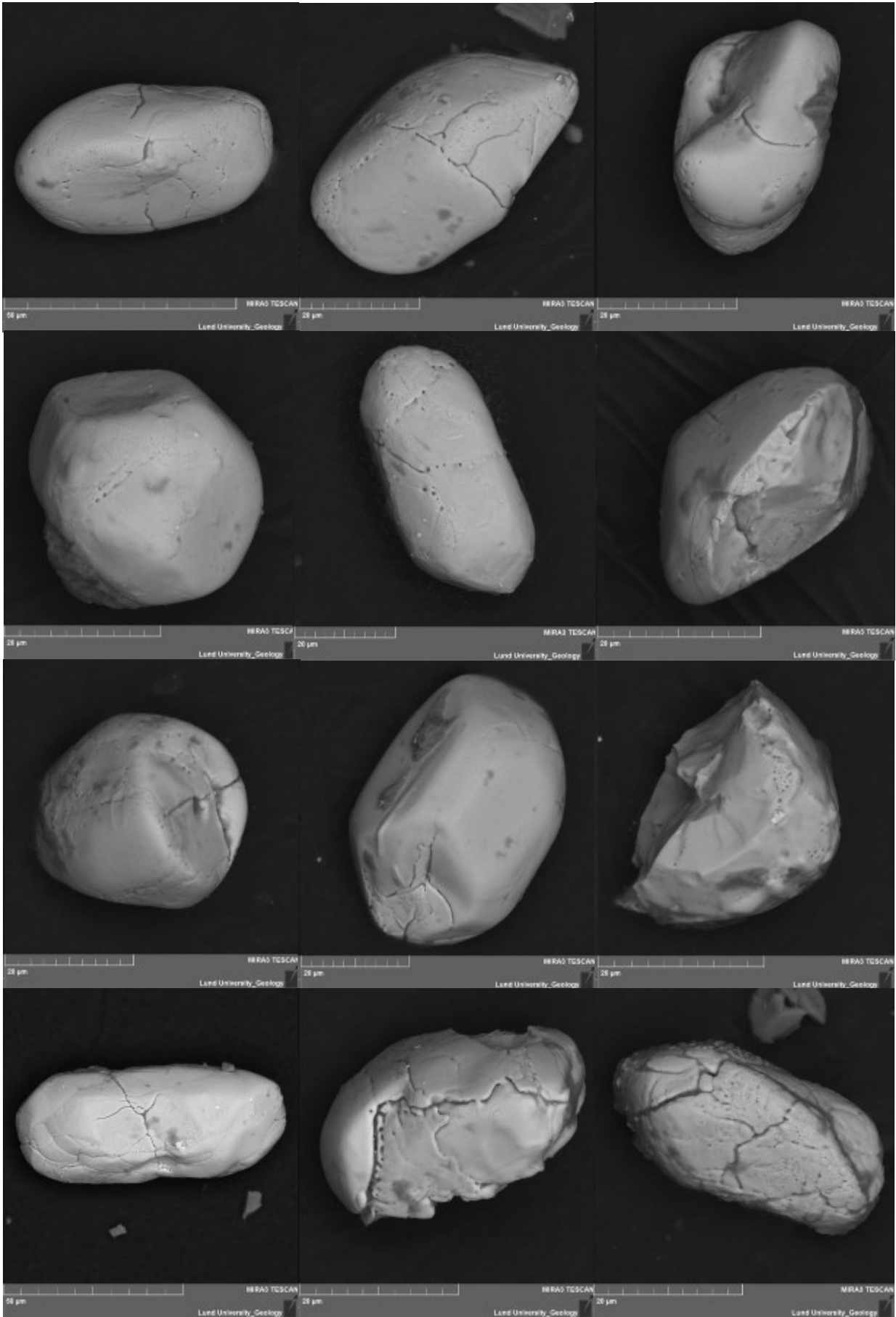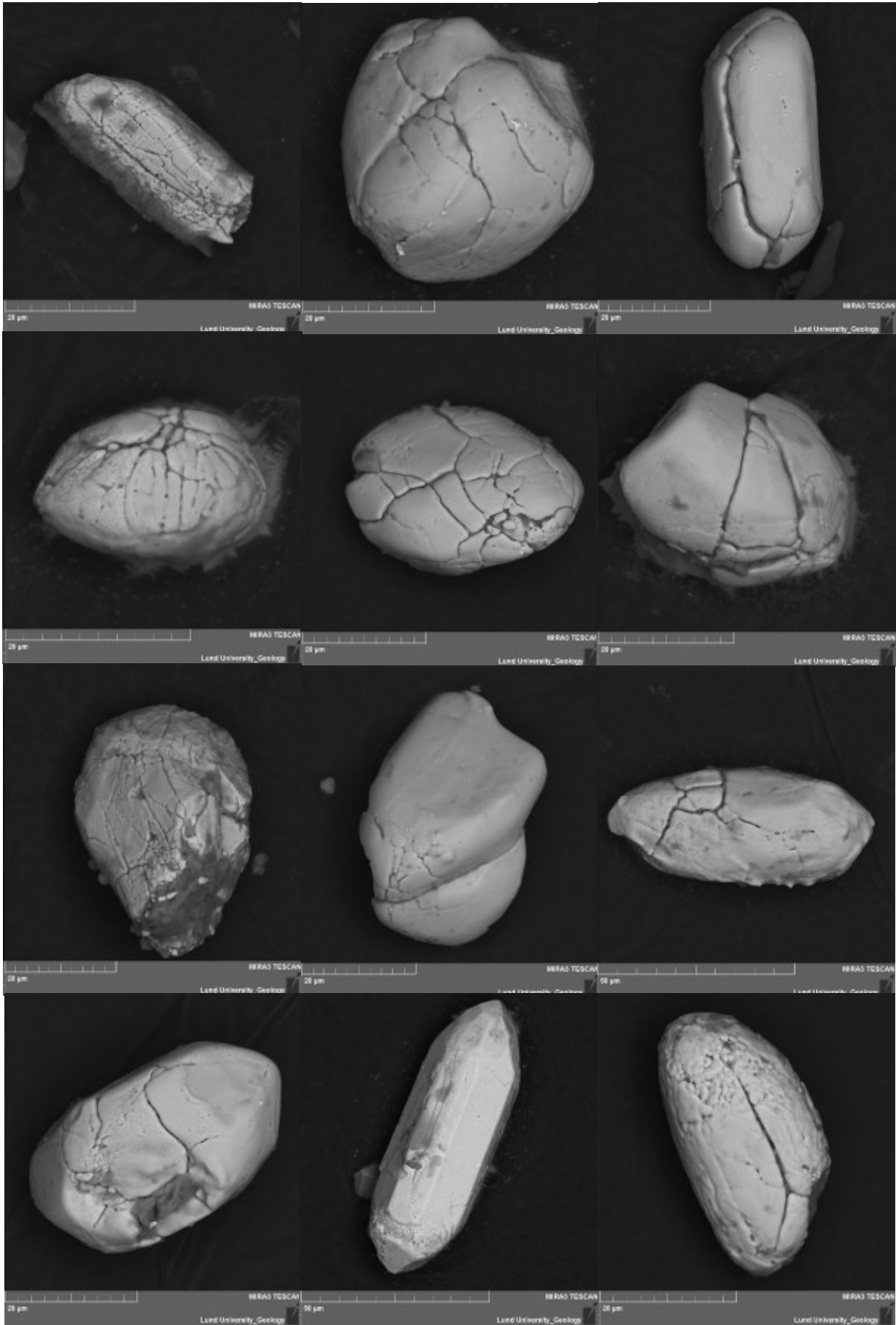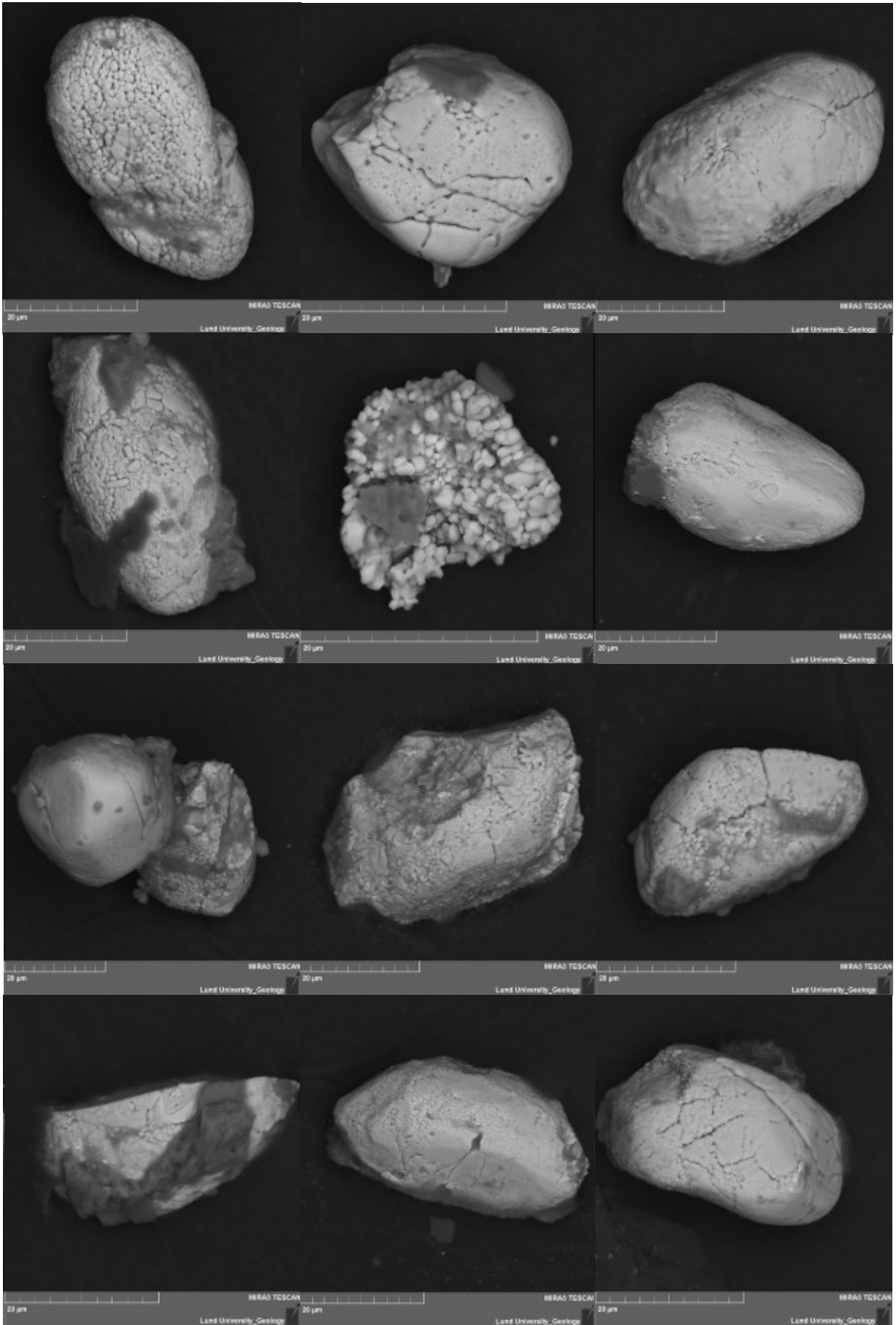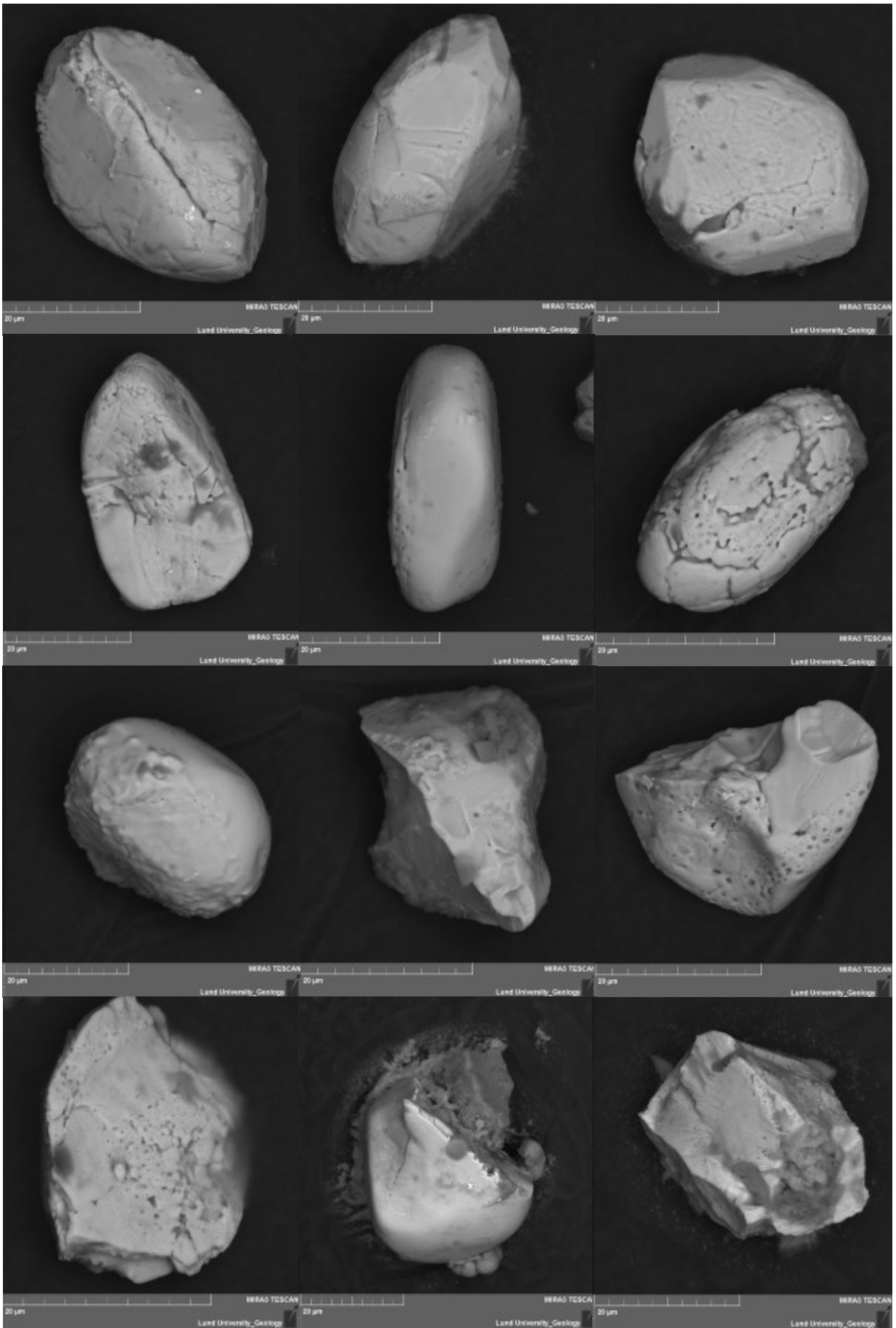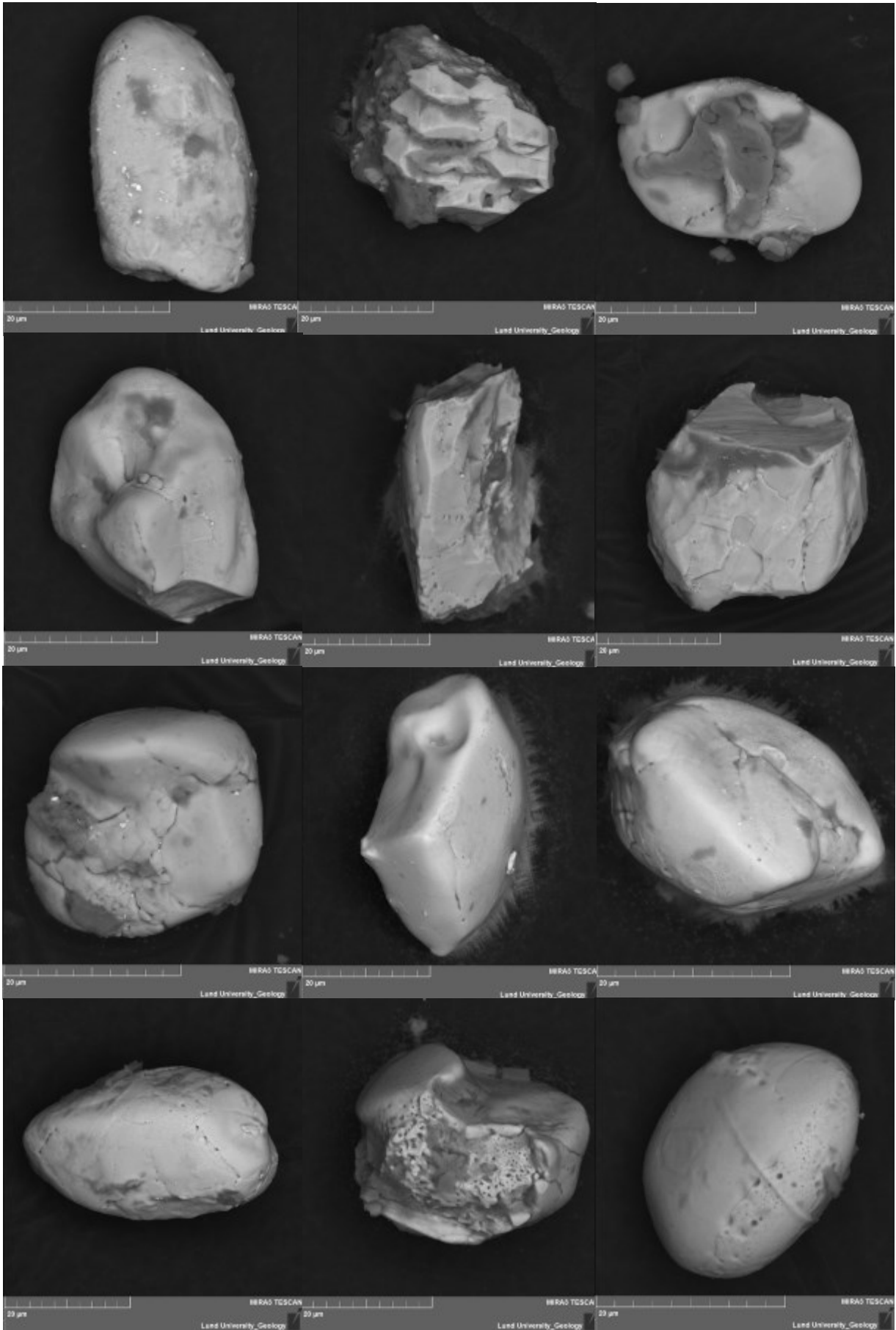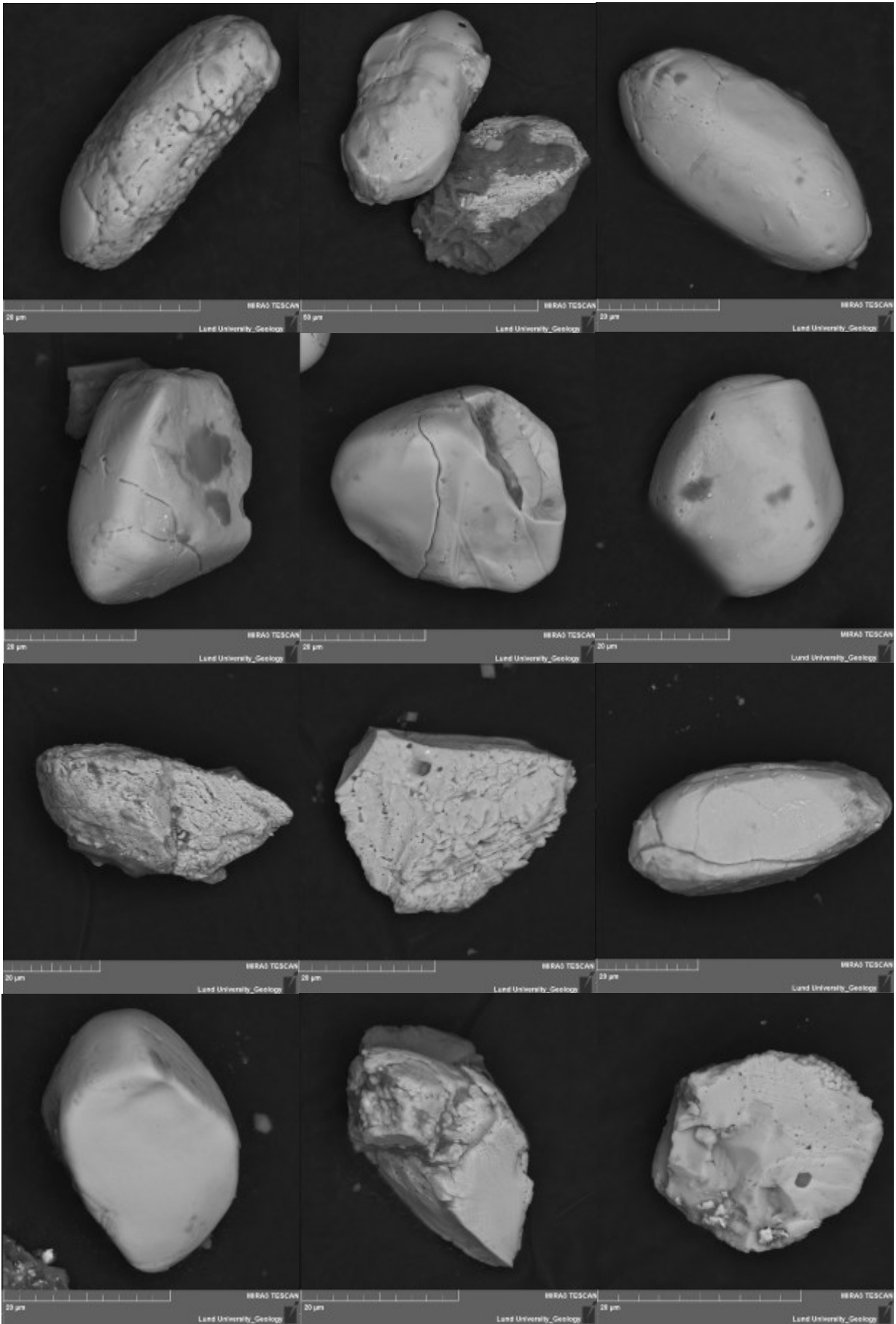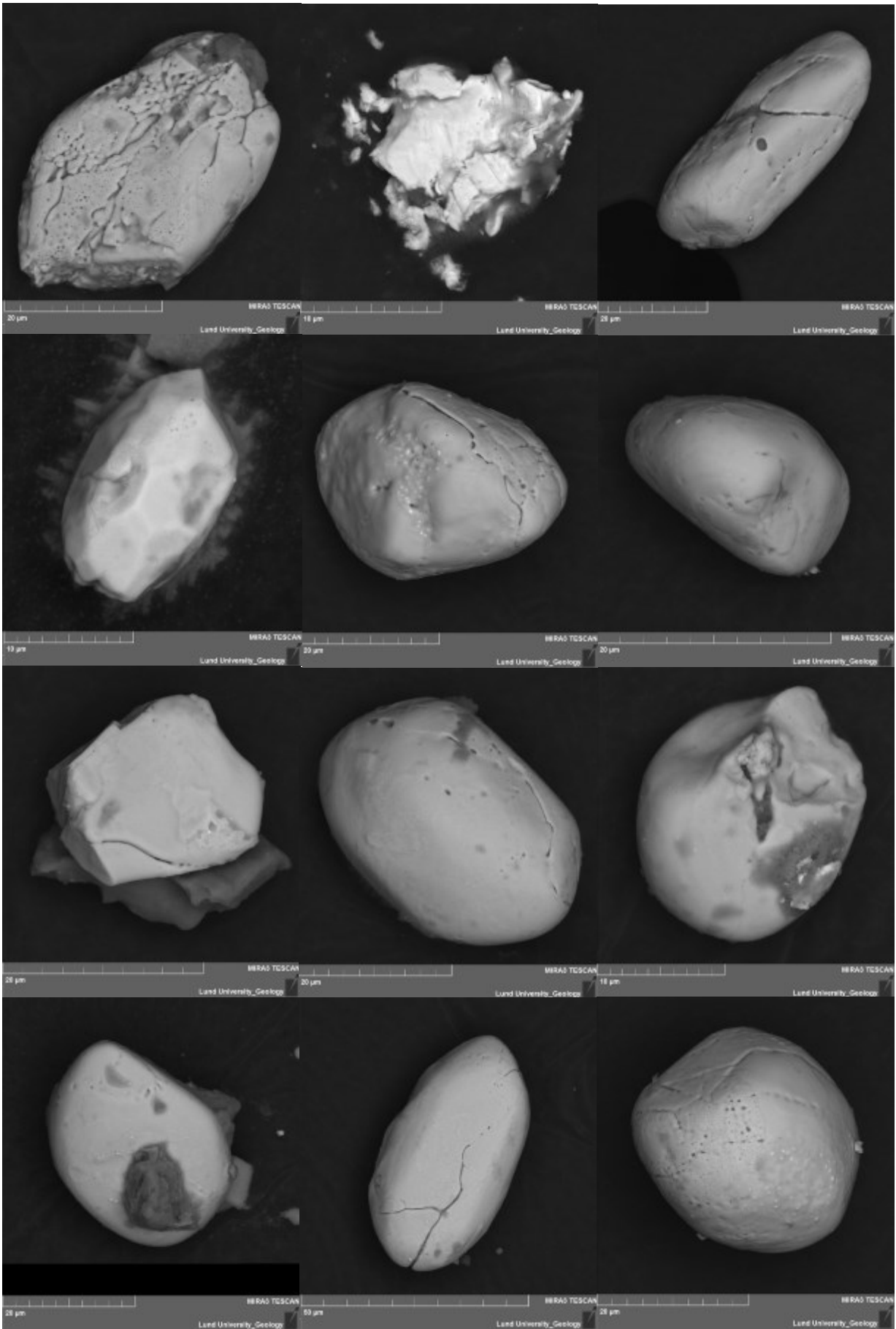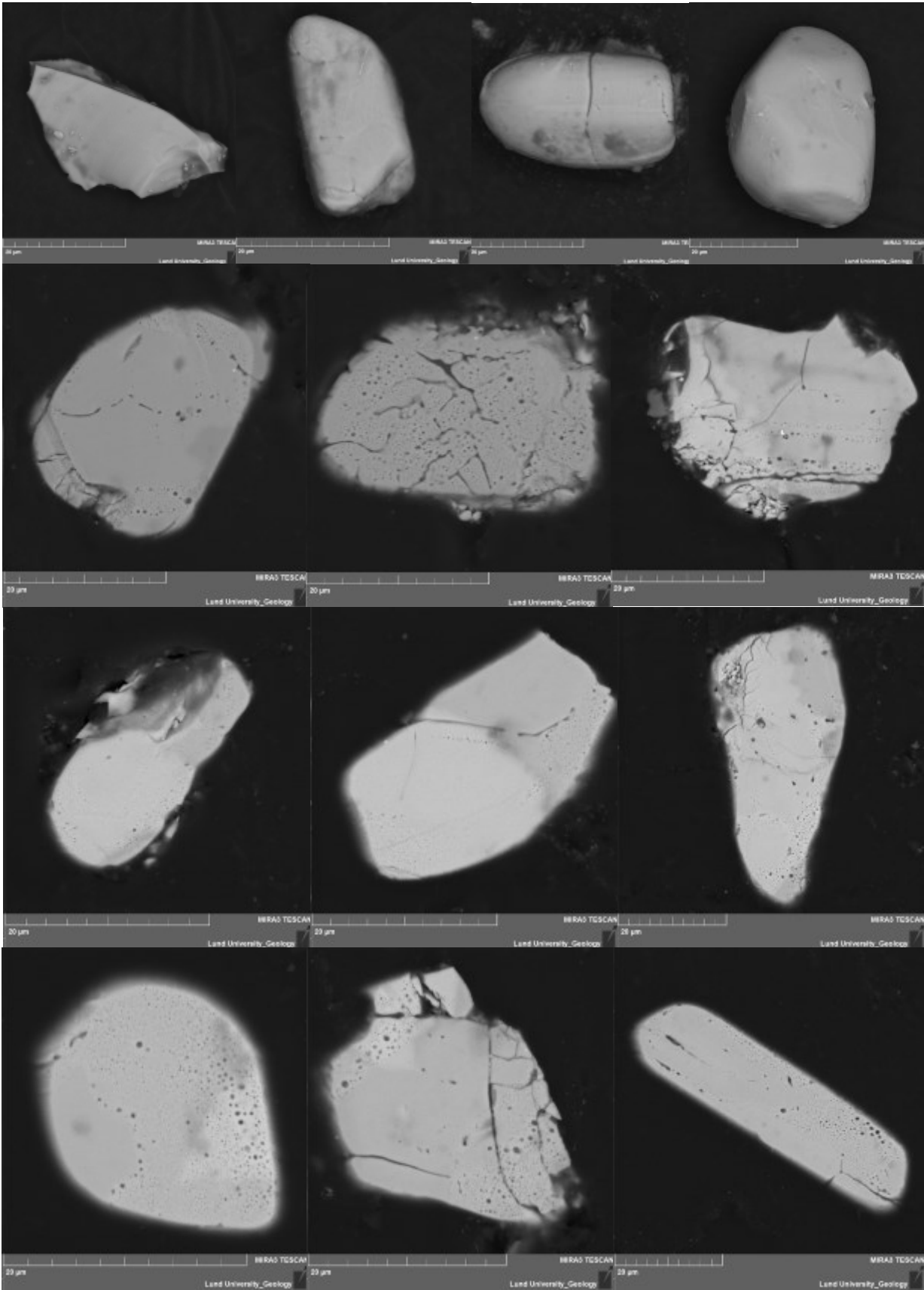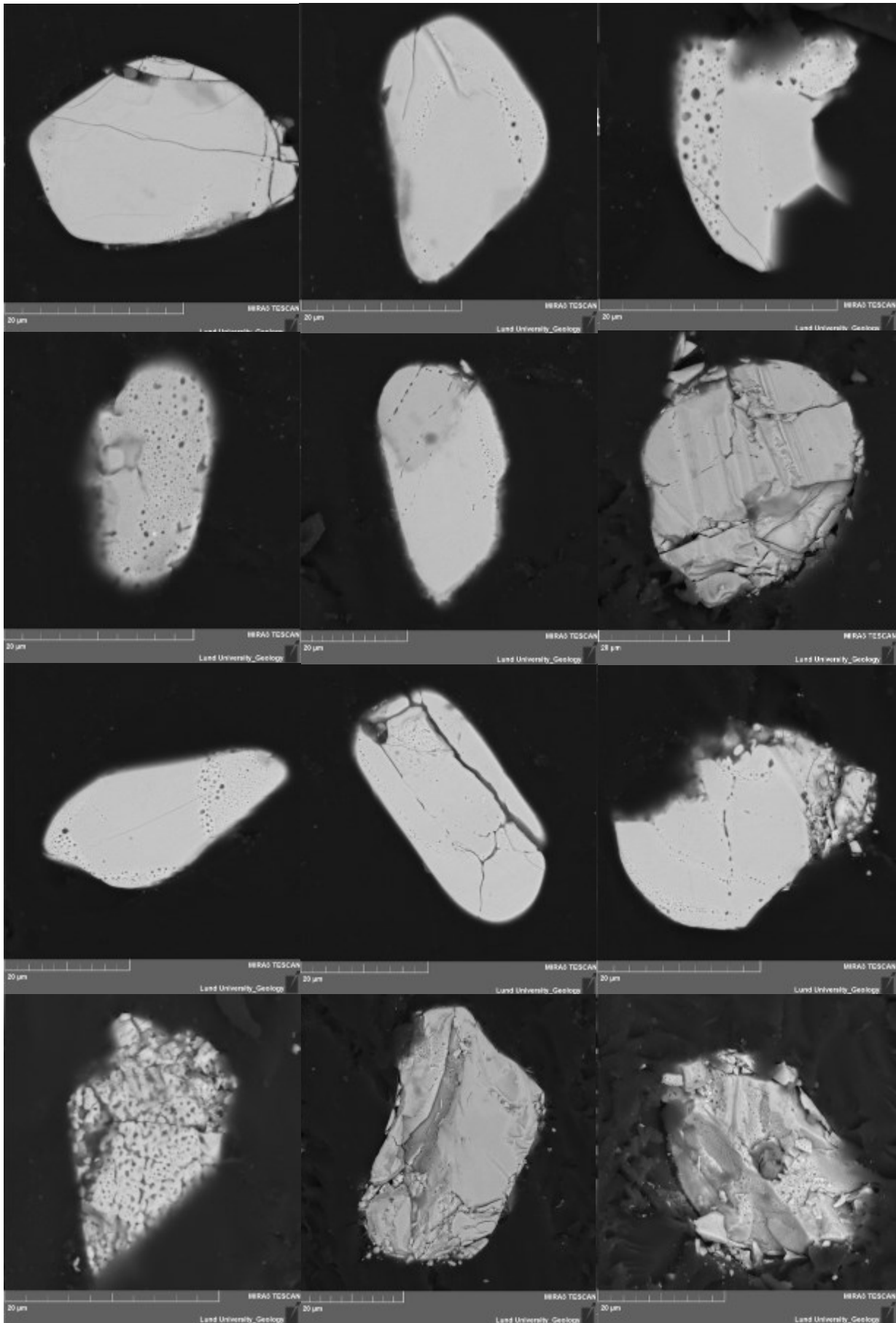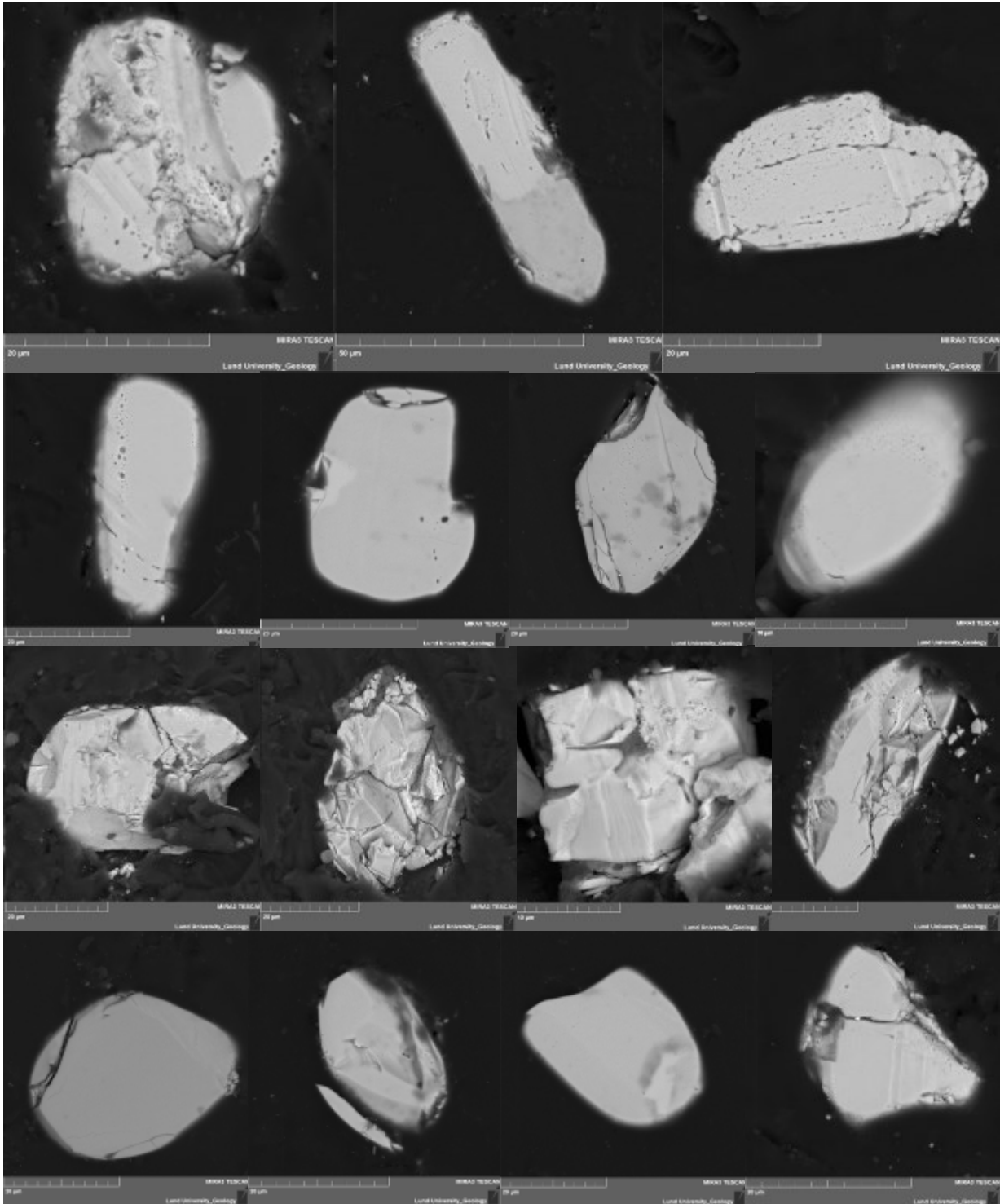
10.3 "Suevite" breccia (SEM)
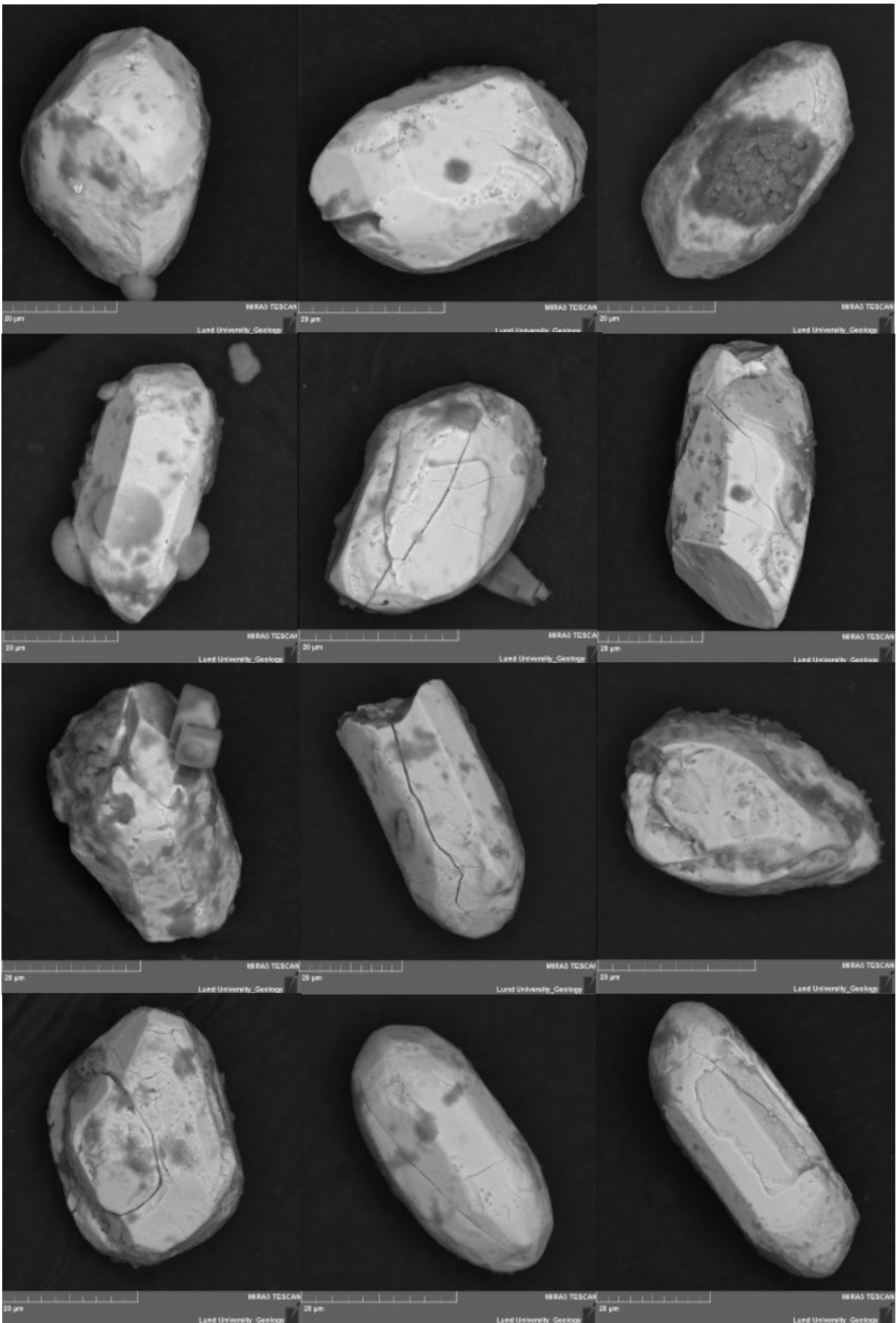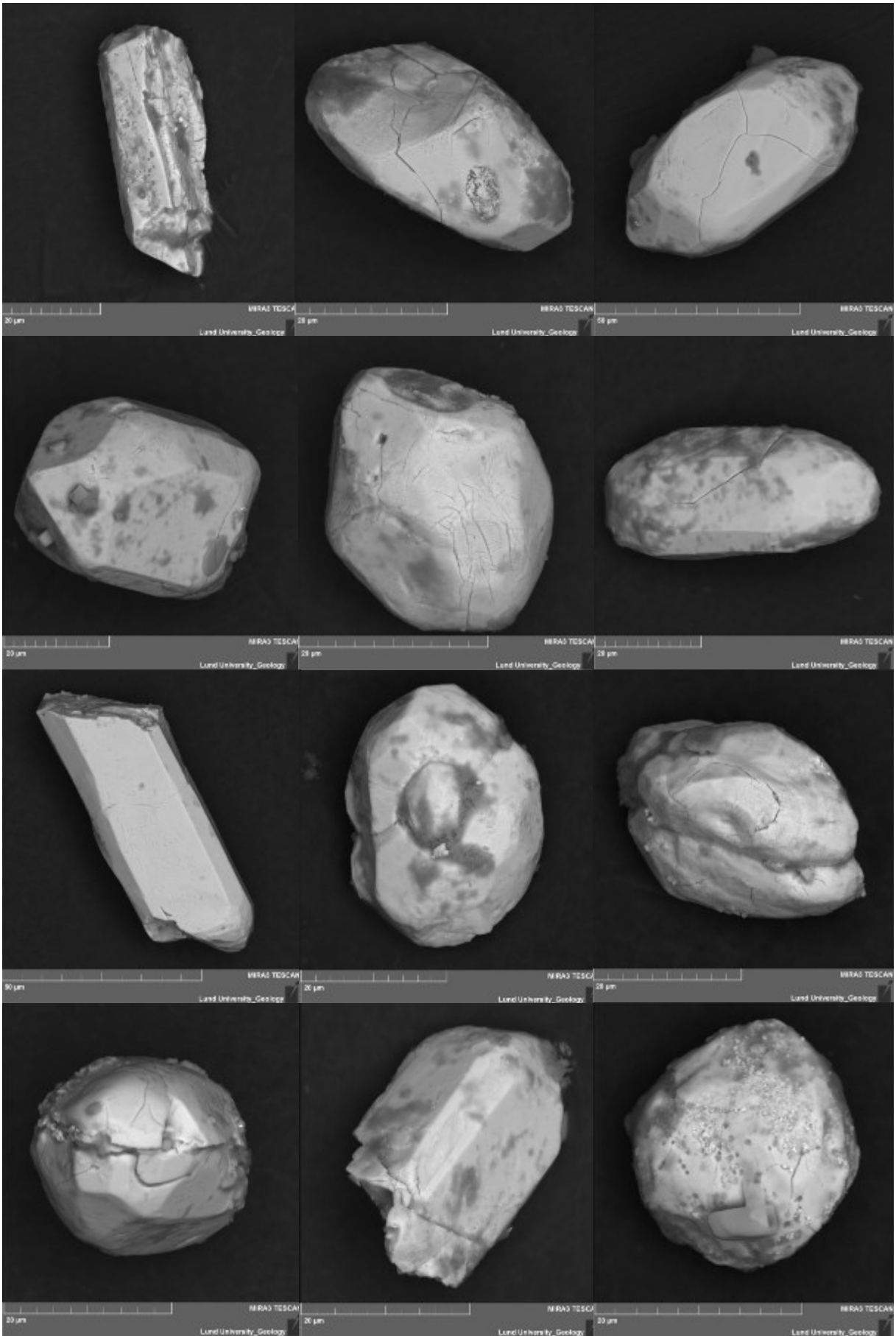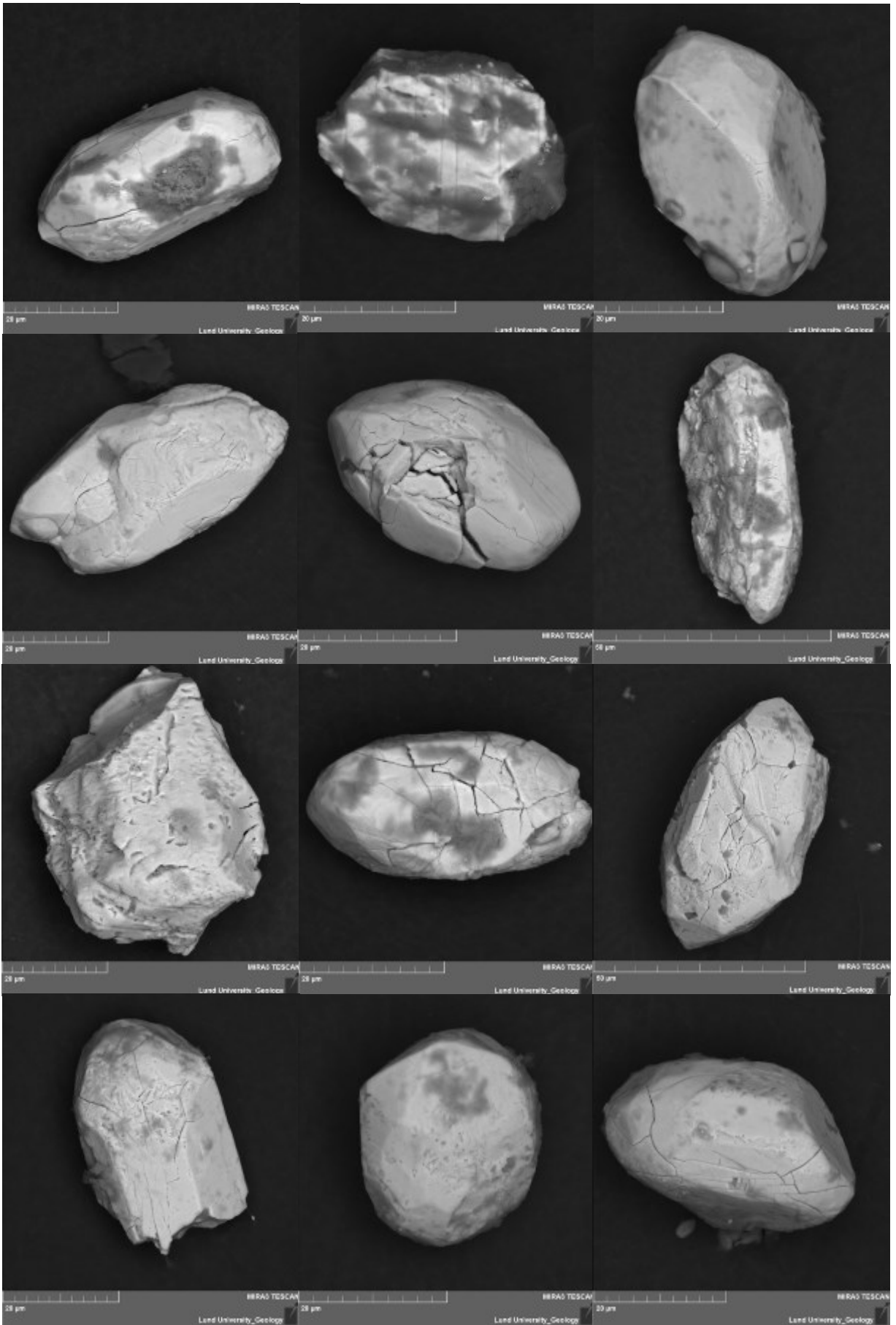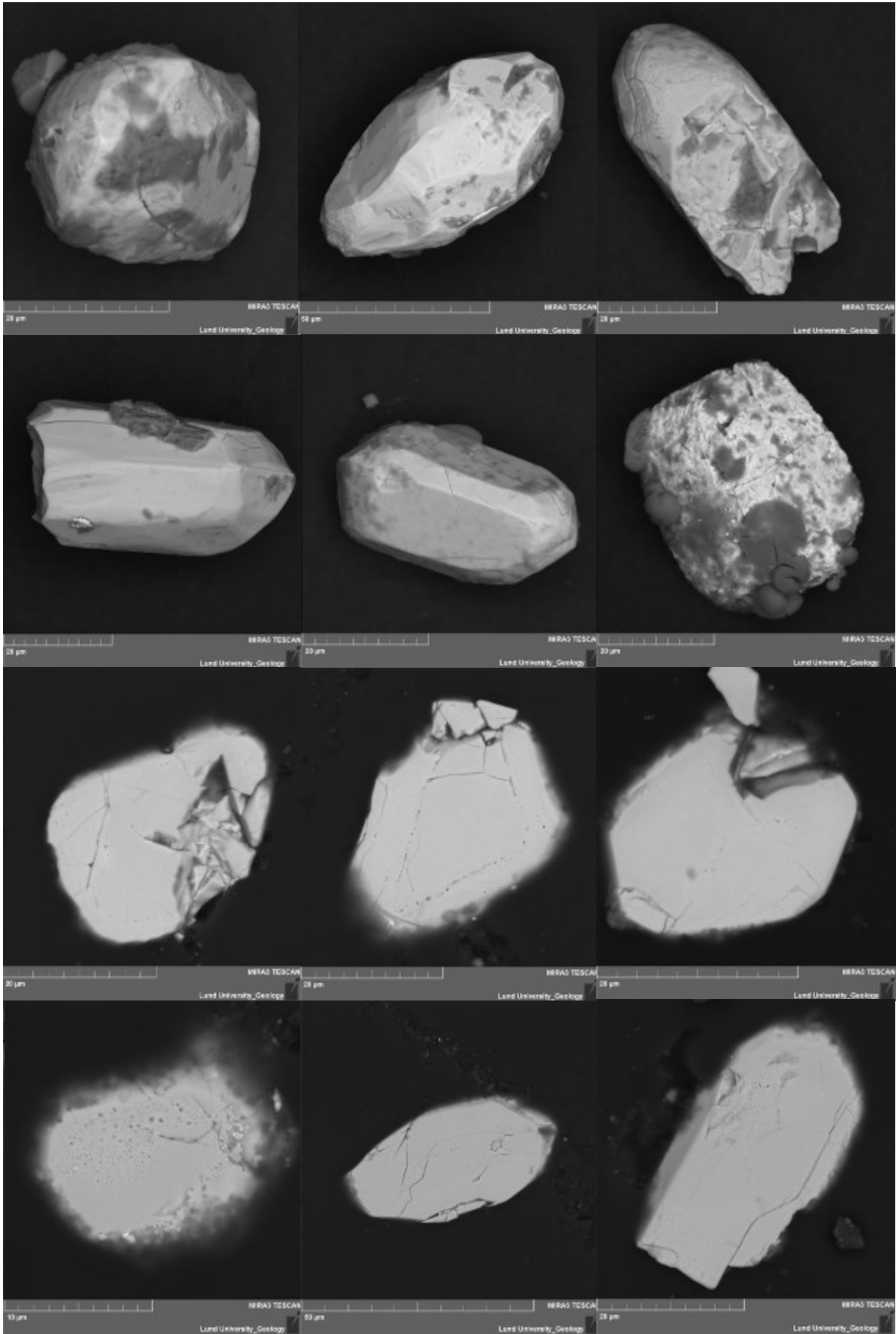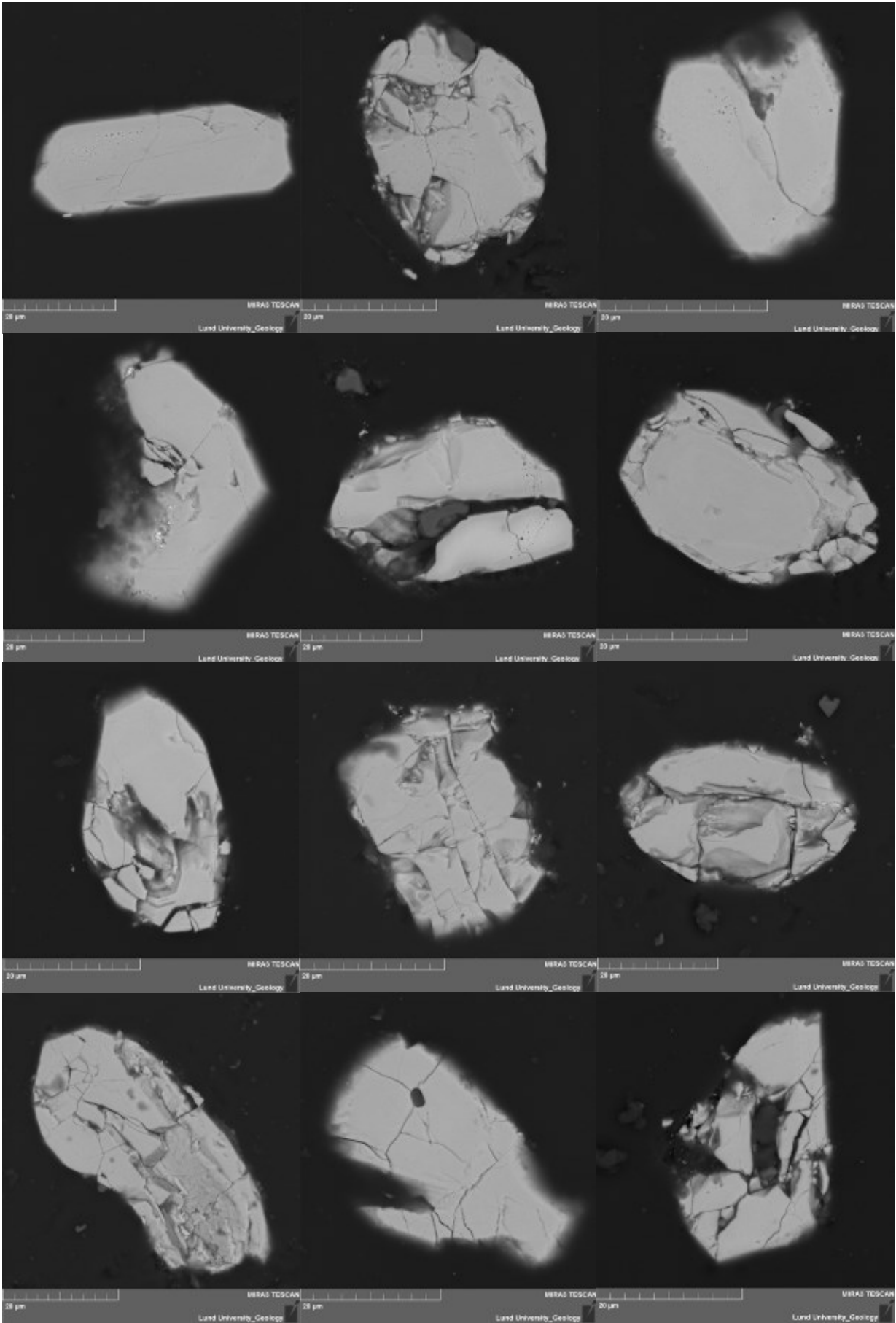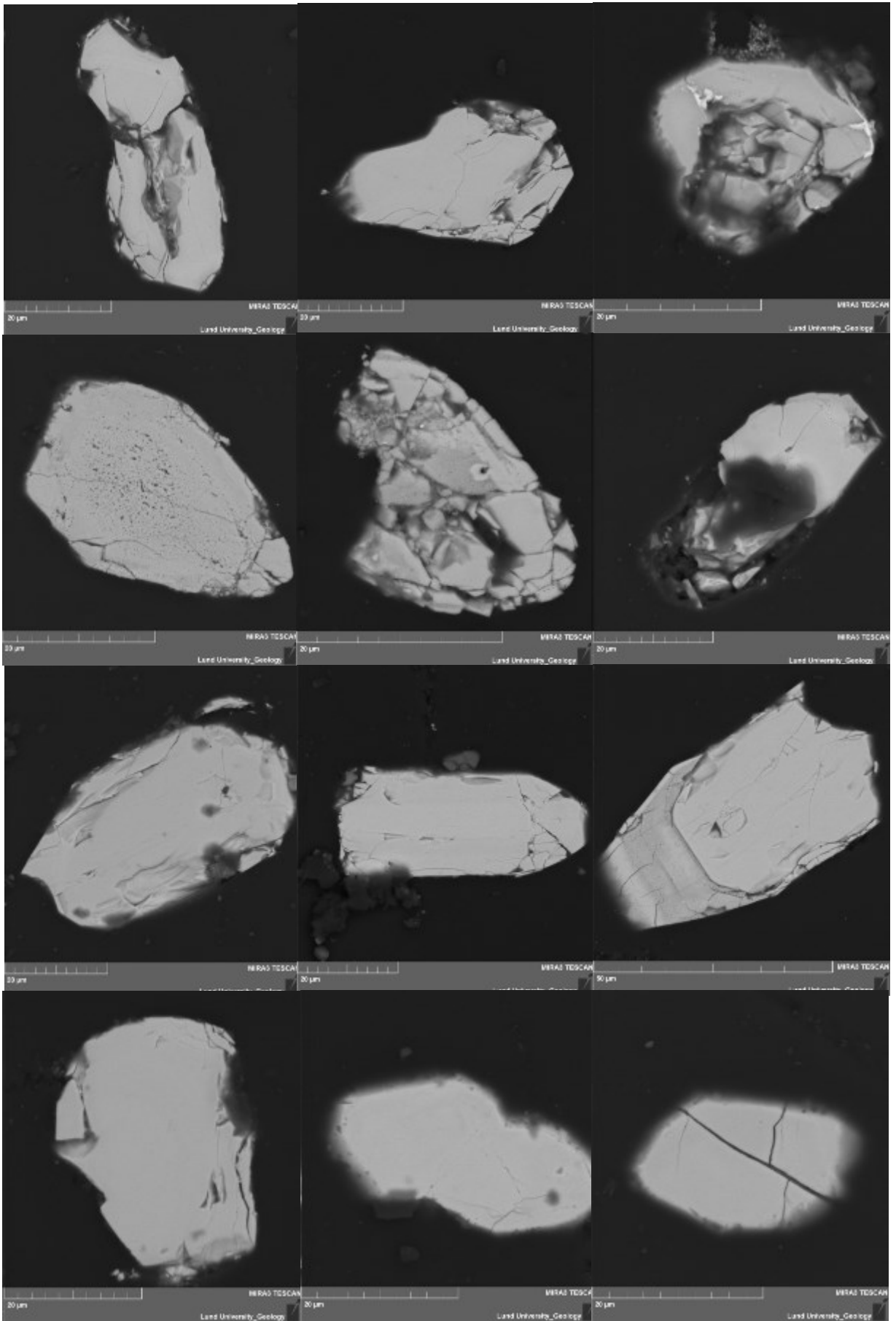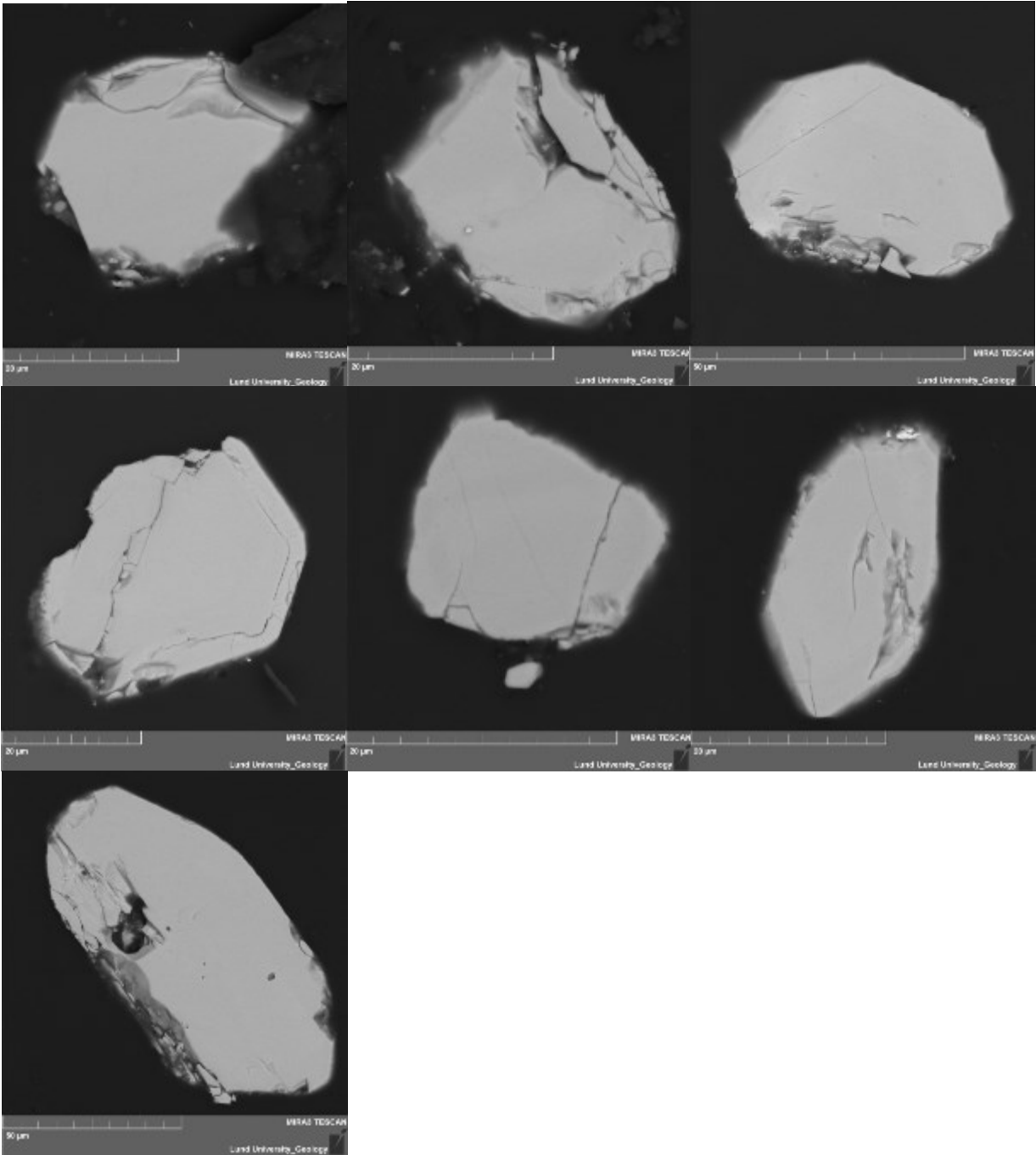
**Tidigare skrifter i serien
"Examensarbeten i Geologi vid Lunds
universitet":**

485. Plan, Anders, 2016: Markradar- och resistivitetsmätningar – undersökningar utav korrosionsförhöjande markegenskaper kring fjärrvärmeledningar i Ängelholm. (15 hp)
486. Jennerheim, Jessica, 2016: Evaluation of methods to characterise the geochemistry of limestone and its fracturing in connection to heating. (45 hp)
487. Olsson, Pontus, 2016: Ekologiskt vatten från Lilla Klåveröd: en riskinventering för skydd av grundvatten. (15 hp)
488. Henriksson, Oskar, 2016: The Dynamics of Beryllium 10 transport and deposition in lake sediments. (15 hp)
489. Brådenmark, Niklas, 2016: Lower to Middle Ordovician carbonate sedimentology and stratigraphy of the Pakri peninsula, north-western Estonia. (45 hp)
490. Karlsson, Michelle, 2016: Utvärdering av metoderna DCIP och CSIA för identifiering av nedbrytningszoner för klorerade lösningsmedel: En studie av Färgaren 3 i Kristianstad. (45 hp)
491. Elali, Mohammed, 2016: Flygsanddyners inre uppbyggnad – georadarundersökning. (15 hp)
492. Preis-Bergdahl, Daniel, 2016: Evaluation of DC Resistivity and Time-Domain IP Tomography for Bedrock Characterisation at Önneslöv, Southern Sweden. (45 hp)
493. Kristensson, Johan, 2016: Formation evaluation of the Jurassic Stø and Nordmela formations in exploration well 7220/8-1, Barents Sea, Norway. (45 hp)
494. Larsson, Måns, 2016: TEM investigation on Challapampa aquifer, Oruro Bolivia. (45 hp)
495. Nylén, Fredrik, 2017: Utvärdering av borrhålskartering avseende kalksten för industriella ändamål, File Hajdarbrottet, Slite, Gotland. (45 hp)
496. Mårdh, Joakim, 2017: A geophysical survey (TEM; ERT) of the Punata alluvial fan, Bolivia. (45 hp)
497. Skoglund, Wiktor, 2017: Provenansstudie av detriala zirkoner från ett guldförande alluvium vid Ravlunda skjutfält, Skåne. (15 hp)
498. Bergcrantz, Jacob, 2017: Ett fönster till Kattegatts förflutna genom analys av bottenlevande foraminiferer. (15 hp)
499. O'Hare, Paschal, 2017: Multiradionuclide evidence for an extreme solar proton event around 2610 BP. (45 hp)
500. Goodship, Alastair, 2017: Dynamics of a retreating ice sheet: A LiDAR study in Värmland, SW Sweden. (45 hp)
501. Lindvall, Alma, 2017: Hur snabbt påverkas och nollställs luminiscenssignaler under naturliga ljusförhållanden? (15 hp)
502. Sköld, Carl, 2017: Analys av stabila isotoper med beräkning av blandningsförhållande i ett grundvattenmagasin i Älvkarleby-Skutskär. (15 hp)
503. Sällström, Oskar, 2017: Tolkning av geofysiska mätningar i hammarborrhål på södra Gotland. (15 hp)
504. Ahrenstedt, Viktor, 2017: Depositional history of the Neoproterozoic Visingsö Group, south-central Sweden. (15 hp)
505. Schou, Dagmar Juul, 2017: Geometry and faulting history of the Long Spur fault zone, Castle Hill Basin, New Zealand. (15 hp)
506. Andersson, Setina, 2017: Skalbärande marina organismer och petrografi av tidigcampanska sediment i Kristianstadsbassängen – implikationer på paleomiljö. (15 hp)
507. Kempengren, Henrik, 2017: Föroreningsspridning från kustnära deponi: Applicering av Landsim 2.5 för modellering av lakvattentransport till Östersjön. (15 hp)
508. Ekborg, Charlotte, 2017: En studie på samband mellan jordmekaniska egenskaper och hydrodynamiska processer när erosion påverkar släntstabiliteten vid ökad nederbörd. (15 hp)
509. Silvén, Björn, 2017: LiDARstudie av glaciala landformer sydväst om Söderåsen, Skåne, Sverige. (15 hp)
510. Rönning, Lydia, 2017: Ceratopsida dinosauriers migrationsmönster under krittiden baserat på paleobiogeografi och fylogeni. (15 hp)
511. Engleson, Kristina, 2017: Miljökonsekvensbeskrivning Revinge brunnsfält. (15 hp)
512. Ingered, Mimmi, 2017: U-Pb datering av zirkon från migmatitisk gnejs i Delsjöområdet, Idefjordenterrängen. (15 hp)
513. Kervall, Hanna, 2017: EGS - framtidens geotermiska system. (15 hp)
514. Walheim, Karin, 2017: Kvartsmineralogins betydelse för en lyckad luminiscensdatering. (15 hp)
515. Aldenius, Erik, 2017: Lunds Geotermisystem, en utvärdering av 30 års drift. (15 hp)
516. Aulin, Linda, 2017: Constraining the duration of eruptions of the Rangitoto volcano, New Zealand, using paleomagnetism. (15 hp)
517. Hydén, Christina Engberg, 2017: Drumlinerna i Löberöd - Spår efter flera isrörelseriktningar i mellersta Skåne. (15

hp)

518. Svantesson, Fredrik, 2017: Metodik för kartläggning och klassificering av erosion och släntstabilitet i vattendrag. (45 hp)

519. Stjern, Rebecka, 2017: Hur påverkas luminiscenssignaler från kvarts under laboratorieförhållanden? (15 hp)

520. Karlstedt, Filippa, 2017: P-T estimation of the metamorphism of gabbro to garnet amphibolite at Herrestad, Eastern Segment of the Sveconorwegian orogen. (45 hp)

521. Önnervik, Oscar, 2017: Ooider som naturliga arkiv för förändringar i havens geokemi och jordens klimat. (15 hp)

522. Nilsson, Hanna, 2017: Kartläggning av sand och naturgrus med hjälp av resistivitetsmätning på Själland, Danmark. (15 hp)

523. Christensson, Lisa, 2017: Geofysisk undersökning av grundvattenskydd för planerad reservvattentäkt i Mjölkalånga, Hässleholms kommun. (15 hp)

524. Stamsnijder, Joaen, 2017: New geochronological constraints on the Klipriviersberg Group: defining a new Neoarchean large igneous province on the Kaapvaal Craton, South Africa. (45 hp)

525. Becker Jensen, Amanda, 2017: Den eocena Furformationen i Danmark: exceptionella bevaringstillstånd har bidragit till att djurs mjukdelar fossiliserats.(15 hp)

526. Radomski, Jan, 2018: Carbonate sedimentology and carbon isotope stratigraphy of the Tallbacken-1 core, early Wenlock Slite Group, Gotland, Sweden. (45 hp)

527. Pettersson, Johan, 2018: Ultrastructure and biomolecular composition of sea turtle epidermal remains from the Campanian (Upper Cretaceous) North Sulphur River of Texas. (45 hp)

528. Jansson, Robin, 2018: Multidisciplinary perspective on a natural attenuation zone in a PCE contaminated aquifer. (45 hp)

529. Larsson, Alfred, 2018: Rb-Sr sphalerite data and implications for the source and timing of Pb-Zn deposits at the Caledonian margin in Sweden. (45 hp)

530. Balija, Fisnik, 2018: Stratigraphy and pyrite geochemistry of the Lower–Upper Ordovician in the Lerhamn and Fågelsång -3 drill cores, Scania, Sweden. (45 hp)

531. Höglund, Nikolas, 2018: Groundwater chemistry evaluation and a GIS-based approach for determining groundwater potential in Mörbylånga, Sweden. (45 hp)

532. Haag, Vendela, 2018: Studie av mikrostrukturer i karbonatslagkäglor från nedslagsstrukturen Charlevoix, Kanada. (15 hp)

533. Hebrard, Benoit, 2018: Antropocen – vad, när och hur? (15 hp)

534. Jancsak, Nathalie, 2018: Åtgärder mot kusterosion i Skåne, samt en fallstudie av erosionsskydden i Löderup, Ystad kommun. (15 hp)

535. Zachén, Gabriel, 2018: Mesosideriter – redogörelse av bildningsprocesser samt SEM-analys av Vaca Muertameteoriten. (15 hp)

536. Fägersten, Andreas, 2018: Lateral variability in the quantification of calcareous nannofossils in the Upper Triassic, Austria. (15 hp)

537. Hjertman, Anna, 2018: Förutsättningar för djupinfiltration av ytvatten från Ivösjön till Kristianstadbassängen. (15 hp)

538. Lagerstam, Clarence, 2018: Varför svalde svanödlor (Reptilia, Plesiosauria) stenar? (15 hp)

539. Pilser, Hannes, 2018: Mg/Ca i bottenlevande foraminiferer, särskilt med avseende på temperaturer nära 0°C. (15 hp)

540. Christiansen, Emma, 2018: Mikroplast på och i havsbotten - Utbredningen av mikroplaster i marina bottensediment och dess påverkan på marina miljöer. (15 hp)

541. Staahlnacke, Simon, 2018: En sammanställning av norra Skånes prekambriska berggrund. (15 hp)

542. Martell, Josefin, 2018: Shock metamorphic features in zircon grains from the Mien impact structure - clues to conditions during impact. (45 hp)

LUNDS UNIVERSITET